ANALYSIS OF ELECTROMAGNETIC WAVE SCATTERED FROM CURVED SURFACE USING UNIFORM GEOMETRICAL THEORY OF DIFFRACTION

KITTISAK PHAEBUA

A THESIS SUBMITTED IN PARTIAL FULLFILLMENT
OF THE REQUIREMENT FOR THE DEGREE OF
DOCTOR OF ENGINEERING IN ELECTRICAL ENGINEERING
FACULTY OF ENGINEERING
KING MONGKUT'S INSTITUTE OF TECHNOLOGY LADKRABANG
2012

KMITL-2012- EN-D-018-148

หัวข้อวิทยานิพนธ์	การวิเคราะห์การกระจัดกระจายคลื่นแม่เหล็กไฟฟ้าจากโครงสร้างผิวโค้ง โดยทฤษฎีการเลี้ยวเบนเชิงเรขาคณิตแบบสม่ำเสมอ
นักศึกษา	นายกิตติศักดิ์ แพบัว
รหัสประจำตัว	51060027
ปริญญา	วิศวกรรมศาสตรดุษฎีบัณฑิต
สาขาวิชา	วิศวกรรมไฟฟ้า
พ.ศ.	2555
อาจารย์ที่ปรึกษาวิทยานิพนธ์	รศ. ดร. ชูวงค์ พงศ์เจริญพาณิชย์
อาจารย์ที่ปรึกษาวิทยานิพนธ์ร่วม	ผศ.ดร. ฐิติพงษ์ เลิศวิริยะประภา

บทคัดย่อ

ผลเฉลยของทฤษฎีการเลี้ยวเบนของคลื่นแม่เหล็กไฟฟ้าแบบสม่ำเสมอ (Uniform Geometrical Theory of Diffraction: UTD) ในวิทยานิพนธ์นี้ได้ถูกพัฒนาขึ้นจากฟังก์ชันของกรีน (Green's function) แบบสามมิติเพื่อคำนวณการกระจัดกระจายคลื่นแม่เหล็กไฟฟ้าจากพื้นผิวอิมพีแดนซ์โค้งแบบราบเรียบ ซึ่งแตกต่างจากผลเฉลย UTD สำหรับพื้นผิวโค้งตัวนำสมบูรณ์ (Perfectly electric conductor: PEC) ที่มีมาก่อนหน้านี้ โดยผลเฉลยของฟังก์ชันกรีนแบบสามมิติและผลเฉลย UTD ที่นำเสนอถูกสร้างจากเงื่อนไขขอบเขตของพื้นผิวอิมพีแดนซ์ของปัญหาอิมพีแดนซ์ทรงกระบอก ยิ่งไปกว่านั้นแล้วผลเฉลย UTD ที่ถูกปรับปรุงให้สามารถคำนวณการกระจัดกระจายของคลื่นแม่เหล็กไฟฟ้าจากพื้นผิวอิมพีแดนซ์ทรงกระบอกแบบสามมิติได้ถูกพัฒนาควบคู่กันกับผลเฉลยข้างต้นด้วย ซึ่งผลเฉลย UTD ที่ถูกปรับปรุงนี้อยู่บนพื้นฐานการปรับปรุงโดยการคาดการณ์อย่างมีหลักการ (heuristic modify) จากผลเฉลย UTD สำหรับพื้นผิวโค้งตัวนำสมบูรณ์ (PEC) ที่มีมาก่อนหน้านี้ในรูปแบบสามมิติ โดยฟังก์ชันอินทิเกรต Pekeris หรือถูกเรียกว่าฟังก์ชันอินทิเกรตของ Fock ในผลเฉลย UTD สำหรับพื้นผิวโค้ง PEC ที่มีมาก่อนหน้านี้ได้ถูกแทนที่ด้วยฟังก์ชันอินทิเกรตของ Fock สำหรับพื้นผิวอิมพีแดนซ์โค้งในรูปแบบสองมิติ จากการศึกษาพบว่าผลเฉลย

UTD ในรูปแบบสามมิติที่อยู่บนพื้นฐานของฟังก์ชันกรีนแบบสามมิติสามารถลดรูปสู่ผลเฉลย UTD ที่ถูกปรับปรุงได้อย่างถูกต้อง

ซึ่งมีความแตกต่างจากกรณีพื้นผิวโค้งตัวนำสมบูรณ์ (PEC) เมื่อฟังก์ชันอินทิเกรตของ Fock ในกรณีพื้นผิวโค้งตัวนำสมบูรณ์ (PEC) สามารถหาค่าโดยการประมาณ แต่ฟังก์ชันอินทิเกรตของ Fock แบบอิมพีแดนซ์นั้นไม่สามารถทำได้และจะต้องคำนวณด้วยวิธีการเชิงเลขเท่านั้น ผลการคำนวณการกระจัดกระจายคลื่นแม่เหล็กไฟฟ้าจากพื้นผิวอิมพีแดนซ์โค้งโดยการใช้ผลเฉลย UTD ที่ถูกปรับปรุงแสดงความสอดคล้องกันเป็นอย่างดีเมื่อเปรียบเทียบกับวิธีการเชิงเลขอื่นๆ

รวมทั้งในวิทยานิพนธ์นี้ ได้นำเสนอกระบวนการทางทฤษฎีในการทำนายการสูญเสียที่เปลี่ยนไปตามระยะทางของการแพร่กระจายคลื่นแม่เหล็กไฟฟ้าในสภาพแวดล้อมของสวนผลไม้ การทำนายการสูญเสียที่เปลี่ยนไปตามระยะทางในระบบโครงข่ายตรวจจับแบบไร้สายสำหรับระบบการเก็บเกี่ยวผลผลิตในสวนทุเรียนได้ถูกเลือกมาเป็นกรณีตัวอย่างในการศึกษาวิจัยนี้ ผลเฉลย UTD ที่นำเสนอถูกนำมาใช้ในการทำนายการสูญเสียที่เปลี่ยนไปตามระยะทางในการศึกษาวิจัยนี้ สภาพแวดล้อมของสวนผลไม้ถูกจำลองด้วยรูปทรงเรขาคณิตตามแบบที่ใช้ในทฤษฎีการเลี้ยวเบนของคลื่นแม่เหล็กไฟฟ้าแบบสม่ำเสมอ ตัวอย่างเช่น พื้นผิวไดอิเล็กตริกเรียบและโครงสร้างอิมพีแดนซ์ทรงกระบอกนั้นถูกจำลองแทนพื้นดินและต้นไม้ตามลำดับ และยิ่งไปกว่านั้นแล้วตัวตรวจจับแบบไร้สายได้ถูกติดตั้งบนผิวของผลทุเรียนที่อยู่บนต้นทุเรียน ผลทุเรียนจึงทำตัวเป็นส่วนหนึ่งของตัวตรวจจับแบบไร้สาย ดังนั้นเพื่อให้ได้มาซึ่งความถูกต้องมากยิ่งขึ้นในการจำลองแบบรูปการแพร่กระจายคลื่นของแหล่งกำเนิดคลื่น การกระจายตัวของลำคลื่นเกาส์เซียน (Gaussian beam expansion) โดยใช้เทคนิคตำแหน่งของแหล่งกำเนิดคลื่นเป็นจำนวนเชิงซ้อนได้ถูกนำมาใช้ในการจำลองแหล่งกำเนิดคลื่นด้วย ผลการทำนายการสูญเสียที่เปลี่ยนไปตามระยะทางจากกระบวนการเชิงเลขที่ได้นำเสนอและผลการทดสอบมีความสอดคล้องกันเป็นอย่างดี กระบวนการเชิงเลขที่ได้นำเสนอเพื่อคำนวนการสูญเสียที่เปลี่ยนไปตามระยะทางจากสภาพแวดล้อมจริงของสวนผลไม้จะเป็นประโยชน์สำหรับการวางแผนการติดตั้งโครงข่ายการสื่อสาร ตัวอย่างเช่นในระบบโครงข่ายตรวจจับแบบไร้สายสำหรับการเก็บเกี่ยวผลผลิตและในสภาพแวดล้อมอื่นๆอีกด้วย

Thesis Title	Analysis of Electromagnetic Wave Scattered from Curved Surface Using Uniform Geometrical Theory of Diffraction
Student	Mr. Kittisak Phaebua
Student ID.	51060027
Degree	Doctor of Engineering
Program	Electrical Engineering
Year	2012
Thesis Advisor	Assoc. Prof. Dr. Chuwong Phongcharoenpanich
Thesis Co-advisor	Asst. Prof. Dr. Titipong Lertwiriyaprapa

ABSTRACT

The three dimensional (3-D) uniform geometrical theory of diffraction (UTD) solution in this dissertation is developed from the exact 3-D Green's functions to predict the electromagnetic wave (EM) scattered from a 3-D smooth curved impedance surface. Unlike the original UTD solution for a perfectly electric conductor (PEC) curved surface, the proposed exact solution of the 3-D Green's functions and the proposed 3-D UTD solution are constructed from the impedance surface boundary condition (IBC) of the impedance cylinder problem. Moreover, the modified 3-D UTD solution is also developed to predict the EM wave scattered from the impedance cylinder. The proposed modified 3-D UTD solution is based on heuristically modifying the original 3-D UTD solution for the corresponding smooth convex PEC scattering problem. The Pekeris-integral function or called Fock-type integral function in the 3-D UTD PEC solution is replaced by the two dimensional (2-D) impedance Fock-type integral function. Surprisingly, it is found that the 3-D UTD solution based on the exact closed form solution of the 3-D Green's functions can be reduced into the modified 3-D UTD solution.

In contrast to the PEC case in which the PEC Fock-type integral function can be approximated using large/small argument approximation and tabulation technique, the Fock-type integral function for the impedance case must be numerically computed. The results from the modified 3-D UTD solution show good agreement with the independent solution from commercial software.

The application of the proposed 3-D UTD solution is also demonstrated. In this dissertation, the proposed theoretical path-loss prediction procedure and the measured results of the EM wave propagation in an orchard environment are presented. The path-loss prediction of the pre-harvesting WSN system in a durian (*Durio zibethinus Murray*) orchard is chosen to be an example of this study. The proposed 3-D UTD scattering solution for a curved impedance surface is employed for theoretical path-loss prediction. The orchard scenario is modeled using a canonical geometries of the UTD method, such as a dielectric flat surface and a cylindrical structures with an impedance surface to respectively represent the ground and trees. Moreover, since the wireless sensor node is attached to the outside peel of a hanging durian fruit, the fruit partially acts as a wireless sensor node (i.e. source). Therefore, to obtain greater accuracy in the source radiation pattern, the Gaussian beam (GB) expansion via the complex source point (CSP) technique is used for source modeling. The path loss prediction from the proposed numerical procedure and the measured results are in good agreement. The proposed numerical procedure to predict the path loss from actual scenario of the orchard is also useful for network planning, such as the pre-harvesting WSN system and other orchard scenarios.

ACKNOWLEDGEMENTS

I would like to express my special appreciation to my advisor, Assoc. Prof. Dr. Chuwong Phongcharoenpanich, for his guidance and support throughout my Ph.D. study. I also would like to extend my sincerest thanks to my co-advisor, Asst. Prof. Dr. Titipong Lertwiriyaprapa, for his important discussions, ideas, and feedbacks in my research work. I also would like to express my appreciation to Prof. Dr. Monai Krairiksh, for his valuable discussions and for the experimental equipments. I also would like to express my deepest gratitude to Prof. Dr. Prabhakhar H. Pathak, for his important guidance in the theoretical parts and support throughout my research at ElectroScience Laboratory (ESL), Ohio State University, Columbus USA, during February 2010 to August 2011 of my visiting scholar program.

Especially, my Ph.D. program was supported by the Thailand Research Fund (TRF) through the Royal Golden Jubilee, Ph.D. Program under Grant No. PHD/0177/2550.

Finally, I would especially like to thank my family for the love, encouragement and support.

Kittisak Phaebua

VITA

Kittisak Phaebua received the B. Eng. and M. Eng. degrees in Telecommunications Engineering from the Department of Telecommunications Engineering, Faculty of Engineering, King Mongkut's Institute of Technology Ladkrabang (KMITL), Bangkok, Thailand, in 2006 and 2008, respectively. He has studied for Ph.D. in Electrical Engineering at KMITL. He received a Ph.D. scholarship from the Thailand Research Fund (TRF) through the Royal Golden Jubilee Ph.D. Program. He was a visiting scholar student in ElectroScience Laboratory, Ohio State University, Columbus USA, during February 2010 to August 2011. His research interests include the electromagnetic wave radiation, coupling and scattering by an impedance curved surface based on the Uniform Geometrical Theory of Diffraction (UTD) method and also antenna/passive microwave components design for a mobile phone, RFID and wireless LAN systems.

PUBLICATIONS

[1] K. Phaebua, T. Lertwiriyaprapa, C. Phongcharoenpanich and M. Krairiksh, "Path-Loss Prediction of Radio Wave Propagation in an Orchard by using Modified UTD Method," *Progress in Electromagnetics Research (PIER) Journal*, vol. 128, pp. 347-363, 2012.

[2] K. Phaebua, T. Lertwiriyaprapa, C. Phongcharoenpanich and M.Krairiksh, "2.45 GHz Path-Loss Prediction for Wireless Sensor Applications in an Orchard by using UTD method," *Proceedings of the 2011 International Symposium on Antennas and Propagation (ISAP2011)*, Jeju, Korea, pp.[ThF2-1]C07_1009, Oct.2011.

[3] P. H. Pathak, K. Phaebua, "A uniform geometrical theory of diffraction for radiation by antennas on a smooth convex impedance surface," *Proceedings of the 2011 International Conference on Electromagnetics in Advanced Applications (ICEAA2011),* Torino, Italy, pp. 405-408, 12-16 Sept. 2011.

[4] K. Phaebua, T. Lertwiriyaprapa, C. Phongcharoenpanich and P.H. Pathak, "A Modified UTD Solution for an Impedance Cylinder Surface," *Proceedings of the 2011 Electrical Engineering/Electronics, Computer, Telecommunications, and Information Technology International Conference (ECTI-CON2011)*, Khonkaen, Thailand, pp.208-211, May 2011.

[5] T. Lertwiriyaprapa, K. Phaebua, C. Phongcharoenpanich and M. Krairiksh, "Analysis of Electromagnetic Wave Scattering from a Curved Surface by Using the Uniform Geometrical Theory of Diffraction," *The Journal of King Mongkut's University of Technology North Bangkok*, vol.20, no.1, pp.161-167, 2010.

[6] K. Phaebua, T.Lertwiriyaprapa, C.Phongcharoenpanich and M.Krairiksh, "Analysis of an Electromagnetic Gaussian Beam Diffraction by a Thin Planar Material Half Plane," *Proceedings of the 2009 International Symposium on Antennas and Propagation (ISAP2009* Bangkok*)*, pp.1207-1210, October 2009.

[7] K. Phaebua, T. Lertwiriyaprapa, C. Phongcharoenpanich and M. Krairiksh, "Path Loss prediction in Durian Orchard Using Uniform Geometrical Theory of Diffraction," *Proceedings of the 2009 IEEE International Symposium on Antennas and Propagation and USNC/URSI National Radio Science Meeting (APS2009),* Charleston, South Carolina, USA, pp.230.5-1 - 230.5-4, June 2009.

TABLE OF CONTENTS

LIST OF FIGURES

Figure Page

LIST OF FIGURES (CONTINUE)

Figure Page

LIST OF FIGURES (CONTINUE)

Figure Page

LIST OF FIGURES (CONTINUE)

Figure Page

LIST OF FIGURES (CONTINUE)

Figure Page

LIST OF TABLES

Table Page

CHAPTER 1
INTRODUCTION

1.1 Motivation and Objective

Wireless Sensor Network (WSN) basically consists of the distributed sensor nodes and the communication nodes which aims to detect some important data [1] such as temperature, humidity, pressure and pollutant conditions in an environmental detection systems. Moreover, sound, vibration and motion detection of the security system and also in military applications, the WSN is increasingly employed. The WSN topologies are shown in Fig. 1.1. The sensor nodes in the sensing areas transfer the detected data to the monitor station via the sensor nodes itself and/or the communication/routing nodes. Recently, the WSN is increasingly used in forest environment applications. For example, the real-time forest fire detection, the humidity detection and the water level detection systems are presented in [2] and [3]. The pre-harvesting systems in the orchard is presented in [4]. The drawing of the interested orchard problems are shown in Figure 1.2. The WSN for the wind turbine farm [5] and in the oil tanks farm are shown in Fig. 1.3(a) and (b) respectively, is applied in the security system to monitor status of the turbines and the oil tanks. The communication routes of the WSN are depended on the communication protocol. In the network planning procedure, the proper locations of both sensor and communication nodes are depended upon the signal strength at each setup location. In practice, the network planning step requires a knowledge of the channel characteristic, namely, the field strength everywhere in the communication area. Generally, the field strength in the sensing area or called the path-loss can be predicted using:

- Empirical models for predicting the path-loss are constructed from measurement path-loss data in real environments [6]-[10],
- Numerical methods such as finite difference time domain (FDTD) , finite integral technique (FIT) [11], Method of Moments (MoM), and other,

- High frequency methods such as the Uniform Geometrical Theory of Diffraction (UTD), Physical Optic (PO) and other. Actually, those solutions are based on ray approximation [6],[7], [12]-[35] .

The UTD method (i.e. High frequency method) is suitable for path-loss prediction of large communication area than other numerical methods. The prediction of the EM wave radiation and scattering via the UTD method becomes very useful and important in solving problems related to network planning of modern radio wave communication systems. Conventional numerical methods become highly inefficient or cannot treat the propagation problems because the computation domain is very large. Therefore, the numerical methods unsuited for dealing with such large problems. Besides, they provide no physical insight into the wave scattering and propagation mechanisms. The advantage and the disadvantage of those path-loss prediction methods will be discussed in the literature review of the Chapter 2.

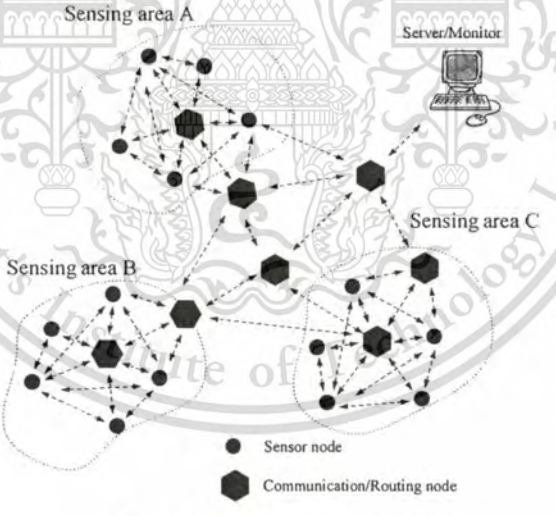

Figure 1.1 The WSN topologies.

For the situation in Figs. 1.2 and 1.3, the actual environment can be modeled using the canonical shapes of the UTD method such as the impedance cylinders and the dielectric flat surface to represent the trees/turbine towers/oil tanks and ground as shown in Fig. 1.3 (c), respectively. The wave propagation mechanisms in the sensing area, and

the total electromagnetic (EM) fields at the observation points consist of the incident wave (directed wave by source or line-of-sight field component), the reflected wave from ground, the reflected wave and the scattered wave from trees/turbine tower/oil tanks. In this case, the EM wave scattered by a group of leaves in the orchard of the problem in Fig. 1.2 and a turbine blades of the problem in Fig. 1.3(a) can be neglected because the heights of both sensor and communication nodes are very small (near ground). The main EM wave contributions from the tree trunks and ground surface are dominant [8]. The high frequency solutions of the incident wave from source and the reflected wave from ground are available at the present time. However, the 3-D solution to predict the reflection and scattering of EM wave from impedance cylinder is not available.

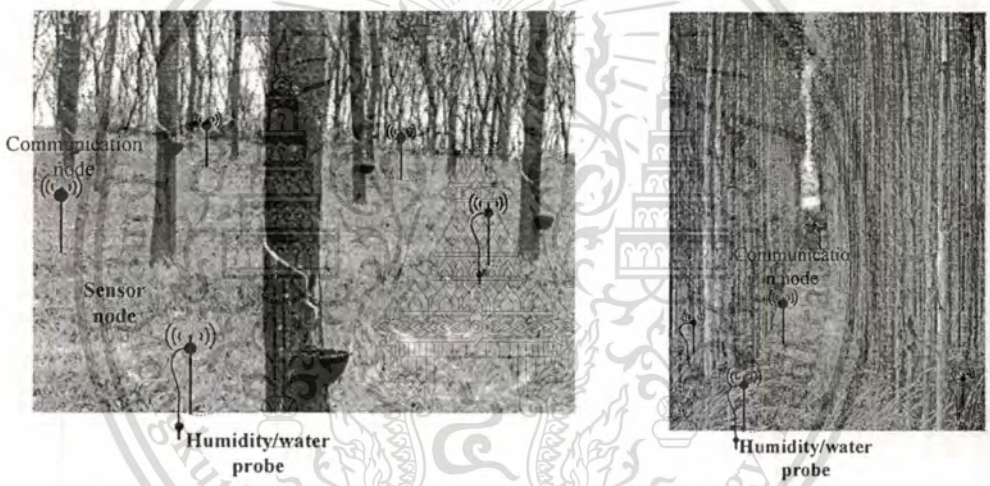

(a) Para rubber orchard (b) Eucalyptus logging

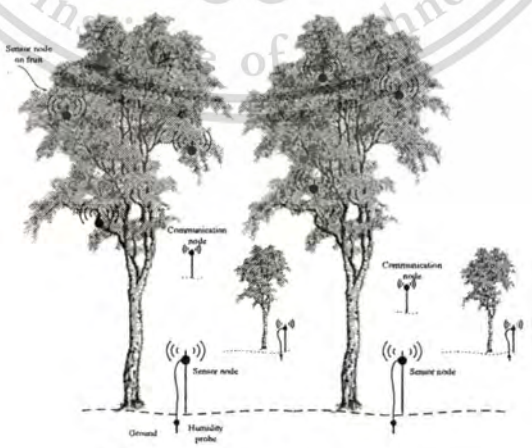

(c) Drawing of the orchard

Figure 1.2 Interested orchard problems.

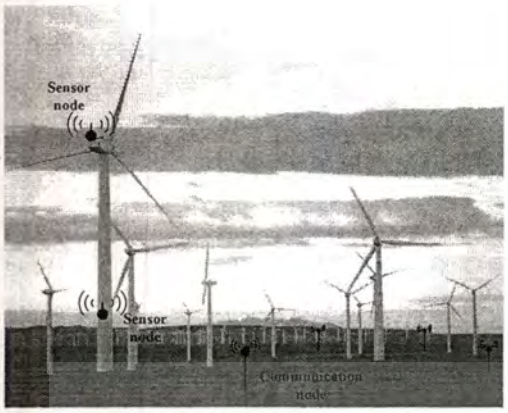

(a) Wind turbine farm

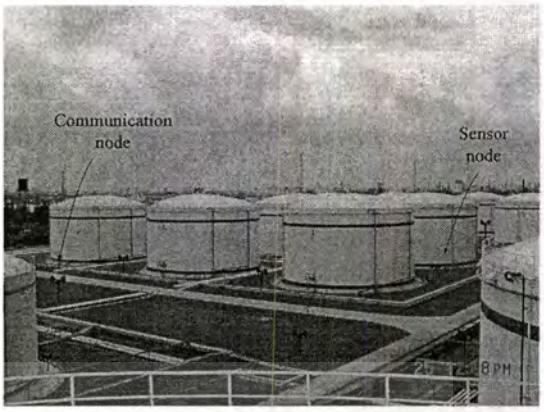

(b) Oil tanks farm

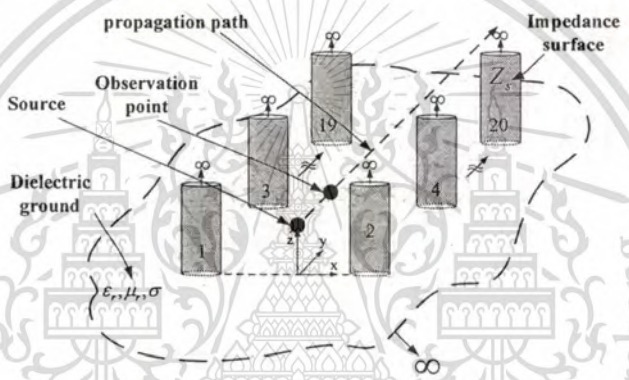

(c) Equivalent model

Figure 1.3 Interest problems and its equivalent model.

The objectives of this dissertation are to develop the closed form exact solution and the UTD solution for predicting the EM wave scattered from an impedance curved surface as shown in Fig. 1.4. The prediction of the incident wave, the reflected and the scattered wave from impedance curved surface in 3-D will be focused in this development. Importantly, the equivalent model using the impedance curved surface is used in the UTD method, which represents a non perfectly electric conductor (non-PEC) curved surface in an actual situation such as a tree surface, cylindrical shape of wind turbine tower, oil tanks, curved roof top, curved surface of air plane, missile surface and others. The details of the developed solutions in this dissertation are as follows.

- Develop the exact solution to predict EM wave scattered from impedance cylinder for both electric J_z and magnetic M_z current excitations.
- Develop the asymptotic solution to predict EM wave scattered from impedance cylinder.
- Develop the UTD solution for EM wave scattered from impedance cylinder.
- Construct the path-loss prediction procedure using the proposed UTD solution for WSN in orchard and other environments.

Figure 1.4 Impedance cylinder scattering problem.

1.2 Outline of the Dissertation

Objective, motivation of this dissertation and short details of the path-loss propagation prediction methods are described in this chapter. A short details of the remaining chapters are as follows:

Chapter 2 presents the literature reviews of the propagation path-loss prediction methods and the history of the UTD development for EM wave scattered from an impedance cylinder.

Chapter 3 presents an analysis of three dimensional (3-D) EM wave scattered from an impedance cylinder. The subsections consist of the derivation details of the exact solution based on 3-D Green's functions, the asymptotic and the UTD solution of EM wave scattered from an impedance cylinder. The development of the z-polarized electric current source J_z and the magnetic current source M_z excitations (i.e. along axis of the cylinder) are focused.

Chapter 4 presents the heuristic development of the modified 3-D uniform geometrical theory of diffraction (UTD) scattering solution for an impedance cylinder. The concept of heuristically modified 3-D UTD solution will be described. In the detail of this chapter, the classical 3-D UTD solution for EM wave scattered from perfectly electric conductor (PEC) cylinder will be summarized. The modified 3-D UTD solution, the accuracy and limitation of the modified 3-D UTD solution will be illustrated.

Chapter 5 presents the application of the proposed 3-D UTD solution. The path-loss of wave propagation prediction in an orchard of the WSN system using the proposed 3-D UTD solution is also demonstrated. The path-loss prediction procedure is constructed by using the proposed 3-D UTD solution. Source (i.e. antenna is attached on durian fruit), ground and tree bark modeling will be deeply described. In the last subsection, the advantages and the limitation of the path-loss prediction procedure will be concluded.

Chapter 6 the conclusion of this dissertation and the remark for future work will be discussed.

It should be noted that in this work all fields are assumed with $e^{j\omega t}$ time dependence and suppressed throughout.

CHAPTER 2

PATH-LOSS PREDICTION AND ELECTROMAGNETIC (EM) WAVE SCATTERED FROM AN IMPEDANCE CYLINDER

2.1 Introduction

In chapter 1, the objectives and the motivation of this dissertation are mentioned. In this chapter, the literature reviews of the path-loss predictions including the advantage and the disadvantage of those methods will be summarized. Especially, the theoretical development of the classical UTD solutions for EM wave scattered from a perfectly electric conductor (PEC) and an impedance cylinder of the previous works will be summarized in this chapter.

2.2 Brief of the Path-loss Prediction Methods

The demand for wireless communication systems, such as the mobile phone systems and Wireless Sensor Network (WSN), have been continuously increasing due to their wireless connection advantages [1]-[5]. For the network planning, every WSN/mobile phone applications require its specific propagation channel characteristic. Methods are used to predict the path-loss are as follows:

2.2.1 Empirical Models

Empirical models for predicting the path-loss are constructed by using a measurement path-loss data in an actual environment (i.e. data collection). For instance, the classical Okumura-Hata and COST 231 models are used for a mobile phone application in a large communication area with very high transmitting antennas and tall obstacles in the line-of-sight path and other [6]-[7]. In the forest environment such as COST 235, Weissberger models are used [8]-[10]. In table 1, the several empirical models are summarized.

Table 1. Summary of the several empirical models [6]-[10]

Models	Constrains	Scenarios
Okumura-Hata model for Urban Areas	• Frequency :150 to 1920 MHz • Mobile antenna height: 1 to 10 meters • Base station antenna height: 30 to 1000 meters • Not many tall blocking structures • Link distance: 1 km to 100 km	• In city with not many tall blocking structures • was constructed from the data of Tokyo Japan.
COST 231-Hata-Model	• Frequency: 1.5 to 2.0 GHz • Mobile Antenna Height: 1 up to 10m • Base station Antenna Height: 30m to 200m • Link Distance: 1 to 20 km	• In city
Two-ray	• Frequency: no specific • Without blocking structures	• Ground reflection such as concrete, grass or general grounds
COST 235	• Frequency: 9.6 to 57.6 GHz • Link Distance: < 200 meters	• Forest
Weissberger	• Frequency: 0.230 to 95 GHz • Depth of Foliage: up to 400 meters	• Foliage, vegetation or forest
ITU-R (ITU Vegetation Model)	• Frequency: 0.3 to 3.0 GHz • Link Distance: <400 meters	• Foliage, vegetation or forest
Chen and Kuo	• Frequency: 1 to 100 GHz • Link Distance: 10 to 100 meters	• Forest environment

However, most of the empirical models are dependent upon scenarios. For instance, the two-ray model is valid for use in the case of strong reflection from the ground, and the Weissberger model can be used in the forest setting to predict the path loss of wave propagation. Besides, Chen and Kua propose a model using vertical/horizontal polarizations for a forest. In such WSN applications, the transmitted power of WSN systems is very low, thus the coverage area being relatively small. The

transmitting antennas are located a few meters above the ground and the geometries of the environment such as buildings and ground have strong effects on the receiving power at the receiving points. As such, the wave propagation prediction requires a more accurate method to predict the signal strength in its respective scenario.

An efficient method for the wave propagation prediction is the high frequency method such the uniform geometrical theory of diffraction (UTD) [6],[7], [12]-[35] (i.e., analytical solution) while numerical methods are less efficient or unsuited to the propagation problems because the computation domain of the latter is very large in comparison with the electrical wavelength. In addition, the UTD method provides the physical insight that allows one to quantitatively and separately study the effects of field types at the observation point, while numerical methods require more efforts to extract the propagation mechanisms such as that presented in [11]. Unlike the empirical model, the analytical solution does not require any measured path-loss data to construct the path-loss model of each scenario. Only the actual geometries such as the positions, the diameters of a trees/oil tanks/wind turbine, and properties of the ground are required in the analytical procedure.

2.2.2 Numerical Methods

Generally, the numerical methods are unsuited to solve the large scattering problems, for instance, the Finite Difference Time Domain (FDTD), Finite Integral Technique (FIT) [11], Method of Moments (MoM), and others. The main issue is a computer resource and a computational time. The numerical methods require dramatically large memory (RAM) and high performance CPU such as a server computer machine. It is difficult to solve by using the general personal computer (PC). Moreover, the numerical methods do not provide the physical insight into the results. The effect of each field components cannot be studied separately.

2.2.3 High Frequency Techniques

The high frequency technique (i.e. deterministic or analytical models) such as the uniform geometrical theory of diffraction (UTD) is useful in the EM field prediction of the propagation problems [12]-[35]. Those solutions are based on the ray approximation

technique. The UTD method can analyze the EM fields everywhere in the considered area. The actual environment can be modeled using the canonical shapes, and then the path-loss can be predicted using the UTD solution. Unlike the summation of the eigen functions of the classical exact closed-form solutions [32]-[35], the UTD provides high accuracy at moderate to high frequency when the summation of the eigen functions is unsuited (very poorly convergent) as explained in [19]. The UTD solutions for the EM wave scattered from wedge, corner and vertex are usually employed to calculate the field strength in the radio wave propagation prediction of the mobile phone/wireless LAN systems [6], [7], [12]-[14]. The buildings are mapped into the UTD models, and the ray tracing is essentially used to find the ray paths. Moreover, the curved surface problems require the specific UTD solutions. The 2-D UTD solution for PEC curved surface was presented in [17] and 3-D case was presented in [18]. The UTD solution for EM wave scattered from curved surface is widely used in many propagation problems such as the UTD solution for multiple rounded surfaces to model the roof top of the building by the curved PEC surface that is proposed in [14]. In addition, a conducting cylinder for modeling human body presence in indoor propagation channel is presented in [15]. The path loss prediction in Durian orchard by using the UTD is presented in [16] under the assumption that the Durian trees are the PEC cylinders. However, the PEC surface model is efficiently used for only the case of strong reflection and diffraction from the obstacle such as building, wall and ground which are usually made from concrete or metal. Therefore, to model a trees, short-grass ground, and soil ground in the orchard scenario, the radio wave propagation prediction models require the UTD solutions with an impedance surface instead of the PEC surface.

2.3 Historical Development of the UTD Solution for EM Wave Scattered from an Impedance Cylinder

The classical 2-D UTD scattering solution for a PEC curved surface was presented in [17]. The 2-D UTD scattering solution for the impedance curved surface was presented in [25]-[27] using the same manner of the classical 2-D UTD solution [17]. However, the 2-D UTD solution for the impedance curved surface does not support in 3-D scenario. The 3-D UTD solution for the PEC curved surface was presented in [18]. The

solution was constructed from the 2-D solution [17] with different spreading factors, incident ray, reflected ray and diffracted ray terms. The solution contains:

- Lit zone (Line-of-sight)
    - Incident field at observation point.
    - Reflected field.
    - Diffracted fields from two sides of the cylinder.

The reflected field contains the incident field at the surface multiplied by reflection coefficient and reflected ray term. The diffracted field contains the incident field at the diffraction point multiply by the transmission coefficient and diffracted ray term.

- Shadow zone
    - The diffracted field contains the incident field at the diffraction point multiplied by the transmission coefficient and diffracted ray term.

The classical 2-D UTD scattering solution for a PEC curved surface [17] and the classical 2-D UTD scattering solution for the impedance curved surface [25]-[27], the solutions are constructed from the summation of Bessel and Hankel functions of the classical eigen solution with plane wave excitation. The Watson transformation [17] is employed to change the summation to the integrals, and then the steepest decent path (SDP) method is employed to asymptotically evaluate the integrals. Finally, the 2-D Fock-type integral functions are remained in the diffraction coefficient. For the PEC case, the remaining term of PEC Fock-type integral function can be computed by using the large/small approximation and interpolation in some regions. Conversely, the 2-D impedance Fock-type integral function requires the numerical integration. A numerical scheme to compute the 2-D impedance Fock-type integral function was proposed in [36] by deforming the new contour of the integral together with the Fourier quadrature numerical integration.

2.4 Summary

According to the previous section, the disadvantages of the empirical models for predicting the path loss of the WSN system are mentioned. Moreover, the classical 3-D UTD PEC and 2-D impedance surface solutions do not support the 3-D impedance

curved surface. Thus, in this dissertation, the 3-D UTD solution for EM wave scattered from impedance curved surface are developed. The alternative Green' function representation is employed to develop the 3-D UTD solution. The alternative Green' function representation can be found in Appendix A. The alternative Green's function representation was presented in [21]. The deep details of the alternative Green's function representation can be found in [22]. The exact solution of wave equation can be written as the double integrals of the characteristic Green's function of each direction. Unlike the classical UTD development, the proposed UTD development does not require the Watson's transform. Also, the magnetic and electric point current sources are employed instead of the plane wave illumination. The theoretical development and procedures in this dissertation are as follows:

- Develop the exact solutions to predict EM wave scattered from an impedance cylinder for both electric J_z and magnetic M_z point current sources. The alternative Green's function representation together with the impedance boundary condition (IBC) are used to construct the exact solutions.
- Develop the asymptotic solutions to predict EM wave scattered from an impedance cylinder using the asymptotic approximation. The steepest decent path (SDP) method together with the large argument approximation of the Bessel and Hankel functions are employed.
- The transformation between the cylindrical and ray coordinate system is employed to construct the 3-D UTD solution for EM wave scattered from an impedance cylinder.

Finally, the path-loss prediction procedure for WSN (for short range communication and low transmitting and receiving antenna heights) in orchard and other forest environments using the proposed 3-D UTD solution will be constructed.

CHAPTER 3
AN ANALYSIS OF THREE DIMENSIONAL (3-D) ELECTROMAGNETIC (EM) WAVE SCATTERED FROM AN IMPEDANCE CYLINDER

3.1 Introduction

In this chapter, the derivations of the three dimensional (3-D) exact, asymptotic and UTD solutions for the EM wave scattered from an impedance cylinder are deeply explained. In Section 3.2, the exact solutions of the wave equations are constructed using the Green's function technique. Using the impedance boundary condition (IBC) at the surface of the scatterer, the closed form exact 3-D solution is simply achieved. However, the closed-form exact solution cannot be computed directly because the solution itself is too complicated. Therefore, the asymptotic approximation techniques in Section 3.3 are employed to transform the exact solution to the asymptotic solution (i.e. ray solution). The calculation of EM field by using the asymptotic solution is less complicated than the exact solution. Surprisingly, the asymptotic solution can be converted into the classical UTD format but it is different in the Fock-type integral function. Unlike the PEC Fock-type integral function of the classical UTD format, the new 3-D impedance Fock-type integral function consists of many important terms inside the integral. The details of the new 3-D impedance Fock-type integral function will be explained in Section 3.4 of this chapter.

3.2 Exact Solution for EM Wave Scattered from an Impedance Cylinder

The problem of the electromagnetic wave (EM) scattered from an impedance cylinder is illustrated in Fig. 3.1. The electric current J_z and the magnetic current M_z are located at the source position as shown in Fig. 3.1(a). The P' and P denote the source and the observation locations. The ρ and ρ' denote the radial distances from the axis of the cylinder to the observation and source points, respectively. The ϕ and ϕ' denote the

observation and source angles, both angles are measured from x-axis to the vector $\hat{\rho}$ and $\hat{\rho}'$, respectively. The z and z' denote the source and observation heights, respectively. The impedance cylinder is employed to represent the actual problem. For instance, the single layer material coated PEC cylinder is shown in Fig. 2.1 (b). Moreover, for other actual problems such as the multilayer material coated PEC cylinder, the proposed solutions require only the closed-form solution to estimate the surface impedance (Z_s).

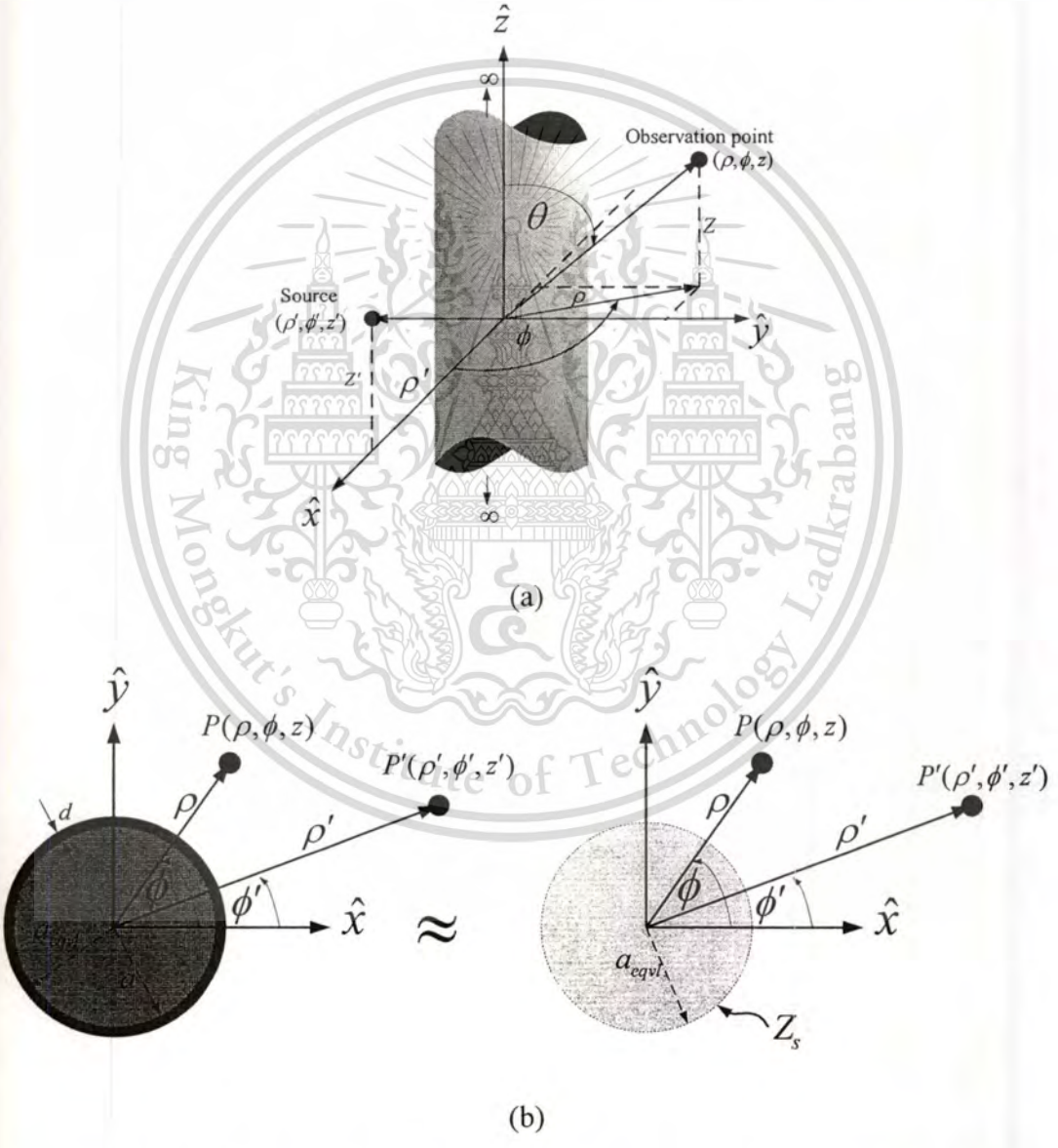

Figure 3.1 Impedance cylinder problem: (a) Perspective view, (b) Top view of a material coated PEC cylinder and its equivalent.

In the cylindrical coordinate system, the scalar potential functions A_z and M_z satisfy the inhomogeneous scalar wave equations [21], [22] and [34] as

$$\left(\nabla^2 + k^2\right) A_z^{J_z} = -\mu_0 J_z \tag{3.1a}$$

and

$$\left(\nabla^2 + k^2\right) F_z^{M_z} = -\varepsilon_0 M_z . \tag{3.1b}$$

In case of the electric current source excitation (J_z) and without magnetic source excitation in the considered region, let consider $J_z \neq 0$ and $M_z = 0$. Equation (3.1) can be written as

$$\left(\nabla^2 + k^2\right)\begin{bmatrix} A_z^{J_z} \\ F_z^{J_z} \end{bmatrix} = -\begin{bmatrix} \mu_0 J_z \\ 0 \end{bmatrix}. \tag{3.2}$$

The magnetic current source (M_z) without electric current source excitation in the considered region, let $M_z \neq 0$ and $J_z = 0$. Equation (3.1) can be written as

$$\left(\nabla^2 + k^2\right)\begin{bmatrix} A_z^{M_z} \\ F_z^{M_z} \end{bmatrix} = -\begin{bmatrix} 0 \\ \varepsilon_0 M_z \end{bmatrix}. \tag{3.3}$$

From Equations (3.2) and (3.3), the solutions of the differential equation can be determined using the 3-D Green's function technique. The 3-D Green's functions satisfy the same differential equations of Equations (3.2) and (3.3).

For $J_z \neq 0$ and $M_z = 0$, the inhomogeneous and homogeneous differential equations can be written as

$$\left(\nabla^2 + k^2\right)\begin{bmatrix} G^{A_z^{J_z}}(R/R') \\ G^{F_z^{J_z}}(R/R') \end{bmatrix} = \begin{bmatrix} -\dfrac{\delta(\rho-\rho')}{\rho}\delta(\phi-\phi')\delta(z-z') \\ 0 \end{bmatrix}. \tag{3.4}$$

For $M_z \neq 0$ and $J_z = 0$, the inhomogeneous and homogeneous differential equations can be written as

$$\left(\nabla^2 + k^2\right)\begin{bmatrix} G^{A_z^{M_z}}(R/R') \\ G^{F_z^{M_z}}(R/R') \end{bmatrix} = \begin{bmatrix} 0 \\ -\dfrac{\delta(\rho-\rho')}{\rho}\delta(\phi-\phi')\delta(z-z') \end{bmatrix}, \tag{3.5}$$

where $\delta(\rho-\rho')$, $\delta(\phi-\phi')$ and $\delta(z-z')$ denote the Dirac delta functions. The Dirac delta function is used to represent the source behavior which can be found in Appendix A. Let's consider

$$(J_z, M_z) = \delta(\bar{R}-\bar{R}') = \frac{\delta(\rho-\rho')}{\rho}\delta(\phi-\phi')\delta(z-z') \tag{3.6}$$

and substituting Equation (3.4) into (3.2) and (3.5) into (3.3), respectively. The relation between point current sources, the 3-D Green's functions and potential functions [22], are as follows

$$A_z^{J_z} = \mu_0 J_z G^{A_z^{J_z}}(R/R'), \tag{3.7a}$$

$$F_z^{J_z} = \varepsilon_0 J_z G^{F_z^{J_z}}(R/R'), \tag{3.7b}$$

$$A_z^{M_z} = \mu_0 M_z G^{A_z^{M_z}}(R/R') \tag{3.7c}$$

and

$$F_z^{M_z} = \varepsilon_0 M_z G^{F_z^{M_z}}(R/R') \tag{3.7d}$$

where ρ, ρ', ϕ, ϕ', Z and Z' denote the radial distance, angle and height of the observation and source locations, respectively. The separation of variable technique is employed to determine the solutions. The details of derivation are shown in Appendix A. The 3-D Green's function for EM wave propagation considering in ϕ direction [22] can be written in the integral forms as

$$G^{A_z^{J_z,M_z},F_z^{J_z,M_z}}(R/R') = \frac{1}{4\pi^2}\int_{C_v}\int_{C_{k_z}} e^{-jk_z(z-z')}e^{-jv(\phi-\phi')}\left(\tilde{G}_\rho^{A_z^{J_z,M_z},F_z^{J_z,M_z}}(\rho,\rho',v,k_z,k_\rho)\right)dvdk_z \tag{3.8}$$

Those 3-D Green's functions in Equation (3.7) consist of the radial Green's functions $\tilde{G}_{\rho}^{A_z^{J_z},M_z,F_z^{J_z},M_z}(\rho,\rho',v,k_z,k_\rho)$ which are called the spectral amplitudes of the spectral integrals, Green's function in z-domain $\tilde{G}_z(z,z')$ and angular Green's function $\tilde{G}_\phi(\phi,\phi')$. The radial Green's function for Equation (3.4)-(3.6) can be written in the form

$$\begin{bmatrix}\tilde{G}_{\rho}^{A_z^{J_z}}\\ \tilde{G}_{\rho}^{F_z^{M_z}}\end{bmatrix}=-\left(\frac{j\pi}{2}\right)\left(J_v(k_\rho\rho_<)+\begin{bmatrix}C_A^{J_z}\\ C_F^{M_z}\end{bmatrix}H_v^{(2)}(k_\rho\rho_<)\right)H_v^{(2)}(k_\rho\rho_>), \tag{3.9a}$$

and the remaining terms can be written as

$$\begin{bmatrix}\tilde{G}_{\rho}^{F_z^{J_z}}\\ \tilde{G}_{\rho}^{A_z^{M_z}}\end{bmatrix}=\begin{bmatrix}C_F^{J_z}\\ C_A^{M_z}\end{bmatrix}H_v^{(2)}(k_\rho\rho_>). \tag{3.9b}$$

The parameters k_ρ and k_z denote the wave number for wave propagation in radial direction (ρ-directed) and z direction (z-directed), respectively. The free-space wave number in the propagation direction can be written as $k^2=k_\rho^2+k_z^2$. The coefficients $C_A^{J_z}$, $C_F^{J_z}$, $C_A^{M_z}$ and $C_F^{M_z}$ are determined by enforcing the impedance boundary condition (IBC) on the total field at the surface of the impedance cylinder $\rho=a$. The IBC of the impedance cylinder is defined by

$$\hat{n}\times\hat{n}\times\bar{E}=-Z_s\hat{n}\times\bar{H} \tag{3.10a}$$

or

$$\begin{bmatrix}E_\phi\\ E_z\end{bmatrix}=Z_s\begin{bmatrix}-H_z\\ H_\phi\end{bmatrix}. \tag{3.10b}$$

The electric and magnetic fields are related with the surface impedance Z_s. From vector potential theory, the relation between EM-fields and vector potentials are defined as

$$\bar{\mathrm{E}}=-j\omega\bar{\mathrm{A}}-\frac{j}{\omega\mu\varepsilon}\nabla(\nabla.\bar{\mathrm{A}})-\frac{1}{\varepsilon}\nabla\times\bar{\mathrm{F}} \tag{3.11a}$$

and

$$\bar{\mathrm{H}} = -j\omega\bar{\mathrm{F}} - \frac{j}{\omega\mu\varepsilon}\nabla(\nabla.\bar{\mathrm{F}}) + \frac{1}{\mu}\nabla\times\bar{\mathrm{A}}. \tag{3.11b}$$

From Equation (3.11), using the relations between vector potentials and fields, the Green's function transformation in Equation (3.8), the potential functions can be rewritten as

$$\begin{bmatrix} A_z^{J_z} \\ A_z^{M_z} \\ F_z^{J_z} \\ F_z^{M_z} \end{bmatrix} = \frac{1}{4\pi^2}\int_{C_v}\int_{C_{k_z}} e^{-jk_z(z-z')}e^{-jv(\phi-\phi')} \begin{bmatrix} a_z^{J_z} \\ a_z^{M_z} \\ f_z^{J_z} \\ f_z^{M_z} \end{bmatrix} dvdk_z \tag{3.12}$$

where $a_z^{J_z}$, $a_z^{M_z}$, $f_z^{J_z}$ and $f_z^{M_z}$ denote the spectral amplitudes of the potential functions. Using the transformation in Equation (3.12), $E_\phi = -Z_s H_z$ can be written in term of radial potential functions as

$$\frac{jvk_z}{\omega\mu\varepsilon\rho}(a_z) = -\frac{1}{\varepsilon}\partial_\rho(f_z) + \frac{jZ_s}{\omega\mu\varepsilon}k_\rho^2(f_z) \tag{3.13a}$$

and $E_z = Z_s H_\phi$ can be written as

$$-\frac{j}{\omega\mu\varepsilon}k_\rho^2(a_z) + \frac{Z_s}{\mu}\partial_\rho(a_z) = \frac{jZ_s vk_z}{\omega\mu\varepsilon\rho}(f_z). \tag{3.13b}$$

Substituting Equations (3.8) and (3.9) into Equations (3.12) and cooperating with Equation (3.13), the unknown coefficients in the radial Green's functions can be simply obtained. For the current J_z, the coefficients $C_A^{J_z}$ and $C_F^{J_z}$ are defined as

$$C_A^{J_z} = -\frac{\left[R_H(\Lambda)R_J(\Lambda^{-1}) - C^2H_v^{(2)}(k_\rho a)J_v(k_\rho a)\right]}{\left[R_H(\Lambda)R_H(\Lambda^{-1}) - \left((C)H_v^{(2)}(k_\rho a)\right)^2\right]} \tag{3.14}$$

and

$$C_F^{J_z} = \left[\frac{jvk_z Z_0}{kk_\rho^2 a^2 \left[R_H(\Lambda) R_H(\Lambda^{-1}) - \left((C) H_v^{(2)}(k_\rho a) \right)^2 \right]} \right] H_v^{(2)}(k_\rho \rho'). \tag{3.15}$$

For the current M_z, the coefficients $C_A^{M_z}$ and $C_F^{M_z}$ are defined as

$$C_A^{M_z} = \left[\frac{-jvk_z Z_0^{-1}}{kk_\rho^2 a^2 \left[R_H(\Lambda) R_H(\Lambda^{-1}) - \left((C) H_v^{(2)}(k_\rho a) \right)^2 \right]} \right] H_v^{(2)}(k_\rho \rho') \tag{3.16}$$

and

$$C_F^{M_z} = -\frac{\left[R_H(\Lambda^{-1}) R_J(\Lambda) - C^2 H_v^{(2)}(k_\rho a) J_v(k_\rho a) \right]}{\left[R_H(\Lambda) R_H(\Lambda^{-1}) - \left((C) H_v^{(2)}(k_\rho a) \right)^2 \right]}, \tag{3.17}$$

where

$$R_H(\Lambda) = \left(H_v^{(2)'}(k_\rho a) - j \frac{\Lambda k_\rho}{k} H_v^{(2)}(k_\rho a) \right), \tag{3.18a}$$

$$R_H(\Lambda^{-1}) = \left(H_v^{(2)'}(k_\rho a) - j \frac{\Lambda^{-1} k_\rho}{k} H_v^{(2)}(k_\rho a) \right), \tag{3.18b}$$

$$R_J(\Lambda) = \left(J_v'(k_\rho a) - j \frac{\Lambda k_\rho}{k} J_v(k_\rho a) \right), \tag{3.18c}$$

$$R_J(\Lambda^{-1}) = \left(J_v'(k_\rho a) - j \frac{\Lambda^{-1} k_\rho}{k} J_v(k_\rho a) \right), \tag{3.18d}$$

and

$$C = \left(\frac{vk_z}{kk_\rho a} \right). \tag{3.18e}$$

The Λ denotes the normalized surface impedance to the intrinsic impedance of free space (i.e. $\Lambda = z_s / z_0$). $J_v(k_\rho a)$ and $J_v'(k_\rho a)$ denote the Bessel function and its

derivative with respect to the argument. $H_\nu^{(2)}(k_\rho a)$ and $H_\nu^{(2)'}(k_\rho a)$ denote the second kind Hankel function and its derivative with respect to the argument $\left(\frac{\partial}{\partial(k_\rho a)}\right)$. The radial scalar potential functions can be written as $a_z^{J_z} = \mu_0 J_z \tilde{G}_\rho^{A_z^{J_z}}$, $f_z^{J_z} = \varepsilon_0 J_z \tilde{G}_\rho^{F_z^{J_z}}$, $a_z^{M_z} = \mu_0 M_z \tilde{G}_\rho^{A_z^{M_z}}$ and $f_z^{M_z} = \varepsilon_0 M_z \tilde{G}_\rho^{F_z^{M_z}}$. From vector potential in Equation (3.11), the electric and magnetic fields can be written as

$$E_\rho = -\frac{j}{\omega\mu\varepsilon}\frac{\partial}{\partial\rho}\left(\frac{\partial(A_z)}{\partial z}\right) - \frac{1}{\varepsilon}\left(\frac{1}{\rho}\frac{\partial(F_z)}{\partial\phi}\right), \qquad H_\rho = -\frac{j}{\omega\mu\varepsilon}\frac{\partial}{\partial\rho}\left(\frac{\partial(F_z)}{\partial z}\right) + \frac{1}{\mu}\left(\frac{1}{\rho}\frac{\partial(A_z)}{\partial\phi}\right),$$

$$E_\phi = -\frac{j}{\omega\mu\varepsilon\rho}\frac{\partial}{\partial\phi}\left(\frac{\partial(A_z)}{\partial z}\right) + \frac{1}{\varepsilon}\left(\frac{\partial(F_z)}{\partial\rho}\right), \quad H_\phi = -\frac{j}{\omega\mu\varepsilon\rho}\frac{\partial}{\partial\phi}\left(\frac{\partial(F_z)}{\partial z}\right) - \frac{1}{\mu}\left(\frac{\partial(A_z)}{\partial\rho}\right),$$

$$E_z = -j\omega A_z - \frac{j}{\omega\mu\varepsilon}\frac{\partial^2}{\partial^2 z}(A_z) \quad \text{and} \quad H_z = -j\omega F_z - \frac{j}{\omega\mu\varepsilon}\frac{\partial^2}{\partial^2 z}(F_z).$$

Using the transformation in Equation (3.12), the properties of $\frac{\partial}{\partial z} = -jk_z$ and $\frac{\partial}{\partial\phi} = -j\nu$ are employed. The radial components or spectral amplitudes of electric and magnetic fields can be written as

$$\begin{bmatrix} e_\rho^{J_z,M_z} \\ h_\rho^{J_z,M_z} \end{bmatrix} = -\frac{j}{\omega\mu\varepsilon}\begin{bmatrix} -jk_z\frac{\partial}{\partial\rho} & \frac{-\omega\mu\nu}{\rho} \\ \frac{\omega\varepsilon\nu}{\rho} & -jk_z\frac{\partial}{\partial\rho} \end{bmatrix}\begin{bmatrix} a_z^{J_z,M_z} \\ f_z^{J_z,M_z} \end{bmatrix}, \tag{3.19a}$$

$$\begin{bmatrix} e_\phi^{J_z,M_z} \\ h_\phi^{J_z,M_z} \end{bmatrix} = -\frac{j}{\omega\mu\varepsilon\rho}\begin{bmatrix} -k_z\nu & j\omega\mu\rho\frac{\partial}{\partial\rho} \\ -j\omega\varepsilon\rho\frac{\partial}{\partial\rho} & -k_z\nu \end{bmatrix}\begin{bmatrix} a_z^{J_z,M_z} \\ f_z^{J_z,M_z} \end{bmatrix} \tag{3.19b}$$

and

$$\begin{bmatrix} e_z^{J_z,M_z} \\ h_z^{J_z,M_z} \end{bmatrix} = -\frac{j}{\omega\mu\varepsilon}(k_\rho^2)\begin{bmatrix} a_z^{J_z,M_z} \\ f_z^{J_z,M_z} \end{bmatrix}. \tag{3.19c}$$

The electric and magnetic fields can be calculated from two potential functions $a_z^{J_z,M_z}$ and $f_z^{J_z,M_z}$ of both electric and magnetic current sources. All EM field components can be written as

$$\begin{bmatrix} E_\rho^{J_z,M_z} \\ H_\rho^{J_z,M_z} \end{bmatrix} = \frac{1}{4\pi^2} \int_{C_\nu} \int_{C_{k_z}} e^{-jk_z(z-z')} e^{-j\nu(\phi-\phi')} \left\{ \frac{-j}{\omega\mu\varepsilon} \begin{bmatrix} -jk_z \frac{\partial}{\partial\rho} & \frac{-\omega\mu\nu}{\rho} \\ \frac{\omega\varepsilon\nu}{\rho} & -jk_z \frac{\partial}{\partial\rho} \end{bmatrix} \begin{bmatrix} a_z^{J_z,M_z} \\ f_z^{J_z,M_z} \end{bmatrix} \right\} d\nu dk_z, \quad (3.20a)$$

$$\begin{bmatrix} E_\phi^{J_z,M_z} \\ H_\phi^{J_z,M_z} \end{bmatrix} = \frac{1}{4\pi^2} \int_{C_\nu} \int_{C_{k_z}} e^{-jk_z(z-z')} e^{-j\nu(\phi-\phi')} \left\{ \frac{-j}{\omega\mu\varepsilon} \begin{bmatrix} \frac{-k_z\nu}{\rho} & j\omega\mu \frac{\partial}{\partial\rho} \\ -j\omega\varepsilon \frac{\partial}{\partial\rho} & \frac{-k_z\nu}{\rho} \end{bmatrix} \begin{bmatrix} a_z^{J_z,M_z} \\ f_z^{J_z,M_z} \end{bmatrix} \right\} d\nu dk_z \quad (3.20b)$$

and

$$\begin{bmatrix} E_z^{J_z,M_z} \\ H_z^{J_z,M_z} \end{bmatrix} = \frac{1}{4\pi^2} \int_{C_\nu} \int_{C_{k_z}} e^{-jk_z(z-z')} e^{-j\nu(\phi-\phi')} \left\{ \frac{-j}{\omega\mu\varepsilon} (k_\rho^2) \begin{bmatrix} a_z^{J_z,M_z} \\ f_z^{J_z,M_z} \end{bmatrix} \right\} d\nu dk_z. \quad (3.20c)$$

3.3 Asymptotic Solution for EM Wave Scattered from an Impedance Cylinder

An asymptotic solution of the EM wave scattered from impedance cylinder can be constructed from large argument approximation of the Bessel and Hankel functions and also from ray path transformations. Fig. 3.2 illustrates the source/observation locations, ray path and ray parameters. Here s_i and s_d denote the 3-D incident and diffracted ray paths, respectively. The t_d denotes the 3-D surface diffracted ray path. The Q_1 and Q_2 denote incident and diffracted field points on the surface, respectively. To transform the 3-D ray path into the 2-D ray path, the $s = s_d \cos(\alpha_1)$, $s^{inc.} = s_i \cos(\alpha_1)$ and $t = t_d \cos(\alpha_1)$ are usually employed to construct the asymptotic solution. The drawing of 2-D ray path, ray parameters and its transformation are shown in Fig. 3.3. From Equations (3.14) to (3.17), the coefficients of the potential functions consist of the Bessel and Hankel functions with argument $k_\rho a$ where $\rho \to a$.

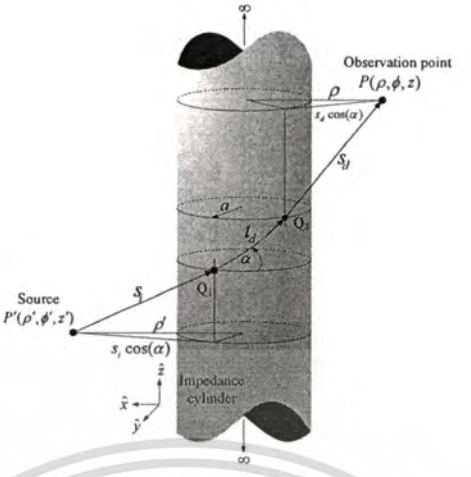

Figure 3.2 Ray parameters and ray paths

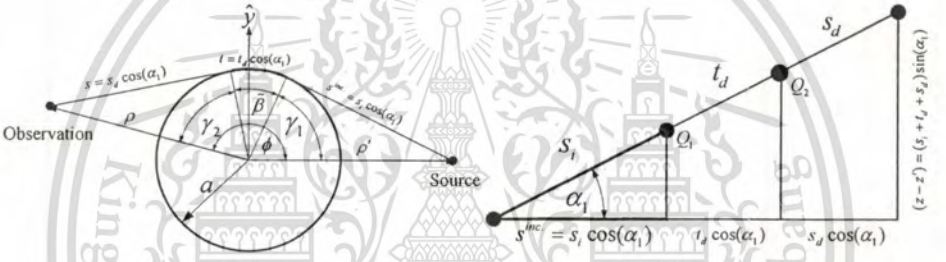

Figure 3.3 Ray path and its ray transformations.

Large argument approximation of the Bessel and Hankel functions [21], [32]-[34] (i.e. $k_\rho a \to$ large), properties of $H_v^{(2)}(k_\rho a)=\dfrac{j}{m_t\sqrt{\pi}}w_2(\tau)$, $H_v^{(2)\prime}(k_\rho a)=\dfrac{-j}{m_t^{\,2}\sqrt{\pi}}w_2'(\tau)$, $J_v(k_\rho a)=\dfrac{1}{m_t\sqrt{\pi}}V(\tau)$ and $J_v'(k_\rho a)=-\dfrac{1}{m_t^{\,2}\sqrt{\pi}}V'(\tau)$ are employed in shadow zone of the asymptotic analysis. Also, the transformations of the integral within the transition region of $v=k\cos(\alpha)a+m\tau$, $k_z=k\sin(\alpha)$, $k_\rho=k\cos(\alpha)$ and $m_t=m\cos(\alpha)$ are employed in this step. Equations (3.14)-(3.17) can be written as

$$R_H(\Lambda)=\frac{-j}{m_t^{\,2}\sqrt{\pi}}\left(w_2'(\tau)+jm_t\Lambda\cos(\alpha)w_2(\tau)\right) \tag{3.21a}$$

$$R_H(\Lambda^{-1}) = \frac{-j}{m_t^2\sqrt{\pi}}\left(w_2'(\tau) + jm_t\Lambda^{-1}\cos(\alpha)w_2(\tau)\right) \tag{3.21b}$$

$$R_J(\Lambda) = -\frac{1}{m_t^2\sqrt{\pi}}\left(V'(\tau) + jm_t\Lambda\cos(\alpha)V(\tau)\right) \tag{3.21c}$$

$$R_J(\Lambda^{-1}) = -\frac{1}{m_t^2\sqrt{\pi}}\left(V'(\tau) + jm_t\Lambda^{-1}\cos(\alpha)V(\tau)\right) \tag{3.21d}$$

and $$C = \left(\sin(\alpha)\right). \tag{3.21e}$$

The approximate closed-form of two Debye approximations of the Hankel functions at the observation and source points respectively are employed as

$$H_\nu^{(2)}(k\cos(\alpha)\rho) \approx \sqrt{\frac{2}{\pi k\cos(\alpha)s^d\cos(\alpha_1)}}e^{-j(k_\rho s^d\cos(\alpha_1)-(k\cos(\alpha)a+m_t\tau)\gamma_2-\frac{\pi}{4})}, \tag{3.22a}$$

$$H_\nu^{(2)}(k\cos(\alpha)\rho') \approx \sqrt{\frac{2}{\pi k\cos(\alpha)s^l\cos(\alpha_1)}}e^{-j(k_\rho s^l\cos(\alpha_1)-(k\cos(\alpha)a+m_t\tau)\gamma_1-\frac{\pi}{4})}. \tag{3.22b}$$

The asymptotic forms for the derivative of Hankel function are written as

$$\frac{\partial\left(H_\nu^{(2)}(k\cos(\alpha)\rho)\right)}{\partial\left(k_\rho\rho\right)} = H_\nu^{(2)'}(k\cos(\alpha)\rho) \approx \sqrt{\frac{2}{\pi k_\rho s}}e^{-j(k_\rho s-(k\cos(\alpha)a+m_t\tau)\gamma+\frac{\pi}{4})}, \tag{3.23a}$$

$$\frac{\partial\left(H_\nu^{(2)}(k\cos(\alpha)\rho)\right)}{\partial\rho} \approx k_\rho\sqrt{\frac{2}{\pi k_\rho s}}e^{-j(k_\rho s-(k\cos(\alpha)a+m_t\tau)\gamma+\frac{\pi}{4})} \tag{3.23b}$$

or can be written as

$$\frac{\partial\left(H_\nu^{(2)}(k\cos(\alpha)\rho)\right)}{\partial\rho} = -jk_\rho H_\nu^{(2)}(k\cos(\alpha)\rho)_{Asymptotic}. \tag{3.23c}$$

In the scattering problem, the observation and source distances are very large comparing to the wavelength. Let $\rho\to\infty$, $k_z = k\sin(\alpha)$, $k_\rho = k\cos(\alpha)$, the Equation (3.20) can be simplified as

$$\begin{bmatrix} E_\rho \\ H_\rho \end{bmatrix} = \frac{1}{4\pi^2} \int_{C_\nu} \int_{C_{k_z}} e^{-jk_z(z-z')} e^{-j\nu(\phi-\phi')} \left\{ \frac{-j}{\omega\mu\varepsilon} \begin{bmatrix} -k^2 \sin(\alpha)\cos(\alpha) & \simeq 0 \\ \simeq 0 & -k^2 \sin(\alpha)\cos(\alpha) \end{bmatrix} \begin{bmatrix} a_z \\ f_z \end{bmatrix} \right\} dv dk_z , \quad (3.24a)$$

$$\begin{bmatrix} E_\phi \\ H_\phi \end{bmatrix} = \frac{1}{4\pi^2} \int_{C_\nu} \int_{C_{k_z}} e^{-jk_z(z-z')} e^{-j\nu(\phi-\phi')} \left\{ \frac{-j}{\omega\mu\varepsilon} \begin{bmatrix} \simeq 0 & Z_0 k^2 \cos(\alpha) \\ -\dfrac{k^2 \cos(\alpha)}{Z_0} & \simeq 0 \end{bmatrix} \begin{bmatrix} a_z \\ f_z \end{bmatrix} \right\} dv dk_z \quad (3.24b)$$

and

$$\begin{bmatrix} E_z \\ H_z \end{bmatrix} = \frac{1}{4\pi^2} \int_{C_\nu} \int_{C_{k_z}} e^{-jk_z(z-z')} e^{-j\nu(\phi-\phi')} \left\{ \frac{-j}{\omega\mu\varepsilon} \left(k^2 \cos^2(\alpha)\right) \begin{bmatrix} a_z \\ f_z \end{bmatrix} \right\} dv dk_z . \quad (3.24c)$$

It is observed that in Equation (2.24), the EM fields satisfy TEM wave radiation of $E_z \approx -Z_0 H_\phi$ and $E_\phi \approx Z_0 H_z$ in principal direction with $\alpha = 0$ (measured from horizontal line), $E_\rho \approx 0$ and $H_\rho \approx 0$, respectively.

Generally, the integrals in the EM field equations consist of the incident field and scattered field terms. The first term of $J_\nu(k_\rho \rho_<) H_\nu^{(2)}(k_\rho \rho_>)$ in Equation (3.9a) of potential functions $A_z^{J_z}$ and $F_z^{M_z}$ due to J_z and M_z excitations respectively represents the incident wave. The second terms $\begin{bmatrix} C_A^{J_z} \\ C_F^{M_z} \end{bmatrix} H_\nu^{(2)}(k_\rho \rho_<) H_\nu^{(2)}(k_\rho \rho_>)$ of Equation (3.9a) and the first term $\begin{bmatrix} C_F^{J_z} \\ C_A^{M_z} \end{bmatrix} H_\nu^{(2)}(k_\rho \rho_>)$ of Equation (3.9b) represent the scattered wave.

The steepest decent path (SDP) method is generally employed to evaluate the integrals in the scattered field terms of Equation (3.24). The SDP in the Appendix B is defined as

$$I(k_0) = \int_{SDP} F(\alpha) e^{k_0 f(\alpha)} d\alpha \approx \sqrt{\frac{-2\pi}{k_0 f''(\alpha_s)}} F(\alpha_s) e^{k_0 f(\alpha_s)} \quad (3.25a)$$

with $f'(\alpha_s) = 0$ and $f''(\alpha_s) \neq 0$. Using the SDP together with the ray transformation as shown in Fig. 3.3, the asymptotic solution can be achieved.

3.3.1 J_z Source Excitation

Using large approximation of the observation point distance $\rho \to \infty$. The spectral amplitudes of the EM fields (i.e. e_ρ, h_ρ, e_ϕ and h_ϕ) can be obtained from two spectral amplitudes of e_z and h_z. The relations can be written as

$$\begin{bmatrix} e_\rho \\ h_\rho \end{bmatrix} = -\tan(\alpha) \begin{bmatrix} e_z \\ h_z \end{bmatrix} \tag{3.26}$$

and

$$\begin{bmatrix} e_\phi \\ h_\phi \end{bmatrix} = \frac{1}{\cos(\alpha)} \begin{bmatrix} Z_0 h_z \\ -e_z / Z_0 \end{bmatrix}. \tag{3.27}$$

The asymptotic $E_z^{J_z}$ in shadow zone is achieved as

$$E_z^{J_z} = \frac{-jkZ_0}{4\pi} \left\{ 1^{st} + \cos^2(\alpha) \right. \\ \left. \times m\sqrt{\frac{2}{k}} \frac{e^{-j\frac{\pi}{4}}}{\sqrt{\pi}} \left[\int_\tau \left(X_A^{J_z} \right) e^{-jk\xi\tau} d\tau \right] \sqrt{\frac{1}{s_d s_i}} \sqrt{\frac{1}{(s_d + s_i + t_d)}} e^{-jks_i} e^{-jk(s_d + t_d)} \right\}. \tag{3.28}$$

The asymptotic $H_z^{J_z}$ in shadow zone is achieved as

$$H_z^{J_z} = \frac{-jk}{4\pi} \left\{ \cos^2(\alpha) \right. \\ \left. \times m\sqrt{\frac{2}{k}} \frac{e^{-j\frac{\pi}{4}}}{\sqrt{\pi}} \left[\int_\tau \left(X_F^{J_z} \right) e^{-jk\xi\tau} d\tau \right] \sqrt{\frac{1}{s_d s_i}} \sqrt{\frac{1}{(s_d + s_i + t_d)}} e^{-jks_i} e^{-jk(s_d + t_d)} \right\}. \tag{3.29}$$

The 1st term in the Equations (3.28), (3.30) and (3.33) can be recognized as the incident wave from the source. The other field components can be written as

$$E_{\rho}^{J_z} = \frac{jkZ_0}{4\pi}\Bigg\{ \tan(\alpha)\left(1^{st}\right) + \sin(\alpha)\cos(\alpha) \times m\sqrt{\frac{2}{k}}\frac{e^{-j\frac{\pi}{4}}}{\sqrt{\pi}}\left[\int_{\tau}\left(X_A^{J_z}\right)e^{-j\xi\tau}d\tau\right]\sqrt{\frac{1}{s_d s_i}}\sqrt{\frac{1}{(s_d+s_i+t_d)}}e^{-jks_i}e^{-jk(s_d+t_d)}\Bigg\} \tag{3.30}$$

$$H_{\rho}^{J_z} = \frac{-jk}{4\pi}\Bigg\{ -sin(\alpha)\cos(\alpha) \times m\sqrt{\frac{2}{k}}\frac{e^{-j\frac{\pi}{4}}}{\sqrt{\pi}}\left[\int_{\tau}\left(X_F^{J_z}\right)e^{-j\xi\tau}d\tau\right]\sqrt{\frac{1}{s_d s_i}}\sqrt{\frac{1}{(s_d+s_i+t_d)}}e^{-jks_i}e^{-jk(s_d+t_d)}\Bigg\} \tag{3.31}$$

$$E_{\phi}^{J_z} = \frac{-jkZ_0}{4\pi}\Bigg\{ \cos(\alpha) \times m\sqrt{\frac{2}{k}}\frac{e^{-j\frac{\pi}{4}}}{\sqrt{\pi}}\left[\int_{\tau}\left(X_F^{J_z}\right)e^{-j\xi\tau}d\tau\right]\sqrt{\frac{1}{s_d s_i}}\sqrt{\frac{1}{(s_d+s_i+t_d)}}e^{-jks_i}e^{-jk(s_d+t_d)}\Bigg\} \tag{3.32}$$

$$H_{\phi}^{J_z} = \frac{-jk}{4\pi}\Bigg\{ -\frac{\left(1^{st}\right)}{\cos(\alpha)} - \cos(\alpha) \times m\sqrt{\frac{2}{k}}\frac{e^{-j\frac{\pi}{4}}}{\sqrt{\pi}}\left[\int_{\tau}\left(X_A^{J_z}\right)e^{-j\xi\tau}d\tau\right]\sqrt{\frac{1}{s_d s_i}}\sqrt{\frac{1}{(s_d+s_i+t_d)}}e^{-jks_i}e^{-jk(s_d+t_d)}\Bigg\} \tag{3.33}$$

3.3.2 M_z Source Excitation

The asymptotic $E_z^{M_z}$ in shadow zone is achieved as

$$E_z^{M_z} = \frac{-jk}{4\pi}\Bigg\{ \cos^2(\alpha) \times m\sqrt{\frac{2}{k}}\frac{e^{-j\frac{\pi}{4}}}{\sqrt{\pi}}\left[\int_{\tau}\left(X_A^{M_z}\right)e^{-j\xi\tau}d\tau\right]\sqrt{\frac{1}{s_d s_i}}\sqrt{\frac{1}{(s_d+s_i+t_d)}}e^{-jks_i}e^{-jk(s_d+t_d)}\Bigg\} \tag{3.34}$$

The asymptotic $H_z^{M_z}$ in shadow zone is achieved as

$$H_z^{M_z} = \frac{-jk}{4\pi Z_0}\left\{ 1^{st} + \cos^2(\alpha) \right.$$
$$\left. \times m\sqrt{\frac{2}{k}}\frac{e^{-j\frac{\pi}{4}}}{\sqrt{\pi}}\left[\int_\tau \left(X_F^{M_z}\right)e^{-j\xi\tau}d\tau\right]\sqrt{\frac{1}{s_d s_i}}\sqrt{\frac{1}{(s_d+s_i+t_d)}}e^{-jks_i}e^{-jk(s_d+t_d)} \right\}. \quad (3.35)$$

The first term (1^{st}) in the Equations (3.25), (3.37) and (3.38) can be recognized as the incident wave from source. All field components can be written as

$$E_\rho^{M_z} = \frac{jk}{4\pi}\left\{ \sin(\alpha)\cos(\alpha) \right.$$
$$\left. \times m\sqrt{\frac{2}{k}}\frac{e^{-j\frac{\pi}{4}}}{\sqrt{\pi}}\left[\int_\tau \left(X_A^{M_z}\right)e^{-j\xi\tau}d\tau\right]\sqrt{\frac{1}{s_d s_i}}\sqrt{\frac{1}{(s_d+s_i+t_d)}}e^{-jks_i}e^{-jk(s_d+t_d)} \right\}, \quad (3.36)$$

$$H_\rho^{M_z} = \frac{jk}{4\pi Z_0}\sin(\alpha)\left\{ \frac{1^{st}}{\cos(\alpha)} + \cos(\alpha) \right.$$
$$\left. \times m\sqrt{\frac{2}{k}}\frac{e^{-j\frac{\pi}{4}}}{\sqrt{\pi}}\left[\int_\tau \left(X_F^{M_z}\right)e^{-j\xi\tau}d\tau\right]\sqrt{\frac{1}{s_d s_i}}\sqrt{\frac{1}{(s_d+s_i+t_d)}}e^{-jks_i}e^{-jk(s_d+t_d)} \right\}, \quad (3.37)$$

$$E_\phi^{M_z} = \frac{-jk}{4\pi}\left\{ \frac{1^{st}}{\cos(\alpha)} + \cos(\alpha) \right.$$
$$\left. \times m\sqrt{\frac{2}{k}}\frac{e^{-j\frac{\pi}{4}}}{\sqrt{\pi}}\left[\int_\tau \left(X_F^{M_z}\right)e^{-j\xi\tau}d\tau\right]\sqrt{\frac{1}{s_d s_i}}\sqrt{\frac{1}{(s_d+s_i+t_d)}}e^{-jks_i}e^{-jk(s_d+t_d)} \right\} \quad (3.38)$$

and

$$H_\phi^{M_z} = \frac{jk}{4\pi Z_0}\left\{ \cos(\alpha) \right.$$
$$\left. \times m\sqrt{\frac{2}{k}}\frac{e^{-j\frac{\pi}{4}}}{\sqrt{\pi}}\left[\int_\tau \left(X_A^{M_z}\right)e^{-j\xi\tau}d\tau\right]\sqrt{\frac{1}{s_d s_i}}\sqrt{\frac{1}{(s_d+s_i+t_d)}}e^{-jks_i}e^{-jk(s_d+t_d)} \right\}. \quad (3.39)$$

The new integrands for the integral of Fock-type integral functions are defined as

$$X_A^{J_z} = \frac{\left[X_w(\tau,\Lambda)X_V(\tau,\Lambda^{-1}) - \left(X_C\right)^2 w_2(\tau)V(\tau)\right]}{\left[X_w(\tau,\Lambda)X_w(\tau,\Lambda^{-1}) - \left(X_C w_2(\tau)\right)^2\right]}, \tag{3.40a}$$

$$X_F^{J_z} = \left[\frac{jm\cos(\alpha)\sin(\alpha)}{\left[X_w(\tau,\Lambda)X_w(\tau,\Lambda^{-1}) - \left(X_C w_2(\tau)\right)^2\right]}\right], \tag{3.40b}$$

$$X_A^{M_z} = \left[\frac{jm\cos(\alpha)\sin(\alpha)}{\left[X_w(\tau,\Lambda)X_w(\tau,\Lambda^{-1}) - \left(X_C w_2(\tau)\right)^2\right]}\right], \tag{3.40c}$$

$$X_F^{M_z} = \frac{\left[X_w(\tau,\Lambda^{-1})X_V(\tau,\Lambda) - \left(X_C\right)^2 w_2(\tau)V(\tau)\right]}{\left[X_w(\tau,\Lambda)X_w(\tau,\Lambda^{-1}) - \left(X_C w_2(\tau)\right)^2\right]}, \tag{3.40d}$$

where

$$X_w(\tau,\Lambda) = \left(w_2'(\tau) + jm\Lambda\cos^2(\alpha)w_2(\tau)\right), \tag{3.41a}$$

$$X_w(\tau,\Lambda^{-1}) = \left(w_2'(\tau) + jm\Lambda^{-1}\cos^2(\alpha)w_2(\tau)\right), \tag{3.41b}$$

$$X_V(\tau,\Lambda) = \left(V'(\tau) + jm\Lambda\cos^2(\alpha)V(\tau)\right), \tag{3.41c}$$

$$X_V(\tau,\Lambda^{-1}) = \left(V'(\tau) + jm\Lambda^{-1}\cos^2(\alpha)V(\tau)\right), \tag{3.41d}$$

and

$$X_C = m\cos(\alpha)\sin(\alpha). \tag{3.41e}$$

Note that, the Equations 3.24, 3.26 and 3.27 restrict only to the far field approximation of the scattering problem.

3.4 Uniform Geometrical Theory of Diffraction (UTD) Solution for an Impedance Cylinder

3.4.1 Ray Transformation

To obtain the unit vector of the UTD method, the ray transformations between the cylindrical coordinate (ρ,ϕ,z) and the ray fixed coordinate system $(\hat{s},\hat{e}_{\perp}^{i,r},\hat{e}_{\parallel}^{i,r})$ are employed. The ray coordinate in lit zone consists of $\hat{s}^{i,r},\hat{e}_{\perp}^{i,r}$ and $\hat{e}_{\parallel}^{i,r}$. And $\hat{s}^{i,r}=\hat{e}_{\perp}^{i,r}\times\hat{e}_{\parallel}^{i,r}$ where $\hat{s}^{i,r}$ denotes the wave propagation direction. The $\hat{e}_{\parallel}^{i,r}$ and $\hat{e}_{\perp}^{i,r}$ denote the unit vectors of parallel and perpendicular components of incident and reflection unit vectors, refer to the planes of incident and reflection wave, respectively. The ray coordinate in shadow zone consists of $\hat{s}^{i,d},\hat{n}_{1,2}$ and $\hat{b}_{1,2}$. $\hat{s}^{i,d}=\hat{b}_{1,2}\times\hat{n}_{1,2}$ where $\hat{s}^{i,r}$ denotes the wave propagation direction. The $\hat{b}_1\,\hat{n}_1$ and $\hat{b}_2\,\hat{n}_2$ denote the unit vectors of incident and diffraction, respectively. The details of derivation of the ray fixed coordinate system are presented [30] and in Appendix D. The summary of the ray transformations is concluded in this section. Generally, the diffracted field can be written as

$$\vec{E}^d=\hat{\rho}E_\rho^d+\hat{\phi}E_\phi^d+\hat{z}E_z^d=\hat{n}_2E_n^d+\hat{b}_2E_b^d \tag{3.42a}$$

where

$$E_n^d=-\sin(\beta)E_\phi^d+\cos(\beta)E_\rho^d \tag{3.43}$$

and

$$E_b^d=\sin(\theta_i)E_z^d-\cos(\beta)\cos(\theta_i)E_\phi^d-\sin(\beta)\cos(\theta_i)E_\rho^d. \tag{3.44}$$

The β denotes the angle between $\hat{\rho}$ and $\hat{n}_2$. The θ^i denotes the incident angle from z-axis. Using large approximation of the observation point distance $\rho\to\infty$, thus the $\beta\approx\frac{\pi}{2}$, the electric fields can be written as

$$E_n^d=-E_\phi^d, \tag{3.45}$$

$$E_b^d = \sin(\theta_i)E_z^d - \cos(\theta_i)E_\rho^d . \tag{3.46}$$

From Equation (3.26), thus

$$E_b^d = \frac{E_z^d}{\sin(\theta_i)} \tag{3.47}$$

Figure 3.4 Ray parameters.

It is noted that in the UTD method, $\cot^2(\theta_i) = \tan^2(\alpha) = T_0^2$ denotes the torsion factor of the ray twist around the cylinder. Using the UTD ray spreading factor of

$$\sqrt{\frac{1}{s_d s_i}}\sqrt{\frac{1}{(s_d + s_i + t_d)}} = \frac{1}{s_i}\sqrt{\frac{d\eta_1}{d\eta_2}}\sqrt{\frac{\rho_2^d}{s_d(s_d + \rho_2^d)}} \tag{3.48}$$

where

$$\sqrt{\frac{d\eta_1}{d\eta_2}} = \sqrt{\frac{s_i}{s_i + t_d}}, \tag{3.49}$$

$$\rho_2^d = s_i + t_d , \tag{3.50}$$

the 3-D UTD solution can be obtained. Moreover, the completed 3-D UTD solution for lit and shadow regions are constructed using the same procedure of [17] and [18]. The total field is continuous at the shadow boundary (SB). The final solutions are concluded below.

3.4.2 J_z Current Excitation

For the shadow zone, the UTD solution can be written as

$$E_b^d = \bar{E}^d \cdot \hat{b}_2 = \frac{-jkZ_0}{4\pi}\left\{ \left(\bar{E}^i(Q_1)\cdot\hat{b}_1\right) \times -\sqrt{m(Q_1)m(Q_2)}\sqrt{\frac{2}{k}}\left[\frac{e^{-j\frac{\pi}{4}}}{2\sqrt{\pi}\xi^d}\left[1-F(X^d)\right]+\hat{X}_A^{J_z}(\xi^d)\right]\sqrt{\frac{d\eta_1}{d\eta_2}}\sqrt{\frac{\rho_2^d}{s_d(s_d+\rho_2^d)}}e^{-jk(s^d+t_d)}\right\} \tag{3.51}$$

$$E_n^d = \bar{E}^d \cdot \hat{n}_2 = \frac{-jkZ_0}{4\pi}\left\{ \left(\bar{E}^i(Q_1)\cdot\hat{b}_1\right) \times \sqrt{m(Q_1)m(Q_2)}\sqrt{\frac{2}{k}}\left[\hat{X}_F^{J_z}(\xi^d)\right]\sqrt{\frac{d\eta_1}{d\eta_2}}\sqrt{\frac{\rho_2^d}{s_d(s_d+\rho_2^d)}}e^{-jk(s^d+t_d)}\right\} \tag{3.52}$$

$$\bar{E}^i(Q_1)\cdot\hat{b}_1 = E_b^i(Q_1) = -\sin(\theta^i)\frac{e^{-jks^i}}{s^i} \tag{3.53}$$

For the lit zone, the UTD solution can be written as

$$E_\perp(P) = \frac{-jkZ_0}{4\pi}\left\{ E_\perp^i(P) + \left(\bar{E}^i(Q_R)\cdot\hat{e}_\perp^i\right) \times -\sqrt{\frac{-4}{\xi^L}}e^{-j(\xi^L)^3/12}\left[\frac{e^{-j\frac{\pi}{4}}}{2\sqrt{\pi}\xi^L}\left[1-F(X^L)\right]+\hat{X}_A^{J_z}(\xi^L)\right]\sqrt{\frac{\rho_1^r\rho_2^r}{(\rho_1^r+s_r)(\rho_2^r+s_r)}}e^{-jk(s_r)}\right\} \tag{3.54}$$

$$E_{\parallel}(P)=\frac{-jkZ_0}{4\pi}\left\{\left(\bar{E}^i(Q_R)\cdot\hat{e}_{\perp}^i\right)\right.$$
$$\left.\times\sqrt{\frac{-4}{\xi^L}}e^{-j(\xi^L)^3/12}\left[\hat{X}_F^{J_z}(\xi^L)\right]\sqrt{\frac{\rho_1^r\rho_2^r}{(\rho_1^r+s_r)(\rho_2^r+s_r)}}e^{-jk(s_r)}\right\} \tag{3.55}$$

where $F(X^{d,L})$ is the Fresnel function of the shadow and the lit zone, respectively. The 3-D Fock-type integral functions are defined as

$$\hat{X}_A^{J_z}(\xi^{L,d})=\frac{e^{-j\frac{\pi}{4}}}{\sqrt{\pi}}\int_{\tau}\left(X_A^{J_z}\right)e^{-j\xi^{L,d}\tau}d\tau \tag{3.56}$$

$$\hat{X}_F^{J_z}(\xi^{L,d})=\frac{e^{-j\frac{\pi}{4}}}{\sqrt{\pi}}\int_{\tau}\left(X_F^{J_z}\right)e^{-j\xi^{L,d}\tau}d\tau\,. \tag{3.57}$$

It is observed that the incident field $E_b^i(Q_1)$ at point Q_1 creates both E_b^d and E_n^d. Note that E_b^d is the coupling field or called cross polarization. The coupling fields vanish for the principal plane of the 2-D case (i.e. normal incident with $\alpha=0$). Moreover, in the case of PEC surface with $\Lambda=0$, the coupling fields also disappeared (i.e. $E_n^d=0$).

3.4.3 M_z Current Excitation

For the shadow zone, the UTD solution can be written as

$$E_b^d=\bar{E}^d\cdot\hat{b}_2=\frac{-jkZ_0}{4\pi}\left\{\left(\bar{E}^i(Q_1)\cdot\hat{n}_1\right)\right.$$
$$\left.\times\sqrt{m(Q_1)m(Q_2)}\sqrt{\frac{2}{k}}\left[\hat{X}_A^{M_z}(\xi^d)\right]\sqrt{\frac{d\eta_1}{d\eta_2}}\sqrt{\frac{\rho_2^d}{s_d(s_d+\rho_2^d)}}e^{-jk(s_d+t_d)}\right\} \tag{3.58}$$

$$E_n^d = \bar{E}^d \cdot \hat{n}_2 = \frac{-jkZ_0}{4\pi}\left\{ \left(\bar{E}^i(Q_1)\cdot\hat{n}_1\right) \right.$$
$$\left. \times -\sqrt{m(Q_1)m(Q_2)}\sqrt{\frac{2}{k}}\left[\frac{e^{-j\frac{\pi}{4}}}{2\sqrt{\pi}\xi^d}\left[1-F(X^d)\right]+\hat{X}_F^{M_z}(\xi^d)\right]\sqrt{\frac{d\eta_1}{d\eta_2}}\sqrt{\frac{\rho_2^d}{s_d(s_d+\rho_2^d)}}e^{-jk(s_d+t_d)} \right\} \tag{3.59}$$

$$\bar{H}^i(Q_1)\cdot\hat{b}_1 = H_b^i(Q_1) = E_n^i(Q_1)/Z_0 = -\sin(\theta^i)\frac{e^{-jks^i}}{s^i}. \tag{3.60}$$

It is clear that Equation (3.60), the E_b^d and E_n^d can be obtained from M_z current excitation. The $E_n^i(Q_1)$ from $\bar{H}^i(Q_1)\cdot\hat{b}_1$ creates both E_b^d and E_n^d. And E_b^d denotes the cross polarization. For the lit zone, the UTD solution can be written as

$$E_\perp(P) = \bar{E}\cdot\hat{e}_\perp^i = \frac{-jkZ_0}{4\pi}\left\{ \left(\bar{E}^i(Q_R)\cdot\hat{e}_\parallel^i\right) \right.$$
$$\left. \times\sqrt{\frac{-4}{\xi^L}}e^{-j\left(\xi^L\right)^3/12}\left[\hat{X}_A^{M_z}(\xi^L)\right]\sqrt{\frac{\rho_1^r\rho_2^r}{(\rho_1^r+s_r)(\rho_2^r+s_r)}}e^{-jk(s_r)} \right\} \tag{3.61}$$

$$E_\parallel(P) = \bar{E}(P)\cdot\hat{e}_\parallel = \frac{-jkZ_0}{4\pi}\left\{ E_\parallel^i(P)+\left(\bar{E}^i(Q_R)\cdot\hat{e}_\parallel^i\right) \right.$$
$$\left. \times -\sqrt{\frac{-4}{\xi^L}}e^{-j\left(\xi^L\right)^3/12}\left[\frac{e^{-j\frac{\pi}{4}}}{2\sqrt{\pi}\xi^L}\left[1-F(X^L)\right]+\hat{X}_F^{M_z}(\xi^L)\right]\sqrt{\frac{\rho_1^r\rho_2^r}{(\rho_1^r+s_r)(\rho_2^r+s_r)}}e^{-jk(s_r)} \right\}, \tag{3.62}$$

where the 3-D Fock-type integral functions are defined as

$$\hat{X}_A^{M_z}(\xi^{L,d}) = \frac{e^{-j\frac{\pi}{4}}}{\sqrt{\pi}}\int_\tau\left(X_A^{M_z}\right)e^{-j\xi^{L,d}\tau}d\tau \tag{3.63}$$

$$\hat{X}_F^{M_z}(\xi^{L,d}) = \frac{e^{-j\frac{\pi}{4}}}{\sqrt{\pi}}\int_\tau\left(X_F^{M_z}\right)e^{-j\xi^{d}\tau}d\tau \tag{3.64}$$

The new integrands for the integrals of Fock-type integral functions are defined as

$$X_A^{J_z} = \frac{\left[X_w(\tau,\Lambda)X_V(\tau,\Lambda^{-1}) - \left(X_C\right)^2 w_2(\tau)V(\tau)\right]}{\left[X_w(\tau,\Lambda)X_w(\tau,\Lambda^{-1}) - \left(X_C w_2(\tau)\right)^2\right]} \tag{3.65a}$$

$$X_F^{J_z} = \left[\frac{jm\cos(\alpha)\sin(\alpha)}{\left[X_w(\tau,\Lambda)X_w(\tau,\Lambda^{-1}) - \left(X_C w_2(\tau)\right)^2\right]}\right] \tag{3.65b}$$

$$X_A^{M_z} = \left[\frac{jm\cos(\alpha)\sin(\alpha)}{\left[X_w(\tau,\Lambda)X_w(\tau,\Lambda^{-1}) - \left(X_C w_2(\tau)\right)^2\right]}\right] \tag{3.65c}$$

$$X_F^{M_z} = \frac{\left[X_w(\tau,\Lambda^{-1})X_V(\tau,\Lambda) - \left(X_C\right)^2 w_2(\tau)V(\tau)\right]}{\left[X_w(\tau,\Lambda)X_w(\tau,\Lambda^{-1}) - \left(X_C w_2(\tau)\right)^2\right]} \tag{3.65d}$$

where

$$X_w(\tau,\Lambda) = \left(w_2'(\tau) + jm\Lambda\cos^2(\alpha)w_2(\tau)\right), \tag{3.66a}$$

$$X_w(\tau,\Lambda^{-1}) = \left(w_2'(\tau) + jm\Lambda^{-1}\cos^2(\alpha)w_2(\tau)\right), \tag{3.66b}$$

$$X_V(\tau,\Lambda) = \left(V'(\tau) + jm\Lambda\cos^2(\alpha)V(\tau)\right), \tag{3.66c}$$

$$X_V(\tau,\Lambda^{-1}) = \left(V'(\tau) + jm\Lambda^{-1}\cos^2(\alpha)V(\tau)\right), \tag{3.66d}$$

$$X_C = m\cos(\alpha)\sin(\alpha). \tag{3.66e}$$

Importantly, the new 3-D impedance Fock-type integral functions reduce to the 2-D impedance Fock-type integral functions [25] and [26] if the $\alpha \to 0$, thus

$$X_A^{J_z} = \frac{V'(\tau) + jm\Lambda^{-1}V(\tau)}{w_2'(\tau) + jm\Lambda^{-1}w_2(\tau)} \tag{3.67a}$$

$$X_F^{J_z} = 0 \tag{3.67b}$$

$$X_A^{M_2} = 0 \tag{3.67c}$$

$$X_F^{M_2} = \frac{V'(\tau) + jm\Lambda V(\tau)}{w_2'(\tau) + jm\Lambda w_2(\tau)}. \tag{3.67d}$$

Moreover, the new 3-D impedance Fock-type integral functions reduce to PEC Fock-type integral functions [18] with $Z_0 \approx 0$ or $\Lambda \approx 0$, and can be written as

$$X_A^{J_2} = \frac{V(\tau)}{w_2(\tau)} \tag{3.68a}$$

$$X_F^{J_2} = \left[T_0 \frac{\Lambda}{[w_2'(\tau) w_2(\tau)]} \right] = 0 \tag{3.68b}$$

$$X_A^{M_2} = \left[T_0 \frac{\Lambda}{[w_2'(\tau) w_2(\tau)]} \right] = 0 \tag{3.68c}$$

$$X_F^{M_2} = \frac{V'(\tau)}{w_2'(\tau)} \tag{3.68d}$$

where $T_0 = \frac{\sin(\alpha)}{\cos(\alpha)} = \frac{\cos(\theta^i)}{\sin(\theta^i)}$ is the torsion factor of ray twist around the surface of the cylinder. The T_0 was introduced in [18].

$$\xi^d = \frac{m(Q) t_d}{a}, \; m(Q) = \left(\frac{k\rho_g}{2} \right)^{1/3}$$

$$X^L = 2kL^L \cos^2(\theta^i), \; X^d = \frac{kL^d (\xi^d)^2}{2m(Q)^2},$$

$$\rho_2^r = s_1, \rho_2^d = s_1 + t_d \text{ and } \rho_1^r = \left[\frac{1}{s_1} + \frac{2\sin^2(\theta_0)}{a\cos(\theta^i)} \right]^{-1}$$

where $L^L = s_1$ and $L^d = s_i$ for the plane wave incidence and $L^L = \frac{s_1 s_r}{s_1 + s_r}$, $L^d = \frac{s_i s_d}{s_i + s_d}$ in the cases of cylindrical and spherical wave incidence, respectively. The s_1 denotes the incident ray path at the reflection point. Some parameters are defined in [18].

3.5 Numerical Results

- **New 3-D Impedance Fock-type Integral Functions** $\hat{X}_A^{J_\nu}(\xi)$

Using the procedure in Appendix C, Equations (3.56) and (3.64) can be computed numerically. For example, let $\Lambda = j0.3$ and $a = 3\lambda$, the example of the numerical results is shown in Fig. 3.5.

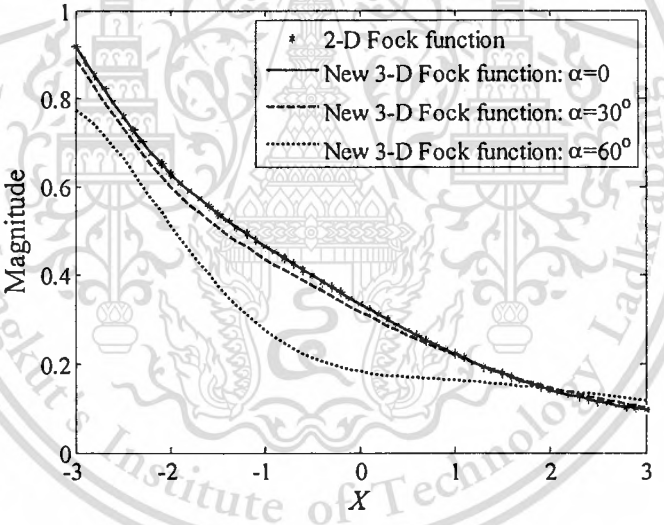

(a) Magnitude of $\hat{X}_A^{J_\nu}(\xi)$ function

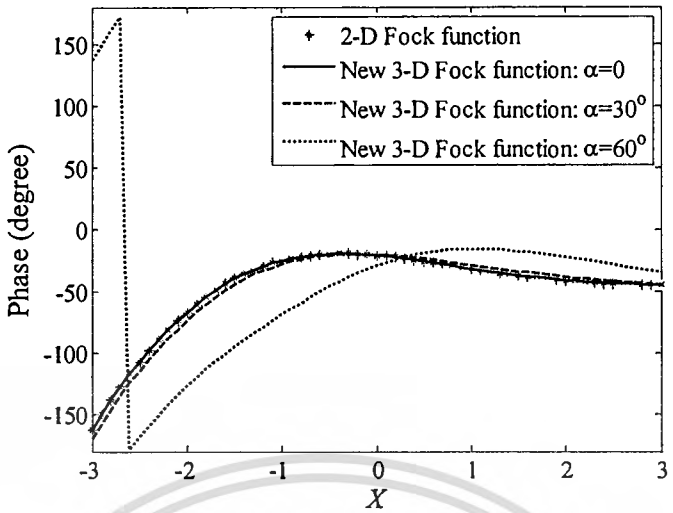

(b) Phase of $\hat{X}_A^{J_z}(\xi)$ function

Figure 3.5 Comparison of the numerical results of $\hat{X}_A^{J_z}(\xi)$ function and classical 2-D impedance Fock-type function where argument $\xi = X$ and plotted without the singular $-1/2X$ factor ($-1/2X$ suppressed).

- **New 3-D Impedance Fock-type Integral Functions $\hat{X}_F^{M_z}(\xi)$**

For example, let $\Lambda = j0.3$ and $a = 3\lambda$, the example of the numerical results is shown in Fig. 3.6.

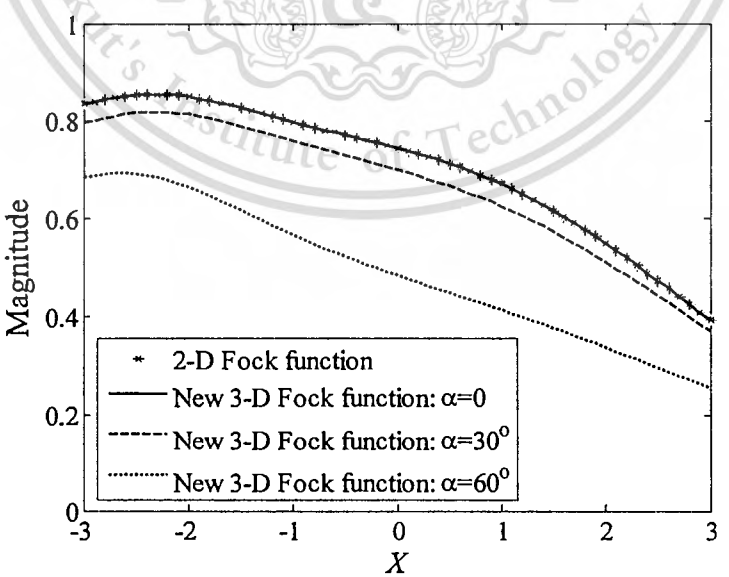

(a) Magnitude of $\hat{X}_F^{M_z}(\xi)$ function

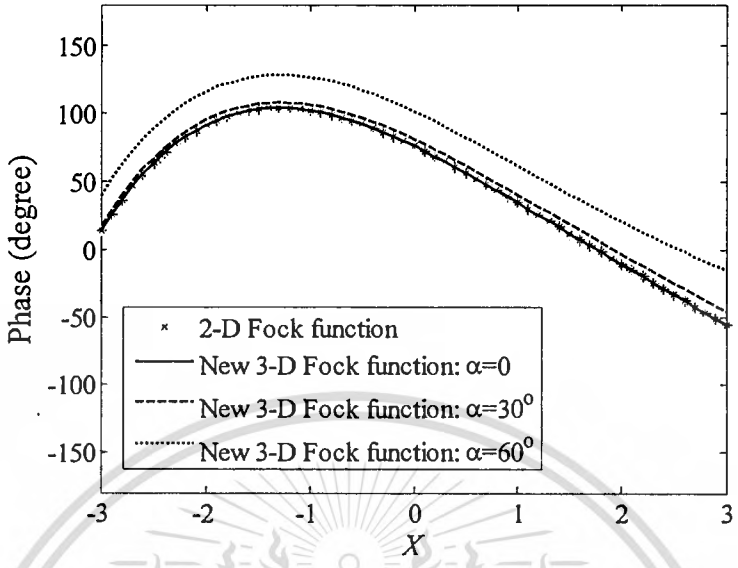

(b) Phase of $\hat{X}_F^{M_z}(\xi)$ function

Figure 3.6 Comparison of the numerical results of $\hat{X}_F^{M_z}(\xi)$ function and classical 2-D impedance Fock-type function where argument $\xi = X$ and plotted without the singular $-1/2X$ factor ($-1/2X$ suppressed).

Figures 3.5 and 3.6 illustrate the effect of the α angle on the $\hat{X}_A^{J_z}(\xi)$ and $\hat{X}_F^{M_z}(\xi)$ functions compared with the classical 2-D impedance Fock-type integral function. The $\hat{X}_A^{J_z}(\xi)$ and $\hat{X}_F^{M_z}(\xi)$ functions are very important in the 3-D case. Meanwhile, the $\hat{X}_F^{J_z}(\xi)$ and $\hat{X}_A^{M_z}(\xi)$ functions are vanished or very small when $\alpha \to 0$.

Figures 3.7 to 3.9 illustrate the total field results in case of J_z source with $\varepsilon_r = 2.1$, 4 and 6, respectively. The case study of $a = 2\lambda$ and $\rho' = 5\lambda$, calculated fields are plotted as a function of ϕ. The comparison results between the proposed 3-D UTD solution and the reference solution (CST) are in good agreement with various thickness *d*.

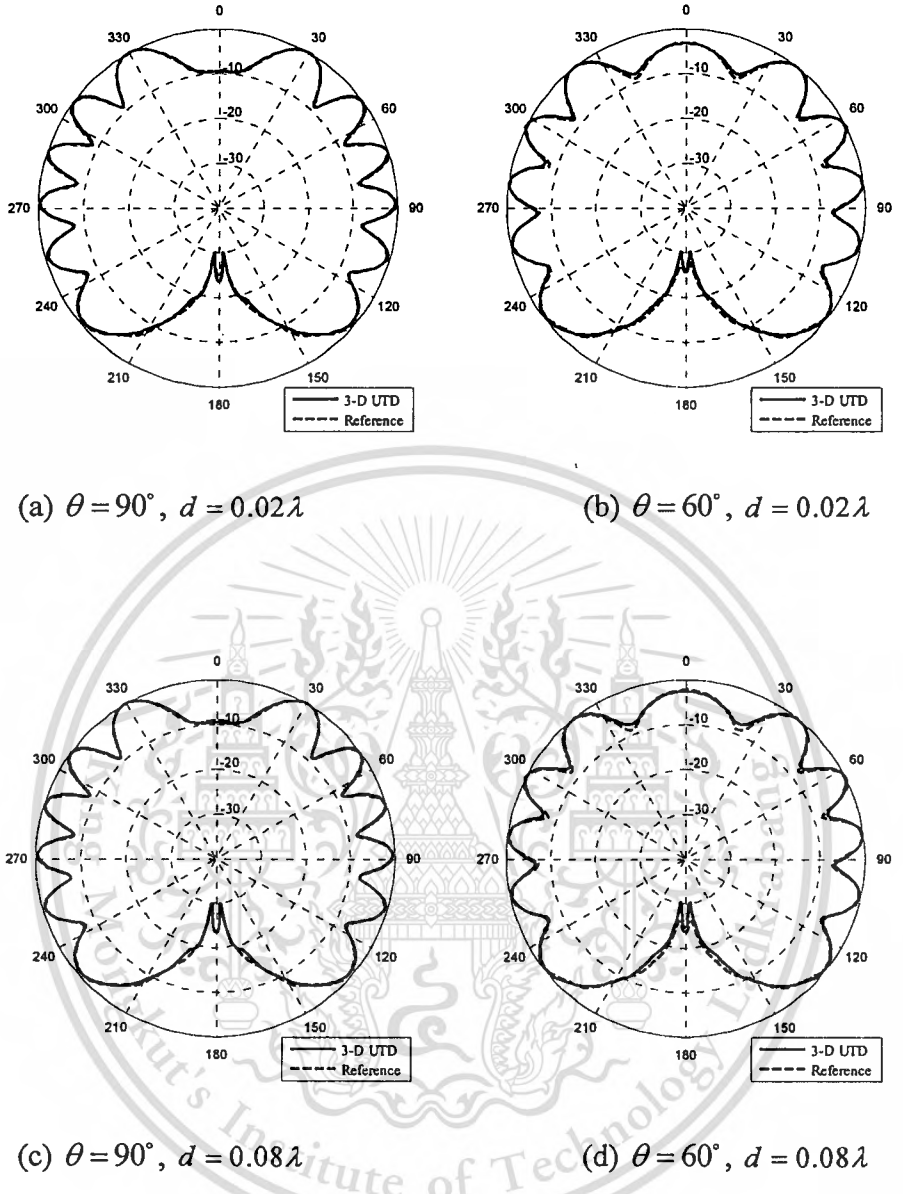

(a) $\theta = 90^\circ$, $d = 0.02\lambda$ (b) $\theta = 60^\circ$, $d = 0.02\lambda$

(c) $\theta = 90^\circ$, $d = 0.08\lambda$ (d) $\theta = 60^\circ$, $d = 0.08\lambda$

Figure 3.7 Comparison of the total field from J_z source: $\varepsilon_r = 2.1$, $a = 2\lambda$ and $\rho' = 5\lambda$. The fields are plotted as a function of ϕ.

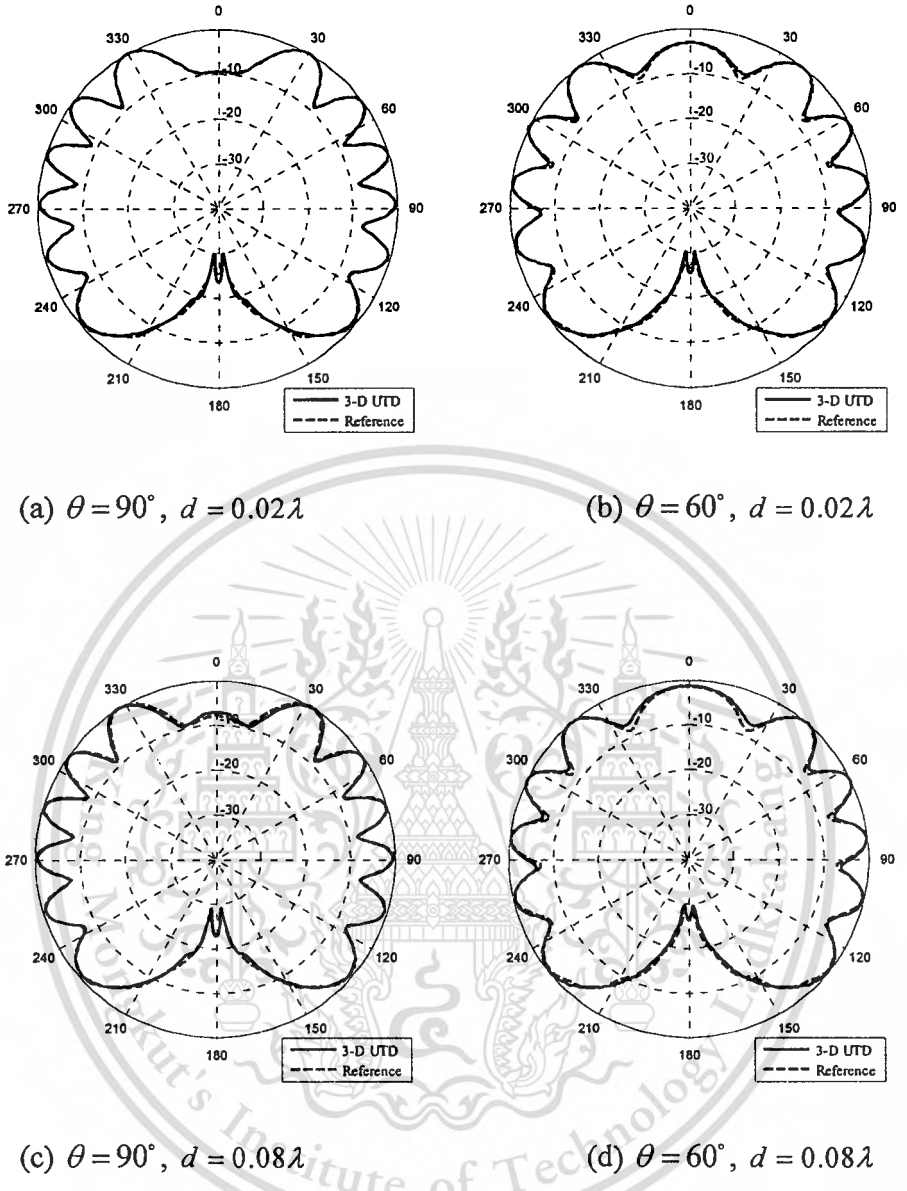

(a) $\theta = 90^\circ$, $d = 0.02\lambda$ (b) $\theta = 60^\circ$, $d = 0.02\lambda$

(c) $\theta = 90^\circ$, $d = 0.08\lambda$ (d) $\theta = 60^\circ$, $d = 0.08\lambda$

Figure 3.8 Comparison of the total field from J_z source: $\varepsilon_r = 4$, $a = 2\lambda$ and $\rho' = 5\lambda$. The fields are plotted as a function of ϕ.

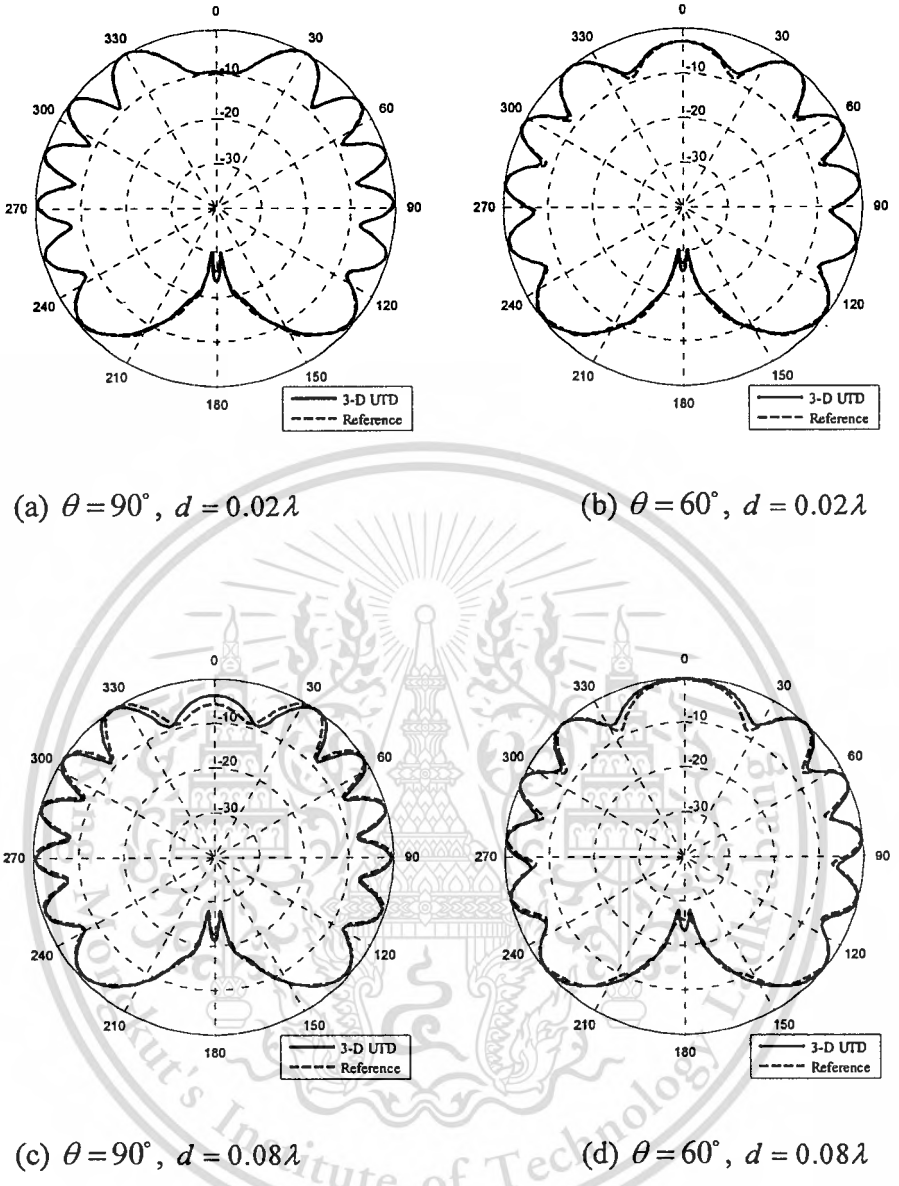

(a) $\theta = 90^\circ$, $d = 0.02\lambda$ (b) $\theta = 60^\circ$, $d = 0.02\lambda$

(c) $\theta = 90^\circ$, $d = 0.08\lambda$ (d) $\theta = 60^\circ$, $d = 0.08\lambda$

Figure 3.9 Comparison of the total field from J_z source: $\varepsilon_r = 6$, $a = 2\lambda$ and $\rho' = 5\lambda$. The fields are plotted as a function of ϕ.

The computational time is shown in Table 2. For example, 360 field points around the cylinder are calculated by using the proposed 3-D UTD solution. The computational time of the proposed 3-D UTD solution is less than the CST Microwave Studio program.

Table 2. Computational time of the 3-D UTD solution.

CPU Intel Core i7, 3.1 GHz with 24 GB of RAM		
Case: a=2λ , $\rho' = 5\lambda$, $\theta = 60^\circ$, and d=0.08λ	CST Microwave Studio (FIT method) (360 field points)	Proposed 3-D UTD solution (360 field points and ray tracing procedure is included)
$\varepsilon_r = 2.1$ (Teflon)	21 minutes, 46 seconds	102 seconds
$\varepsilon_r = 6$	5 hours, 33 minutes	121 seconds

3.6 Summary

In this chapter, the achieved analytical solutions for the EM wave scattered from an impedance cylinder are as follows.

- The three dimensional (3-D) exact solutions are based on Green's functions for the EM wave scattered from an impedance cylinder with axial electric J_z and magnetic M_z current sources.
- The asymptotic solution (rays solution) for the EM wave scattered from an impedance cylinder. The complexity of the 3-D exact solution is reduced by using the asymptotic approximation.
- The 3-D UTD solution for the EM wave scattered from an impedance cylinder is achieved.

The asymptotic solutions are converted into the classical UTD format by using the ray transformation. The achieved new 3-D impedance Fock-type integral functions recover the 2-D impedance Fock-type integral functions in cases of normal incident $\alpha \to 0$, and recover the PEC Fock-type integral functions when the surface impedance $Z_s \to 0$ (i.e. $\Lambda = 0$). It is found that the 3-D Fock-type integral functions of $X_F^{J_s} = 0$ and $X_F^{J_s} = 0$ for the 2-D impedance curved surface case. It is clearly evident that the coupling fields vanish for the normal incident (i.e. 2-D case) case and without coupling field terms for the PEC surface case.

CHAPTER 4

MODIFIED UTD SOLUTION FOR THE CONVEX IMPEDANCE CYLINDER SURFACE AND ITS ACCURACY OF THE SOLUTION

4.1 Introduction

The modified UTD solution for impedance cylinder was proposed in [28]. The solution is obtained by modifying the classical three dimensional (3-D) UTD solution for PEC surface cylinder [18]. Under the assumption of low transmitting and receiving antenna heights, the impedance Fock-type integral functions of the two dimensional (2-D) case are used instead of the PEC Fock-type integral functions of the classical UTD solution. The modified 3-D UTD solution can be accurately used to calculate the electromagnetic (EM) fields comparing with the results from the CST Microwave Studio program (based on finite integral technique (FIT)). It is observed that in chapter 3, the new 3-D Fock-type integral functions in the proposed 3-D UTD solution (based on Green's functions) reduce to the 2-D impedance Fock-type integral function in case of $\alpha = 0$. The complexity of the proposed 3-D UTD solution can be reduced by using the modified 3-D UTD.

This chapter explains the idea how to develop the modified 3-D UTD solution for the EM wave scattered from an impedance cylinder. Also, the accuracy and its limitation of the modified 3-D UTD scattering solution for impedance cylinder will be illustrated.

4.2 Summary of the Classical 3-D UTD Solution for EM Wave Scattered from a Perfect Electric Conductor (PEC) Cylinder

The classical 3-D UTD solution was presented in [18]. The solution was proposed for general curved PEC surface. In this section, we will focus on the canonical cylinder shape. The UTD solution in lit zone (line-of-sight region) and the shadow zone will be summarized in this section.

Figure 4.1 The problem geometry: (a) Cylinder problem and (b) Actual problem and equivalent problem of the UTD method (Top view)

Figure 4.1 shows a canonical UTD cylinder problem where a radius of the cylindrical geometry is defined as a, and the source (ρ',ϕ',z') and observation position at (ρ,ϕ,z) are not located close to the cylinder surface. The total field (TE^z or TM^z) at the observation point P includes the direct illumination from the incident geometrical optics ray field $u_i(P)$ which can be a plane wave, cylindrical or spherical wave, plus the reflected wave field $u_r(P)$ in the lit region. Only the diffracted field $u_d(P)$ remains in the shadow region. The field at the observation point P in the lit region (i.e. line-of-sight) can be written in the form

$$\bar{u}_t(P)=\bar{u}_i(P)+\bar{u}_i(Q_R)\cdot\bar{\bar{R}}_{s,h}A_{llt}e^{-jks_r}. \tag{4.1}$$

$u_i(P)$ and $u_i(Q_R)$ denote the incident field at the observation point and the reflected field at the reflection point (Q_R), respectively. The A_{llt} denotes the reflected ray spreading factor which must depend on the incident wave types and surface geometry. The $\bar{\bar{R}}$ denotes the generalized reflection coefficients of the curved surface which is related to the acoustic soft (R_s) and hard (R_h) functions. The R_s and R_h functions are written as

$$R_{s,h}=-\sqrt{\frac{-4}{\xi^L}}e^{-j\frac{(\xi^L)^3}{12}}\left\{\frac{e^{-j\pi/4}}{2\xi^L\sqrt{\pi}}\left(1-F(kL\tilde{a})\right)+\hat{P}_{s,h}(\xi^L)\right\}, \tag{4.2}$$

where

$$\bar{\bar{R}}=R_s\hat{e}_\perp^i\hat{e}_\perp^r+R_h\hat{e}_\parallel^i\hat{e}_\parallel^r \tag{4.3}$$

and

$$\hat{P}_{s,h}(\xi^L)=\frac{e^{-j(\pi/4)}}{\sqrt{\pi}}\int_{-\infty}^{\infty}\frac{\tilde{Q}V(\tau)}{\tilde{Q}w_2(\tau)}e^{-j\xi^L\tau}d\tau. \tag{4.4}$$

The subscript s and h refer to soft and hard polarization of the incident fields. $\tilde{Q}=1$ for the soft case and $\tilde{Q}=\frac{\partial}{\partial\tau}$ for hard case, respectively. The generalized reflection coefficients $R_{s,h}$ consists of the Fresnel's type function $F(kL\tilde{a})$ and the Pekeris-integral function $\hat{P}_{s,h}(\xi^L)$ or called Fock-type integrals function. In the case of the PEC cylinder surface, the function $F(kL\tilde{a})$ and $\hat{P}_{s,h}(\xi^L)$ are simply computed by using the large and small argument approximations and also via tabulated values for intermediate range of the arguments. But this scheme is not valid for an impedance surface case. Thus, it is necessary to use a numerical integration procedure to evaluate the Pekeris-integral functions $\hat{P}_{s,h}(\xi^L, q_{s,h})$ for the impedance case. The computation of this integral is explained later in the next section.

When the observation point moves to the shadow zone, only the diffracted field $\bar{u}_d(P)$ is remained. The diffracted field launches from the surface of the canonical cylinder at point Q_1 to subsequently reach the observation point P. The $\bar{u}_d(P)$ in [18] can be written in the form

$$\bar{u}_d(P)=\bar{u}_i(Q_1)\cdot\bar{\bar{T}}A_{ilit}e^{-jks_d} \tag{4.5}$$

The $\bar{u}_i(Q_1)$ denotes the incident field at the initial diffraction point Q_1. The generalized diffraction coefficient ($\bar{\bar{T}}$) in [18] can be written in the form

$$T_{s,h}=-\sqrt{m(Q_1)m(Q_2)}\sqrt{\frac{2}{k}}e^{-jkt}\left\{\frac{e^{-j\pi/4}}{2\xi^d\sqrt{\pi}}\left(1-F(kL\tilde{a})\right)+\hat{P}_{s,h}(\xi^d)\right\}, \tag{4.6}$$

where

$$\bar{\bar{T}}=T_s\hat{b}_1^i\hat{b}_2^d+T_h\hat{n}_1^i\hat{n}_2^d. \tag{4.7}$$

Fock-type integral function in shadow zone can be written as

$$\hat{P}_{s,h}(\xi^d) = \frac{e^{-j(\pi/4)}}{\sqrt{\pi}} \int_{-\infty}^{\infty} \frac{\tilde{Q}V(\tau)}{\tilde{Q}w_2(\tau)} e^{-j\xi^d \tau} d\tau \,, \tag{4.8}$$

and A_{shadow} denotes the diffracted ray spreading factor which depends on the surface geometry. The parameters in those equations are as follows

$$\xi^d = \frac{m(Q)\cdot t}{a},\ m(Q) = \left(\frac{k\rho_g}{2}\right)^{1/3},\ X^L = 2kL^L\cos^2(\theta^i),\ X^d = \frac{kL^d(\xi^d)^2}{2m(Q)^2},$$

$$A_{lit} = \sqrt{\frac{\rho_1^r\rho_2^r}{(\rho_1^r+s_r)(\rho_2^r+s_r)}},\ A_{shadow} = \sqrt{\frac{s_i}{s_i+t_d}}\cdot\sqrt{\frac{\rho_2^d}{s^d(\rho_2^d+s^d)}}$$

$$\rho_2^r = s_1,\ \rho_2^d = s_i + t_d,\ \rho_1^r = \left[\frac{1}{s_1} + \frac{2\sin^2(\theta_0)}{a\cos(\theta^i)}\right]^{-1},$$

where $L^L = s_1$ and $L^d = s_i$ for the plane wave incidence and $L^L = \frac{s_1 s_r}{s_1+s_r}$, $L^d = \frac{s_i s_d}{s_i+s_d}$ in the cases of cylindrical and spherical wave incidence, respectively. The s_1 denotes the incident ray path at the reflection point. Some parameters are defined in [18].

4.3 The Modified 3-D UTD Solution for a Convex Impedance Cylinder

The 2-D UTD solution for a 2-D convex impedance surface was presented in [25] and [26]. The 2-D UTD solution for a convex impedance surface requires the Pekeris-integral functions $\hat{P}_{s,h}(\xi^{L,d}, q_{s,h})$ (Fock-type integral function). The $\hat{P}_{s,h}(\xi^{L,d}, q_{s,h})$ function consists of the Fock-type Airy functions. The $\hat{P}_{s,h}(\xi^{L,d}, q_{s,h})$ functions depend on the boundary condition at the surface.

This section presents a heuristic UTD solution for computing the EM field scattered from an impedance convex surface. The presented UTD solution for 3-D impedance convex surface is obtained by removing the PEC Fock-type integral function and replacing with the impedance 2-D Fock-type integral function. For the PEC curved

surface case, the Pekeris-integral function $P_{s,h}(\xi^L)$ is generally evaluated via the large and small argument approximation and via the numerically tabulated values for the intermediate ranges of the argument of the function [25]-[26]. These latter schemes are not possible for an impedance convex surface case because the Pekeris function cannot be tabulated as a function of only one universal parameter. Hence, one applies a numerical integration procedure to compute the UTD Pekeris-integral transition function for an impedance convex surface. The impedance Fock-type integral function $\hat{P}_{s,h}(\xi^{L,d}, q_{s,h})$ is defined as

$$\hat{P}_{s,h}(\xi^{L,d}, q_{s,h}) = \frac{e^{-j(\pi/4)}}{\sqrt{\pi}} \int_{-\infty}^{\infty} \frac{V'(\tau) - q_{s,h} V(\tau)}{w_2'(\tau) - q_{s,h} w_2'(\tau)} e^{-j\xi^{L,d}\tau} d\tau \tag{4.9}$$

and

$$q_{s,h} = \begin{cases} -j\left(\dfrac{ka}{2\sin^2(\theta_0)}\right)^{\frac{1}{3}} \Lambda^{-1} & \text{soft case} \\ -j\left(\dfrac{ka}{2\sin^2(\theta_0)}\right)^{\frac{1}{3}} \Lambda & \text{hard case} \end{cases} \tag{4.10}$$

As mentioned above, the proposed solution includes the $\hat{P}_{s,h}(\xi^{L,d}, q_{s,h})$ transition function for the impedance boundary condition. It is necessary to use a numerical integration procedure for evaluating the $\hat{P}_{s,h}(\xi^{L,d}, q_{s,h})$ for the UTD solution. The computation of the $\hat{P}_{s,h}(\xi^{L,d}, q_{s,h})$ is shown below.

In Appendix C, the integration in Equation (4.9) cannot be evaluated analytically. The $\hat{P}_{s,h}(\xi^{L,d}, q_{s,h})$ can be finally written as

$$\hat{P}_{s,h}(X, q_{s,h}) = \frac{e^{-j(\pi/4)}}{\sqrt{\pi}} \left\{ -\frac{1}{2X} + G_1(X,t) + G_2(X,t) \right\}, \tag{4.11}$$

where

$$G_1(X,q_{s,h}) = \frac{e^{-j(\pi/6)}}{2} \cdot \int_0^{\infty} \frac{\left[e^{-j(\pi/6)}Ai'(t)+q_{s,h}e^{j(\pi/6)}Ai(t)\right]e^{-jXrt}}{e^{j(\pi/6)}Ai'(te^{j(2\pi/3)})+q_{s,h}e^{-j(\pi/6)}Ai(te^{j(2\pi/3)})}dt \quad (4.12)$$

and

$$G_2(X,q_{s,h}) = -\frac{1}{2} \cdot \int_0^{\infty} \frac{\left[Ai'(t)-q_{s,h}Ai(t)\right]e^{-jXt}}{e^{j(\pi/6)}Ai'(te^{-j(2\pi/3)})+q_{s,h}e^{-j(\pi/6)}Ai(te^{-j(2\pi/3)})}dt . \quad (4.13)$$

The integration scheme employed in the literature [36] is based on the Fourier quadrature method. In this thesis, a numerical integration method based on the recursive adaptive Simpson quadrature to compute this Fock-type integration function is employed. The present method is very efficient and requires less computational time. The upper limit of the integral in Equation (4.9) is infinity. However, in this work, the upper limit of the integral in Equation (4.9) is assumed to be only 100 to achieve accurate results because it is shown that it is large enough to satisfy the required accuracy. To verify the accuracy of the Pekeris or Fock-Type integral function, a comparison of results between the modified 3-D UTD solution via the numerical integration scheme and the results from CST Microwave Studio program are presented in the next section.

4.4 Special Case of the New 3-D Impedance Fock-type Integral Functions

From mentioned in section 4.3, the modified 3-D UTD solution is obtained by heuristically modifying the classical PEC Fock-type integral function. In chapter 3, four new impedance Fock-type integral functions are written as

$$\hat{X}_{A,F}^{J_z,M_z}(\xi^{L,d}) = \frac{e^{-j\frac{\pi}{4}}}{\sqrt{\pi}} \int_{\tau} \left(X_{A,F}^{J_z,M_z}\right) e^{-j\xi^{L,d}\tau} d\tau . \quad (4.14)$$

From the previous chapter, the integrands of the Fock-type integrals functions are defined as

$$X_A^{J_z} = \frac{\left[X_w(\tau,\Lambda)X_V(\tau,\Lambda^{-1}) - \left(X_C\right)^2 w_2(\tau)V(\tau)\right]}{\left[X_w(\tau,\Lambda)X_w(\tau,\Lambda^{-1}) - \left(X_C w_2(\tau)\right)^2\right]} \tag{4.15a}$$

$$X_F^{J_z} = \left[\frac{jm\cos(\alpha)\sin(\alpha)}{\left[X_w(\tau,\Lambda)X_w(\tau,\Lambda^{-1}) - \left(X_C w_2(\tau)\right)^2\right]}\right] \tag{4.15b}$$

$$X_A^{M_z} = \left[\frac{jm\cos(\alpha)\sin(\alpha)}{\left[X_w(\tau,\Lambda)X_w(\tau,\Lambda^{-1}) - \left(X_C w_2(\tau)\right)^2\right]}\right] \tag{4.15c}$$

$$X_F^{M_z} = \frac{\left[X_w(\tau,\Lambda^{-1})X_V(\tau,\Lambda) - \left(X_C\right)^2 w_2(\tau)V(\tau)\right]}{\left[X_w(\tau,\Lambda)X_w(\tau,\Lambda^{-1}) - \left(X_C w_2(\tau)\right)^2\right]} \tag{4.15d}$$

where

$$X_w(\tau,\Lambda) = \left(w_2'(\tau) + jm\Lambda\cos^2(\alpha)w_2(\tau)\right) \tag{4.16a}$$

$$X_w(\tau,\Lambda^{-1}) = \left(w_2'(\tau) + jm\Lambda^{-1}\cos^2(\alpha)w_2(\tau)\right) \tag{4. 16b}$$

$$X_V(\tau,\Lambda) = \left(V'(\tau) + jm\Lambda\cos^2(\alpha)V(\tau)\right) \tag{4. 16c}$$

$$X_V(\tau,\Lambda^{-1}) = \left(V'(\tau) + jm\Lambda^{-1}\cos^2(\alpha)V(\tau)\right) \tag{4. 16d}$$

and

$$X_C = m\cos(\alpha)\sin(\alpha)\,. \tag{4. 16e}$$

$V(\tau)$, $V'(\tau)$, $w_2(\tau)$ and $w_2'(\tau)$ denote the Fock type Airy functions and their derivatives. The new 3-D impedance Fock-type integral functions reduce to the 2-D impedance Fock-type integral function [25] in case of $\alpha \to 0$. Thus, the new 2-D impedance Fock-type integral functions can be written as

$$X_A^{J_z} = \frac{V'(\tau) + jm\Lambda^{-1}V(\tau)}{w_2'(\tau) + jm\Lambda^{-1}w_2(\tau)}, \tag{4.17a}$$

$$X_F^{J_z} = 0, \tag{4.17b}$$

$$X_A^{M_z} = 0, \tag{4.17c}$$

and

$$X_F^{M_z} = \frac{V'(\tau) + jm\Lambda V(\tau)}{w_2'(\tau) + jm\Lambda w_2(\tau)}. \tag{4.17d}$$

Moreover, the proposed new 3-D impedance Fock-type integral functions reduce to PEC Fock-type integral function [17]-[18] with $Z_0 \approx 0$ or $\Lambda \approx 0$, and can be written as

$$X_A^{J_z} = \frac{V(\tau)}{w_2(\tau)}, \tag{4.18a}$$

$$X_F^{J_z} = 0 \tag{4.18b}$$

$$X_A^{M_z} = 0 \tag{4.18c}$$

and

$$X_F^{M_z} = \frac{V'(\tau)}{w_2'(\tau)}. \tag{4.18d}$$

Finally, it can confirm that the modified 3-D UTD solution is corrected. The modified 3-D UTD solution will be useful to calculate the EM wave scattered from an impedance cylinder under the condition of small transmitting and receiving antenna heights.

4.5 The Accuracy and the Limitation of the Proposed Modified 3-D UTD Solution

To verify the accuracy of the Fock-Type integral function which is computed by the numerical integration scheme, the CST-Microwave Studio program is also employed as an additional comparison. The CST program is a well-known commercial EM simulation tool based on the finite integral technique (FIT). In practice, the surface impedance Z_s depends on the specific problems. For example, in the single material coated PEC cylinder case, the surface impedance Z_s depends on the thickness (d), permittivity and permeability (ε_r, μ_r) of the materials. The numerical results for the case of a PEC cylinder with a thin dielectric single layer coating are presented. The relation between the surface parameters (i.e. dielectric constant (ε_r, μ_r) and the thickness (d)) and the surface impedance Z_s can be approximated by using the impedance boundary condition (IBC) as shown in [41], namely

$$Z_s \approx -\frac{jZkd}{\varepsilon_r}(1-\varepsilon_r\mu_r)\left[1+\frac{k^2d^2}{2}(1-\varepsilon_r\mu_r)\right]^{-1}. \tag{4.19}$$

Actually, the thickness of a thin material-coated should be small compared to radius of the cylinder $d << a$. In this thesis, the study of the thickness of thinly material-coated PEC cylinder will be performed to find the limitation of the proposed modified 3-D UTD solution and its impedance closed-form. The contour plot of the MSE of the total field between the UTD numerical results and the reference results from CST-Microwave Studio versus the thickness/radius ratio (d/a) and oblique incident angle are employed to find out the limitation of d.

$$MSE = \frac{1}{N}\sum_{i=1}^{N}(y_i-\hat{y}_i)^2 = \frac{1}{N}\sum_{i=1}^{N}(e_i)^2 \tag{4.20}$$

and

$$MSE(dB) = 10\log(MSE) \tag{4.21}$$

The MSE is known as the sum of squared error of each point divided by the total data number of considered data set N. The y_i denotes the reference data from CST-Microwave Studio at point i. The $\hat{y}_i$ denotes the data from the modified 3-D UTD solution at point i (in linear scale). The $y_i - \hat{y}_i = e_i$ denotes the error of each point. Note that the sampling field at point i in this thesis is the total field of any ϕ angles.

The comparison results between the modified 3-D UTD solution and the reference solution based on finite integration technique (FIT) method (CST Microwave Studio program) are illustrated. The parameter θ denotes the angle that is measured from the z-axis or the axis of the cylinder to the observation vector P. This thesis focuses on a general nonmagnetic material. The $\mu_r = 1$, $\varepsilon_r = 2.1$, 4 and 6 are chosen to study the effect of the thickness d on the accuracy of the modified 3-D UTD solution. However, the modified 3-D UTD solution can be used for the magnetic material case.

Figure 4.2 shows the compared MSE contour plots between the UTD numerical results and reference results (CST) of the total field from J_z (s-polarized) source versus the thickness/radius ratio (d/a) and θ angle (oblique angle). Also, the modified 3-D UTD solution is valid for M_z (h-polarized) case. Source distance is located from axis of cylinder of $\rho' = 5\lambda$. The observation point is moved around the cylinder by changing ϕ angle. The MSE contour plots in Fig. 3(a) for $\varepsilon_r = 2.1$ with d/a from 0.01-0.13, (b) for $\varepsilon_r = 4$ with d/a from 0.01-0.09 and (c) for $\varepsilon_r = 6$ with d/a from 0.01- 0.05 are lower than -10 dB of all the coated thickness and θ angles of interest. The MSE(dB) increases when the coated thickness and ε_r increase due to the limitation of approximate closed form of the surface impedance. Moreover, the MSE (dB) increases when the oblique angle θ decreases due to the limitation of the 2-D impedance Fock-type integral function. However, to find the limitation of the proposed modified 3-D UTD solution, the MSE contour line of -20 dB limit is employed. If the MSE is below -20 dB or in the region of MSE lower than -20 dB, the good accuracy can be obtained. For outside the region of MSE lower than -20 dB, the modified 3-D UTD becomes low accurate.

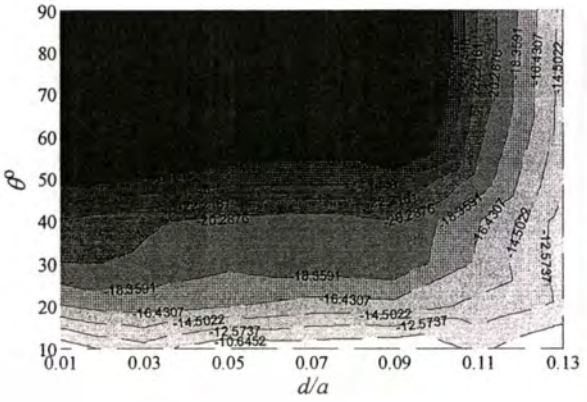

(a) $\varepsilon_r = 2.1$

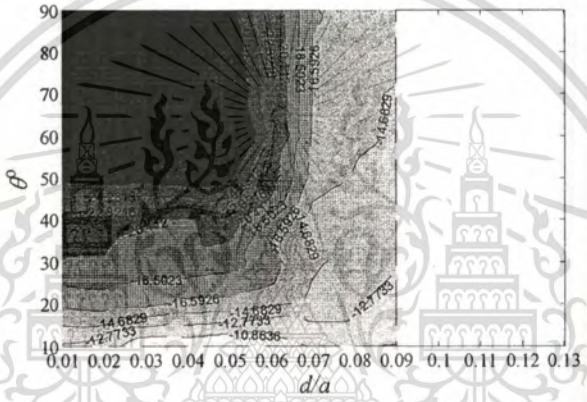

(b) $\varepsilon_r = 4$

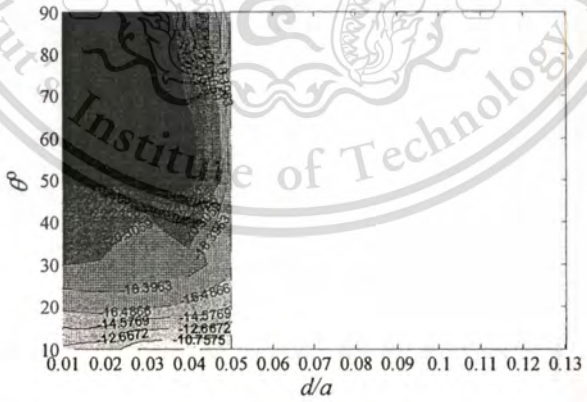

(c) $\varepsilon_r = 6$

Figure 4.2 MSE(dB) contour plots of the total field between modified UTD and CST Microwave Studio around the cylinder versus the thickness/radius ratio: $\varepsilon_r = 2.1$,4, 6, $a = 2\lambda$ and $\rho' = 5\lambda$.

The total field comparison between the modified 3-D UTD and reference are shown in Figs. 4.3 to 4.8. Figs. 4.3, 4.5 and 4.7 show the total field in case of $d/a = 0.01$ or $d = 0.02\lambda$ (lowest bound of interested) with different ε_r. For $\varepsilon_r = 2.1$, the MSE(dB) equals -35.1 dB and -32.5 dB for $\theta = 90^\circ$ (normal incident) and $\theta = 60^\circ$ (oblique incident), respectively as shown in Fig. 4.3. For $\varepsilon_r = 4$, the MSE equals to -37.2 dB and -33.1 dB for $\theta = 90^\circ$ and $\theta = 60^\circ$, respectively as shown in Fig. 4.5. For $\varepsilon_r = 6$, the MSE equals -37.1 dB and -33.1 dB for $\theta = 90^\circ$ and $\theta = 60^\circ$, respectively as shown in Fig. 4.7. All comparison results from Figs. 4.3, 4.5 and 4.7 show very good agreement. In contrast, Figs. 4.4, 4.6 and 4.8 show the total field in case of the approximate closed-form impedance surface Z_s is not valid because the MSE is higher than -20 dB limit. Therefore, the results are not accurate compared with the reference results from CST program. In Fig. 4.4 for $\varepsilon_r = 2.1$, the MSE equals -14.0 dB and -13.7 dB for (a) $\theta = 90^\circ$ and (b) $\theta = 60^\circ$, respectively. In Fig. 4.6 for $\varepsilon_r = 4$, the MSE equals -16.7 dB and -16.4 dB for (a) $\theta = 90^\circ$ and (b) $\theta = 60^\circ$, respectively. In Fig. 4.8 for $\varepsilon_r = 6$, the MSE equals -16.9 dB and -17.8 dB for (a) $\theta = 90^\circ$ and (b) $\theta = 60^\circ$, respectively.

According to the modified 3-D UTD solution, the 2-D impedance Fock-type integral function of the TE^z and TM^z wave normal incident ($\alpha = 0$) is used, these solutions do not valid in case of low θ angle. The limitation of the modified 3-D UTD solutions as a function of θ angle is also shown in Fig. 4.2 (a), (b) and (c) for $\varepsilon_r = 2.1$, 4 and 6, respectively. For the θ angles around 40 to 90 degrees, all of the considered ε_r, the MSEs are lower than -20 dB. However, the MSEs are also depended on the material-coated thickness/radius ratio. The area of the MSE lower than -20 dB in Fig. 4.2 decreases when the ε_r increases. From the studies, the θ angle must be greater than 40 degrees. The thickness/radius ratio of dielectric-coated PEC cylinder in case of $\varepsilon_r = 2.1$ should be $d/a \le 0.11$. For other cases, there should be $d/a \le 0.07$ for $\varepsilon_r = 4$ and it should be $d/a \le 0.05$ for $\varepsilon_r = 6$. Thus, the ε_r affects the maximum value of the coated thickness. The MSEs contour plots in Fig. 4.2 can be used as the guideline for using the

proposed modified 3-D UTD solution accurately. Note that the accuracy of the CST results depend strongly on the mesh-cell density. At least 40 million mesh-cells are employed in the simulation of this thesis to guarantee the accurate result. It is found that the minimum computational time of the commercial software is around 2 hours and the maximum is around 9 hours for CPU Intel Core i7, CPU-speed 3.1 GHz with 24 GB RAM. The periodic boundary condition is employed to model the infinite cylinder. The mesh-cell density may sometimes be up to 80 million mesh-cells. However, the modified 3-D UTD computational time is less than 2 minutes (the ray tracing procedure is included) on the same machine configuration and it does not depend on the source and observation distance. However, for the commercial software, the computational time depends on the source, observation distance and provides no physical insight to the result.

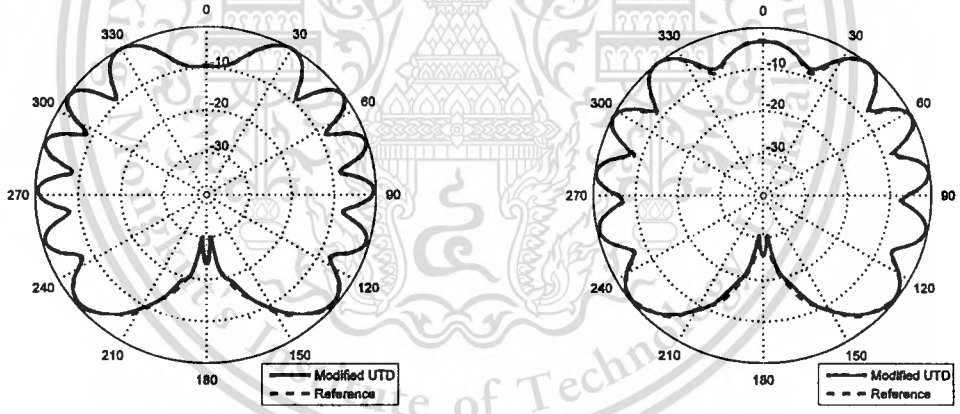

(a) $\theta = 90^\circ$ (b) $\theta = 60^\circ$

Figure 4.3 Comparison of the total field from J_z source: $\varepsilon_r = 2.1$, $a = 2\lambda$, $\rho' = 5\lambda$, and $d/a = 0.01$ or $d = 0.02\lambda$. (a) $\theta = 90^\circ$, MSE=-35.1 dB and (b) $\theta = 60^\circ$, MSE=-32.5 dB. The fields are plotted as a function of ϕ.

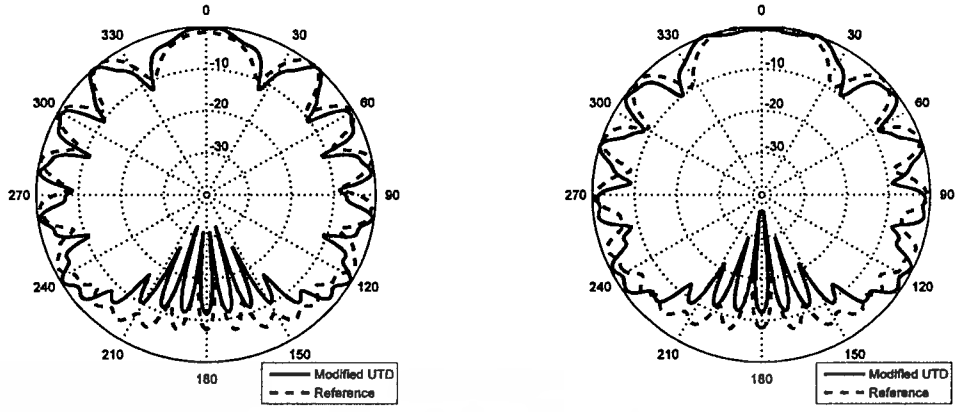

(a) $\theta = 90^\circ$ (b) $\theta = 60^\circ$

Figure 4.4 Comparison of the total field in case of the approximate closed-form impedance surface Z_s is not valid: $\varepsilon_r = 2.1$, $a = 2\lambda$, $\rho' = 5\lambda$, and $d/a = 0.03$ or $d = 0.26\lambda$. (a) $\theta = 90^\circ$, MSE=-14.0dB and (b) $\theta = 60^\circ$, MSE=-13.7B. The fields are plotted as a function of ϕ.

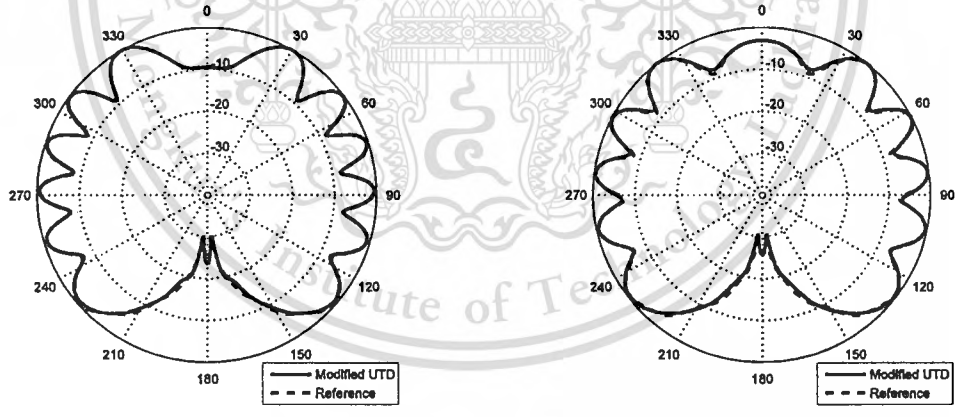

(a) $\theta = 90^\circ$ (b) $\theta = 60^\circ$

Figure 4.5 Comparison of the total field from J_z source: $\varepsilon_r = 4$, $a = 2\lambda$, $\rho' = 5\lambda$, and $d/a = 0.01$ or $d = 0.02\lambda$. (a) $\theta = 90^\circ$, MSE=-37.2 dB and (b) $\theta = 60^\circ$, MSE=-33.1 dB. The fields are plotted as a function of ϕ.

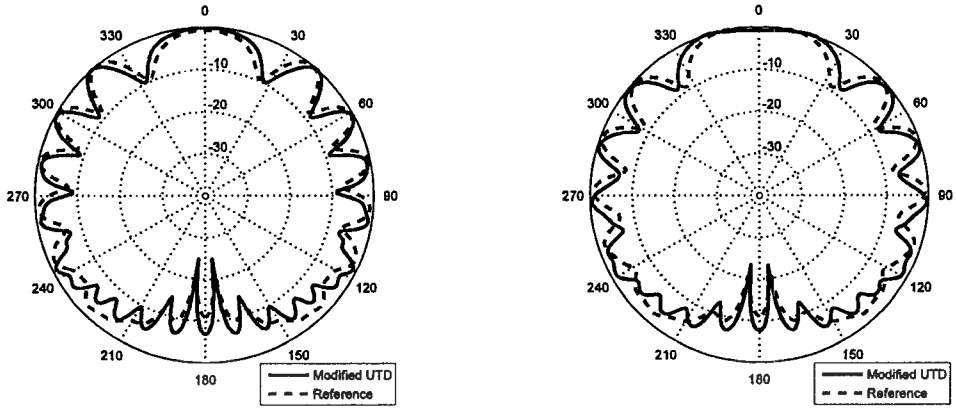

(a) $\theta = 90^\circ$ (b) $\theta = 60^\circ$

Figure 4.6 Comparison of the total field in case of the approximate closed-form impedance surface Z_s is not valid: $\varepsilon_r = 4$, $a = 2\lambda$, $\rho' = 5\lambda$, and $d/a = 0.07$ or $d = 0.14\lambda$. (a) $\theta = 90^\circ$, MSE=-16.7dB and (b) $\theta = 60^\circ$, MSE=-16.4dB. The fields are plotted as a function of ϕ.

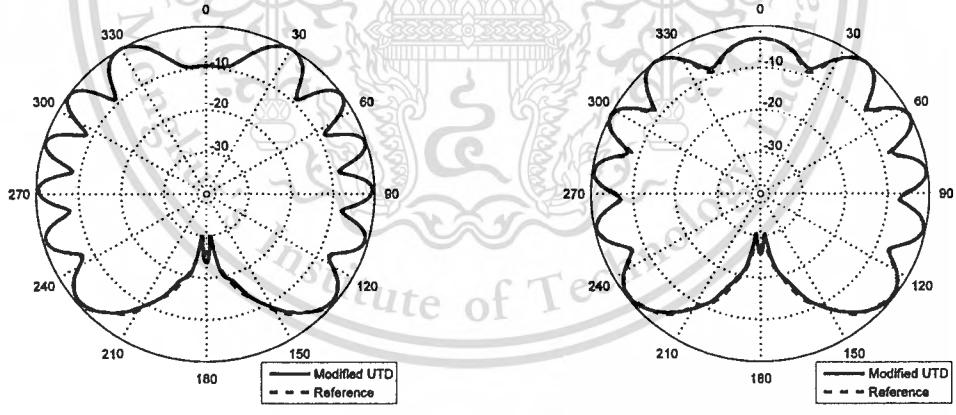

(a) $\theta = 90^\circ$ (b) $\theta = 60^\circ$

Figure 4.7 Comparison of the total field from J_z source: $\varepsilon_r = 6$, $a = 2\lambda$, $\rho' = 5\lambda$, and $d/a = 0.01$ or $d = 0.02\lambda$. (a) $\theta = 90^\circ$, MSE=-37.1 dB and (b) $\theta = 60^\circ$, MSE=-33.1 dB. The fields are plotted as a function of ϕ.

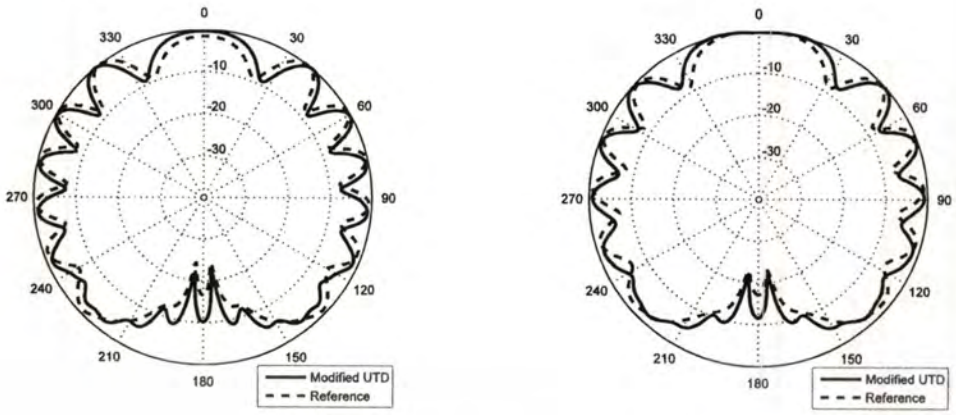

(a) $\theta = 90^{\circ}$ (b) $\theta = 60^{\circ}$

Figure 4.8 Comparison of the total field in case of the approximate closed-form impedance surface Z_s is not valid: $\varepsilon_r = 6$, $a = 2\lambda$, $\rho' = 5\lambda$, and $d/a = 0.05$ or $d = 0.1\lambda$. (a) $\theta = 90^{\circ}$, MSE=-16.9dB and (b) $\theta = 60^{\circ}$, MSE=-17.8dB. The fields are plotted as a function of ϕ.

4.6 Numerical and Measured Results

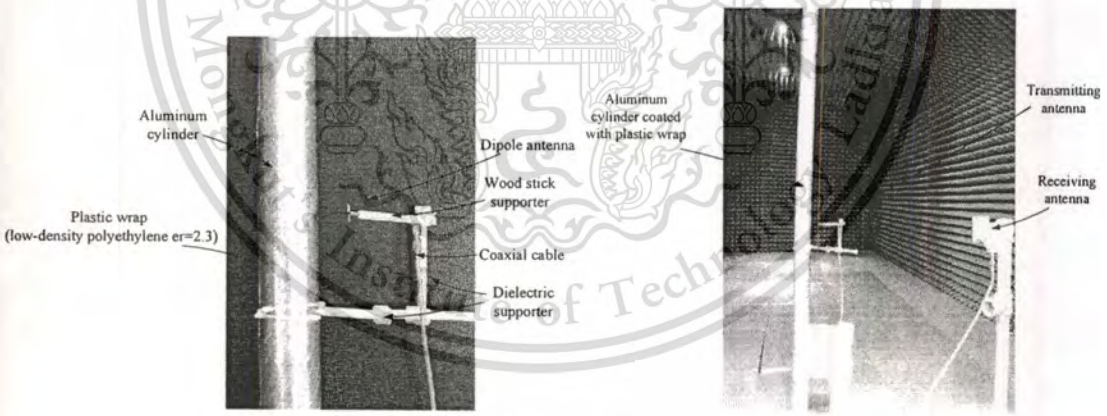

(a) (b)

Figure 4.9 Material-coated cylinder: low density polyethylene (LDPE) with $\varepsilon_r = 2.3$, $a = 1\lambda$ at 12GHz, $\rho' = 3\lambda$ and $d = 0.04\lambda$. (a) Material-coated aluminum cylinder and source (b) Measurement setup in anechoic chamber.

The measurement of the EM field around the material-coated conducting cylinder is performed to verify the accuracy of the modified 3-D UTD solution. Fig. 4.9 shows the measurement setup. The $\lambda/2$ dipole antenna is employed to represent the electric current source J_z as shown in Fig. 4.9 (a) where the λ denotes the wavelength in free-space at 12 GHz operating frequency. The monopole source is located from material-coated aluminum cylinder of $\rho' = 3\lambda$ with cylinder radius of $a = 1\lambda$. The dipole source is supported by wood stick and plastic rod. The aluminum cylinder is wrapped by low-density polyethylene (LDPE) with permittivity of $\varepsilon_r = 2.3$. The thickness of LDPE of $d = 0.04\lambda$ and $d = 0.1\lambda$ are chosen in this study. The open-end rectangular waveguide antenna is used to receive the EM field from the monopole source with vertical linear polarization as shown in Fig. 4.9 (b). The receiving antenna is located at $\rho = 25\lambda$. The different antenna heights between the transmitting and receiving antennas (i.e. $\Delta z = z - z'$) of $\Delta z = 0$ meter ($\theta = 90$ degrees) and $\Delta z = 0.15$ meter (i.e. $\theta = 76$ degrees) are performed.

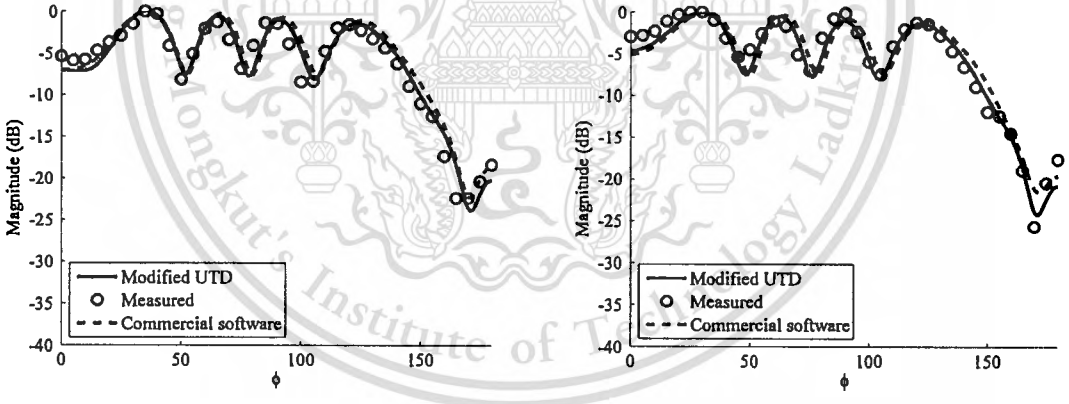

(a) $\theta = 90^\circ$ (b) $\theta = 76^\circ$

Figure 4.10 Comparison of the total field results between modified UTD and measurement results: polyethylene $\varepsilon_r = 2.3$, $a = 1\lambda$, $\rho' = 3\lambda$ and $d = 0.04\lambda$. (a) $\theta = 90^\circ$ and (b) $\theta = 76^\circ$.

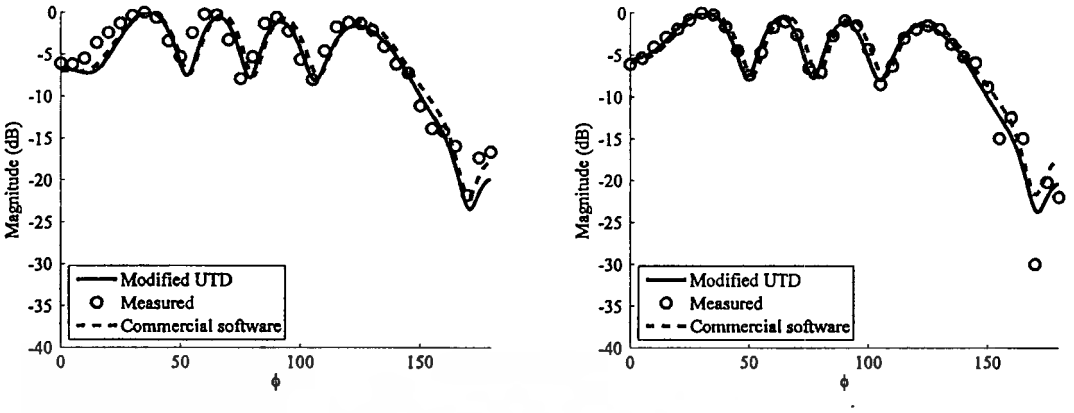

(a) $\theta = 90^\circ$ (b) $\theta = 76^\circ$

Figure 4.11 Comparison of the total field results between modified UTD and measurement results: polyethylene $\varepsilon_r = 2.3$, $a = 1\lambda$, $\rho' = 3\lambda$ and $d = 0.1\lambda$. (a) $\theta = 90^\circ$ and (b) $\theta = 76^\circ$.

Figure 4.10 shows the total field pattern in the case of the thickness of the LDPE layer of $d = 0.04\lambda$. Also, Fig. 4.11 shows the comparison results in the case of the LDPE layer of $d = 0.1\lambda$. The measurement results show good agreement with the proposed modified 3-D UTD solution and the results from the commercial software. It is confirmed that the modified 3-D UTD solution for impedance surface cylinder will be in a good accuracy for any practical applications of the thin material coated curved surface problem.

The computational time is shown in Table 3. For example, 360 field points around the cylinder are calculated by using the proposed 3-D UTD solution (including ray tracing procedure). The computational time of the proposed 3-D UTD solution is less than the CST Microwave Studio program. The computational time of modified 3-D UTD solution is less than half of the proposed 3-D UTD solution.

Table 3. Computational time of the modified 3-D UTD solution.

CPU Intel Core i7, 3.1 GHz with 24 GB of RAM			
Case: a=2λ, $\rho' = 5\lambda$, $\theta = 60°$, and d=0.08λ	CST Microwave Studio (FIT) (360 field points)	Proposed 3-D UTD solution in chapter 3 (360 field points)	Modified 3-D UTD solution (360 field points)
$\varepsilon_r = 2.1$	21 minutes, 46 seconds	102 seconds	59 seconds
$\varepsilon_r = 6$	5 hours, 33 minutes	121 seconds	61 seconds

4.7 Summary

A modified UTD solution for the convex impedance cylinder surface and its accuracy of the solution are presented. From the studies, it is shown that the 3-D UTD solution for the PEC convex surface can be heuristically modified to compute the EM field scattered from the impedance cylinder surface. The computational time is reduced by factor 2 or more. A very good comparison results between the 3-D modified UTD solution for the convex impedance cylinder surface, the EM commercial software and some selected measurement results are illustrated. The modified 3-D UTD solution for a convex impedance cylinder surface will be useful for general engineer application such as the predicting of EM wave scattered from trees, missile or aircraft. In fact, the surface of missile or aircraft is usually coated by color or absorbing thin-coated material layers. For the multilayer coating or thick coating problem, the modified 3-D UTD solution requires the new equation to approximate the surface impedance value Z_s from the actual surface.

CHAPTER 5

PATH-LOSS PREDICTION OF THE RADIO WAVE PROPAGATION IN AN ORCHARD BY USING THE MODIFIED UTD SOLUTION

5.1 Introduction

In this chapter, the proposed theoretical path-loss prediction procedure and the measured results of radio wave propagation in an orchard environment are presented. The path-loss prediction of wireless sensor network (WSN) in a durian (*Durio zibethinus Murray*) orchard is chosen to be an example of the WSN for fruit maturity monitoring system. The three-dimensional (3-D) modified uniform geometrical theory of diffraction (UTD) for curved impedance surface [28] as presented in Chapter 4 and the complex source point (CSP) technique for source modeling are employed for theoretical path-loss prediction in this chapter. The proposed numerical procedure obtained from this work is applicable to other types of orchards, such as rubber tree orchard, palm orchard, coconut orchard and other plantations for logging, with nevertheless slight changes in such physical properties of the orchard as tree size, locations of the trees, tree barks, ground types, and wave source. Besides monitoring ripening of the fruits, WSN can be used in fire monitoring system, water monitoring [3] and control system. However, it is difficult to create a model that represents every influencing factor detected in the orchard, such as the reflection and diffraction from leaves and tree branches. Because of the short communication distance in the orchard and the proximity of the transmitting and receiving antennas to the ground, merely the rays from tree trunks and the ground are studied. The durian trees in the orchard are modeled using impedance cylindrical surface structures. The orchard ground is modeled using the dielectric ground containing the relative permittivity ε_r, the relative permeability μ_r and the conductivity σ. The modified 3-D UTD scattering solution for impedance cylinder presented in [28] is obtained by heuristically modifying the classical 3-D UTD solution for a PEC curved

surface [18] with impedance Pekeris' caret function [25]. Moreover, since the wireless sensor node is attached to the outside peel of a hanging durian fruit, the fruit partially acts as a wireless sensor node. Therefore, to obtain greater accuracy in the source radiation pattern, the Gaussian beam (GB) expansion via the CSP technique is used for source modeling. The expansion of the GBs is effectively used to generate the radiation pattern.

5.2 Orchard and Source Modeling

Photographs of the orchard (Horticultural Research Center (HRC), Thailand) and a durian fruit are illustrated in Figures. 5.1(a) and 5.2(a), respectively. Typically, the height and diameter of durian trees, depending upon their species, are more than 10 meters (32.8 feet) and approximately 0.3 meter (12 inches), respectively. The proposed model is created under the assumption of no branches and leaves because as shown in Fig. 5.1(a) durian trees in the plantation have a small number of branches and leaves near the ground. In this study, the geometry of the durian trees is replaced with canonical shapes such as a simple cylinder with an impedance surface, and the actual ground with the dielectric planar surface [37]. The proposed model of the durian orchard is shown in Fig. 5.1(b). The Z_s denotes an impedance surface parameter of the cylinder, S_x is the distance of source from cylinder No. 2, S_z is the height of source above the ground, and a the durian tree radius.

(a)

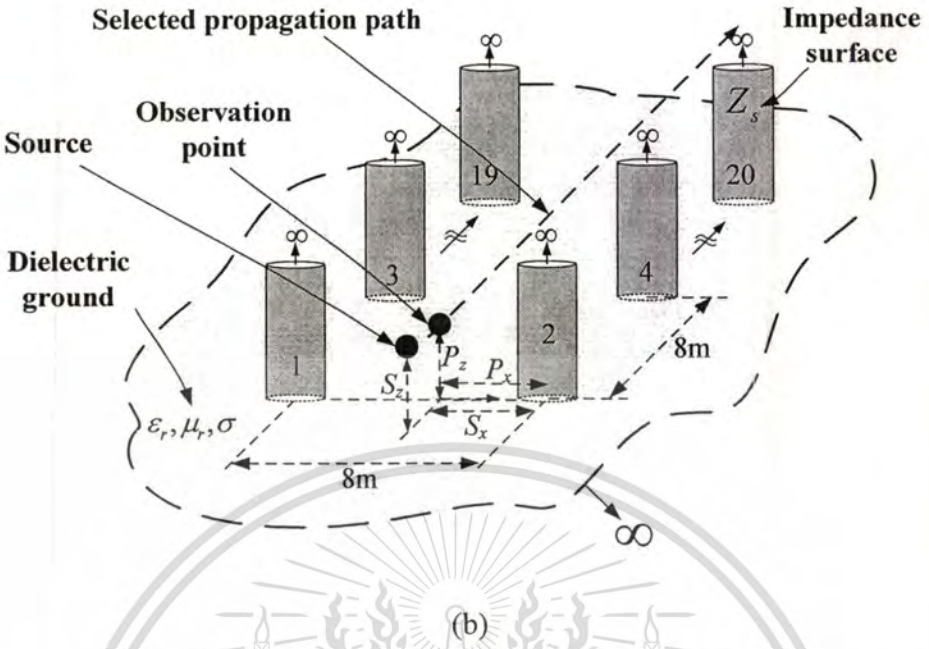

(b)

Figure 5.1 Orchard modeling: (a) durian orchard (b) model of the orchard using the canonical structure.

It was found in [16] that the path-loss is strongly affected by the source pattern of the transmitting antenna. In the WSN system under the study, a sensor device (patch antenna) is first attached onto the exterior of a durian fruit as shown in Fig. 5.2 and the communication nodes of the WSN are then installed near the ground of the durian orchard. The chosen patch antenna provides a vertical polarization (V-polarized), unidirectional pattern and operating frequency at 2.45GHz. The radiation pattern from the patch antenna attached on the durian fruit is altered due to the shape of the durian fruit. Therefore, it is necessary to carefully model the actual source in the orchard modeling. The GB expansion via CSP technique can be efficiently applied to the UTD solution [29]. The GB expansion is employed to interpolate the radiation pattern from actual source as shown in Fig. 5.2.

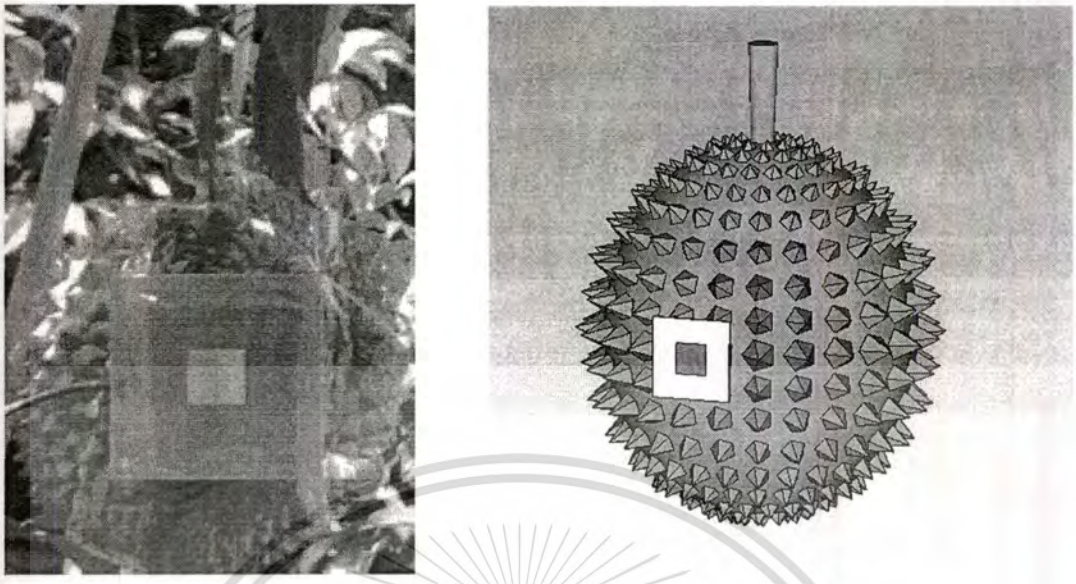

(a) (b)

Figure 5.2 (a) Vertical polarized patch antenna on a durian fruit (b) Drawing of patch antenna on a durian fruit.

5.3 Theory of the Path-loss Prediction

5.3.1 UTD Incident Field via the GB Representation

The arbitrary GB directions in 3-D case can be generated using the CSP [38] and [39] as shown in Fig. 5.3(a). The amplitude of GB rapidly decays in the same fashion as the Gaussian function when the observation point moves away from the axis of the GB. It is found that the CSP beam expansion can efficiently represent electromagnetic radiation and scattering problems because the number of GB terms can be truncated by employing the rapid decaying property of the GB to reduce the computational time [40]. This is the main advantage of using the GB expansion rather than other expansions such as the spherical wave or plane wave expansions.

The complex source location is obtained by substituting the real source location with complex source location, where the $\overline{\overline{r}}$, $\overline{\overline{\phi}}$ and $\overline{\overline{R}}$ are complex parameters. The beam

waist of GB at origin of the CSP is defined as w_0, where θ_b and ϕ_b denote the GB direction angles. The $r = \sqrt{x^2 + y^2 + z^2}$ denotes the real distance of the observation points when $x = r\sin\theta\cos\phi$, $y = r\sin\theta\sin\phi$ and $z = r\cos(\theta)$. The real source location is defined as $x' = r'\sin\theta'\cos\phi'$, $y' = r'\sin\theta'\sin\phi'$ and $z' = r'\cos(\theta')$. The complex source location can then be expressed as $\tilde{x}' = x' - jb\sin\theta_b\cos\phi_b$, $\tilde{y}' = y' - jb\sin\theta_b\sin\phi_b$ and $\tilde{z}' = z' - jb\cos\theta_b$, where $\tilde{r}' = \sqrt{\tilde{x}'^2 + \tilde{y}'^2 + \tilde{z}'^2}$. Thus, the distance between the source point and the observation point can be written as $\tilde{R} = r - \tilde{r}'$. To construct radiation pattern of source, the expansion of Gaussian beams can be expressed with

$$E(\tilde{R}) = \sum_{n=1}^{N} a_n \frac{e^{-jk\tilde{R}}}{\tilde{R}}. \tag{5.1}$$

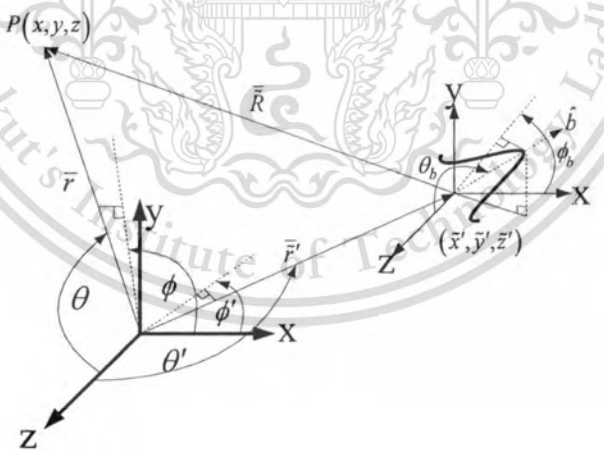

(a)

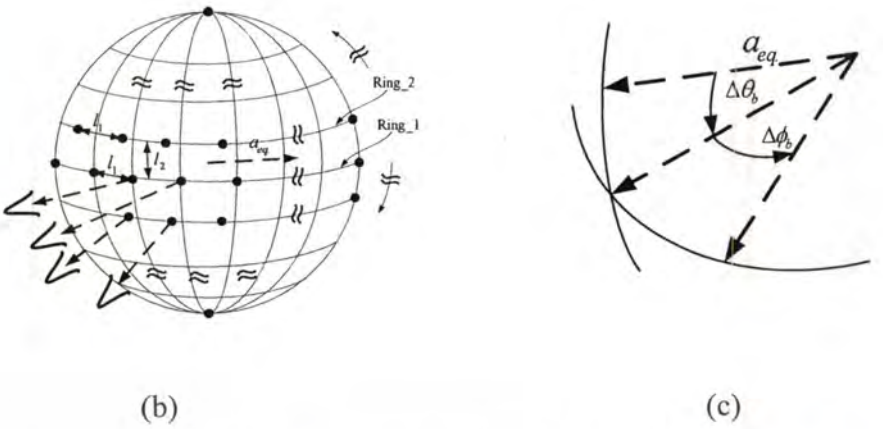

(b) (c)

Figure 5.3 Antenna pattern representation: (a) CSP for constructing the GB, (b) the summation of arbitrary directions of GBs, (c) the spacing angles between GBs.

The $E(\tilde{R})$ denotes the radiation pattern function at any observation point. The unknown sampling field coefficients of the total number of the GBs (N) are defined by a_n, which can be determined using point matching together with the actual source radiation pattern from measurement. Fig. 5.3(b) shows the equivalent sphere with radius $a_{eqv.}$=1. The $\Delta\phi_b = \Delta\theta_b$ denotes the delta sampling angles of GB as shown in Fig. 5.3(c). Thus, the number of GBs on the equivalent ring on the equivalent sphere varies depending upon the location of equivalent ring on the equivalent sphere. The GBs with different coefficients a_n are located at the origin of equivalent sphere. As previously mentioned, the unknown coefficients a_n can be determined with point matching of the actual sampling field radiation pattern obtained from measurement. The patch antenna attached on the durian fruit is supported by the planar supporter made of polyurethane foam and wood as shown in Fig. 5.4(a). The sampling field was measured by varying in 10-degree incremental steps the θ and ϕ angles. Finally, the field strength (linear scale) is normalized to the maximum value to determine the GB coefficients a_n. Fig. 5.4(b) shows the experiment and the synthesis of the normalized field pattern. The comparison indicates good agreement. In this work, to reduce the computational time, 10 degrees of the sampling angles and the beam waist of GB with 1λ are selected.

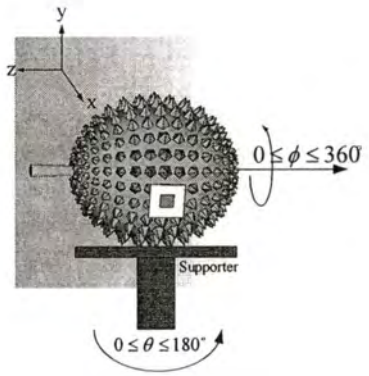

(a)

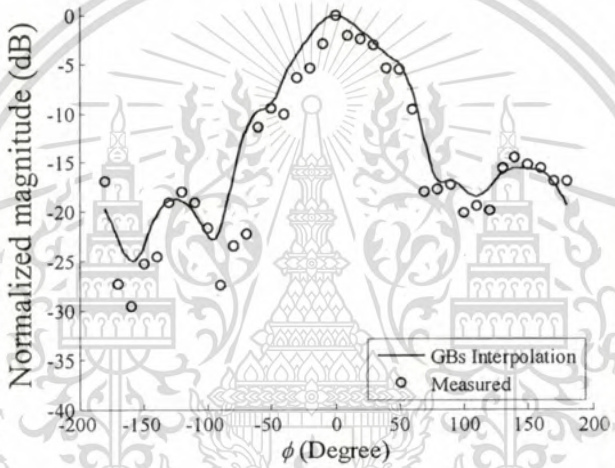

(b)

Figure 5.4 (a) The diagram of the radiation pattern measurement of the patch antenna on durian fruit (b) 2-D source radiation pattern.

4.3.2. UTD Canonical Problem and Equations

Figure 5.5 shows all possible ray paths in the orchard model. Fig. 5.5(a) shows the cylindrical structure with 3-D diffracted ray paths, Fig. 5.5(b) illustrates all ray paths of a single cylinder at different regions, i.e. front and rear of the shadow boundary (SB), and *Fig.* 5.5(c) is the dielectric ground model and its reflected ray path. The actual ground is modeled using the dielectric ground model [37]. The total field, i.e. vertical polarization source, at the observation point of the proposed procedure consists of the incident field

$u_i(P)$, the reflected field $u_r(P)$ from all of the impedance cylinders, the diffracted fields $u_d(P)$ from two sides of all impedance cylinders in the orchard model, and the reflected field from dielectric ground u_r^{ground}. The total field u_t of the proposed procedure can be written as

$$u_t = u_t^{lit}(P) + u_d(P). \tag{5.2}$$

The u_t^{lit} is the field at the observation point P in the lit region which can be written as

$$u_t^{lit}(P) = u_i(P) + \underbrace{\sum_{m=1}^{M} u_i^m\left(Q_R^m\right) R_{s,h}^m A_{lit}^m e^{-jks_r^m}}_{\text{All reflected field from impedance cylinders}} + u_r^{ground} \tag{5.3}$$

where M denotes total number of impedance cylinders in the orchard model. It is noted that the results of actual radiation pattern obtained from the previous section using GB expansion technique are used as the incident field in this work. $R_{s,h}$ denotes the reflection coefficients of the curved surface, which consist of the Fresnel's function and the Pekeris' caret function. The subscripts s and h refer to soft (i.e., electric field incident parallel to the axis of cylinder) and hard polarizations (i.e., magnetic field incident parallel to the axis of cylinder) of the incident wave. A_{lit} represents the 3-D spreading factor in the lit zone conditional upon incident wave types and surface geometry. S_r denotes reflected path length of each impedance cylinder. The diffracted fields $u_d(P)$ from the surface Q_2 of all cylinders to the observation point P are shown in Figs. 5.5 (a) and (b). The $u_d(P)$ of M cylinders can be written as

$$u_d(P) = \sum_{m=1}^{M} u_i^m\left(Q_1^m\right) T_{s,h}^m A_{shadow}^m e^{-jks_d^m}. \tag{5.4}$$

The $u_i(Q_1)$ denotes the incident field at the incident diffraction point Q_1 of each cylinder, and S_d denotes the diffracted path length. The transmission coefficients $T_{s,h}$ consisting of the Fresnel's function and the Pekeris' caret function can be numerically

computed. A_{shadow} denotes the 3-D spreading factor in the shadow zone depending on the surface geometry. The parameters in Equations (5.3) and (5.4) can be found in [18], and the details of the modified 3-D UTD solution for an impedance cylinder surface are presented in [28].

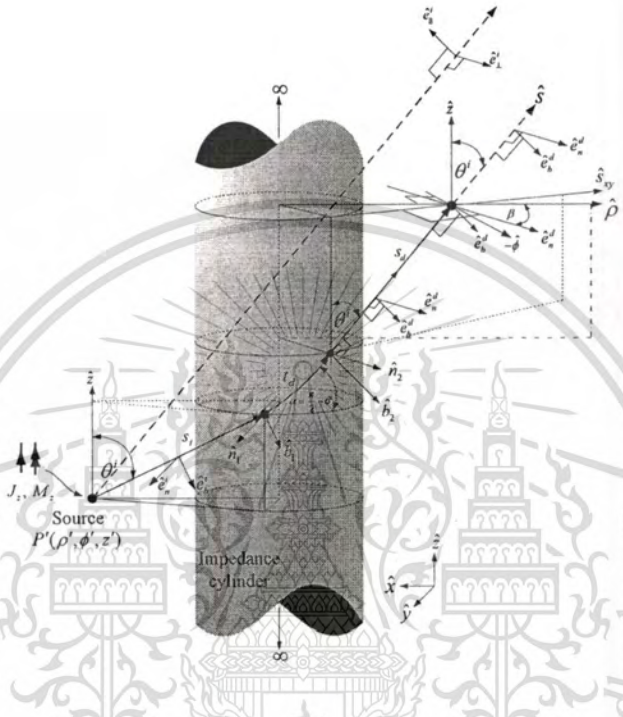

(a)

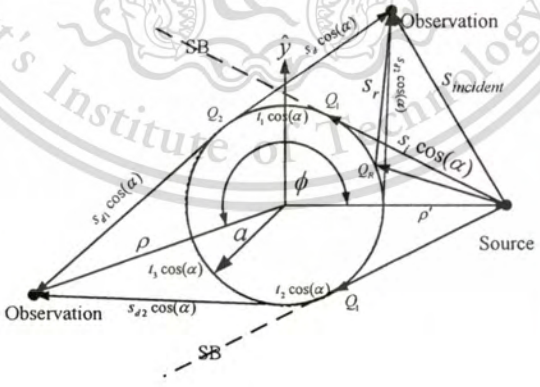

(b)

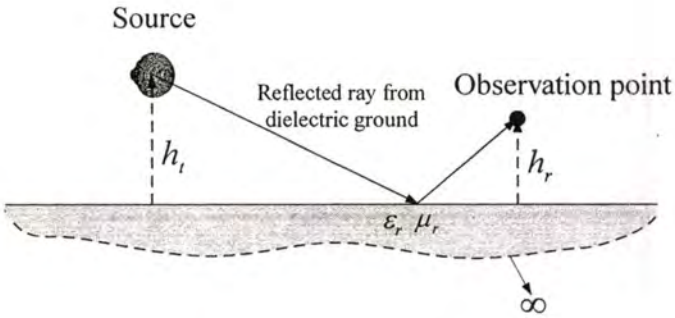

(c)

Figure 5.5 Geometrical modeling of a tree: (a) Tree model using impedance cylinder and diffracted ray paths, (b) ray mechanisms of a cylinder, (c) dielectric ground model and reflected ray path.

Generally, the numerical scheme to calculate PEC Pekeris' caret integral function $P_{s,h}(\xi^L)$ is unavailable for a curved impedance surface. In this dissertation, the numerical integration based on the recursive adaptive Simpson Quadrature is applied. To verify the accuracy of the proposed idea using the numerical integration, the comparison between the proposed solution and the simulation results from the CST Microwave Studio program of single impedance cylinder is shown in Fig. 5.6. The value of surface impedance Z_S of a thin material coating on a PEC cylinder derived from the approximation of the problems was presented in [41]. The axis of cylinder is located along z-axis. The θ angle is measured from z-axis to the observation point. It is noted that the proposed UTD solution can automatically recover the 2-D case when the incident angle becomes perpendicular to the cylinder axis. As shown in Fig. 5.6, the numerical results obtained from the proposed UTD solution were in line with the results from CST program for both normal (2-D case) and oblique (3-D case) incidents.

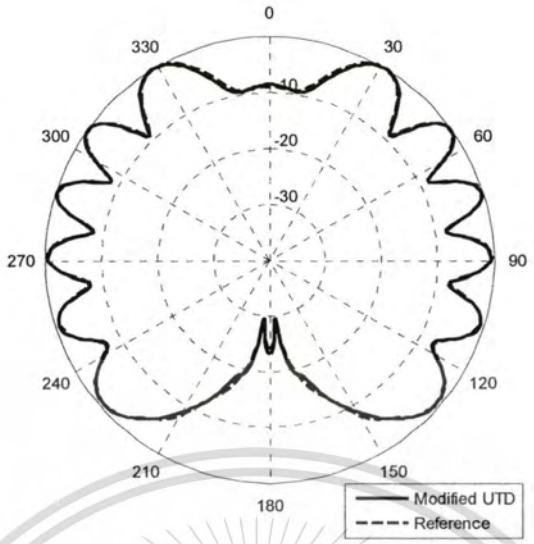

(a) $\theta = 90^{\circ}$ (2-D case)

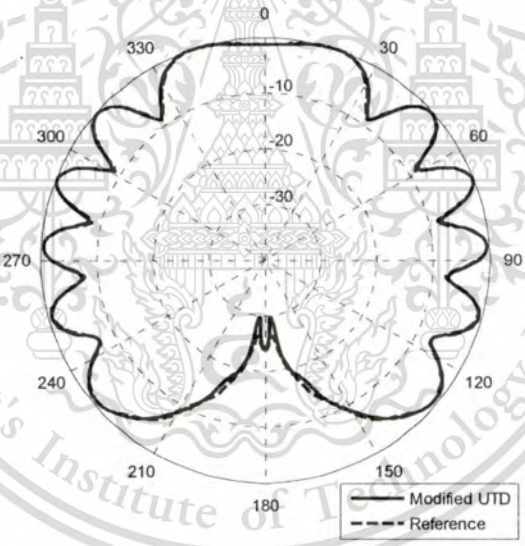

(b) $\theta = 70^{\circ}$ (3-D case)

Figure 5.6 Comparison of the total field (vertical dipole source) between the modified UTD and CST Microwave Studio program (reference) versus ϕ angle: $a = 2\lambda$, $\rho' = 5\lambda$, $t = 0.06\lambda$, $\varepsilon_r = 4$, $\mu_r = 1$ and $\rho = 100\lambda$.

5.4 Measurement Setup

The path-loss measurement was performed in a durian orchard of the Horticultural Research Center (HRC), Khlung, Chanthaburi, Thailand. The spacings

between any two durian trees are horizontally and vertically 8 meters. The photographs of the measurement setup and the locations of transmitter and receiver are shown in Fig. 5.7. The average diameter of durian trees is 0.3 meter (a = 0.15 meter). The vertical polarized antennas for source and observation point are employed. The source antenna is attached on a durian fruit with S_z = 2.2 meters and S_x = 1.5 meters as shown in Fig. 5.7(b). The handheld spectrum analyzer as shown in Fig. 5.7(c) is used to receive the field strength at the observation points along the measurement path. The receiving antenna is located at P_z = 1.5 meters and P_x = 1.5 meters as shown in Fig. 5.7(c). The overall distance of propagation measurement is 80 meters. The sampling distance for measurement of 4 meters was chosen along the propagation path.

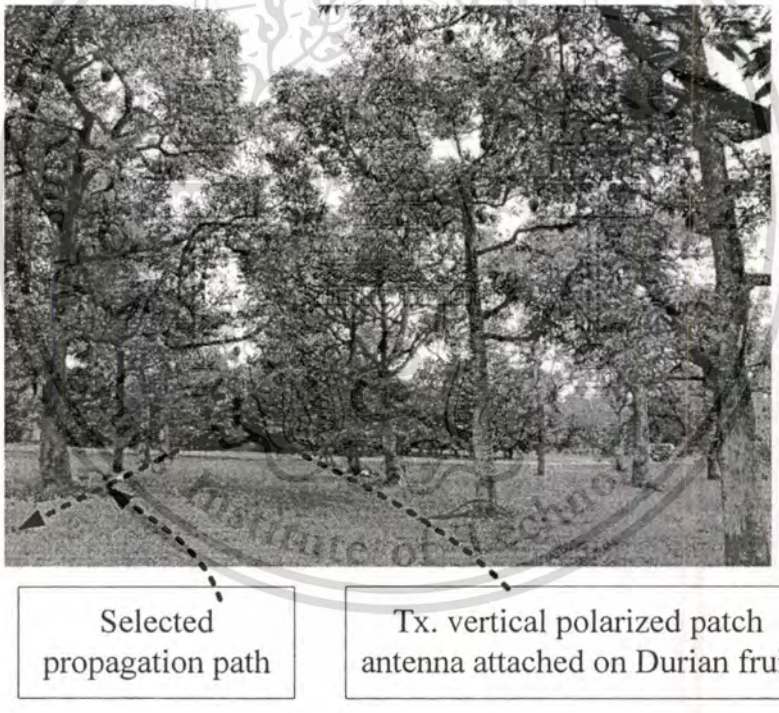

(a)

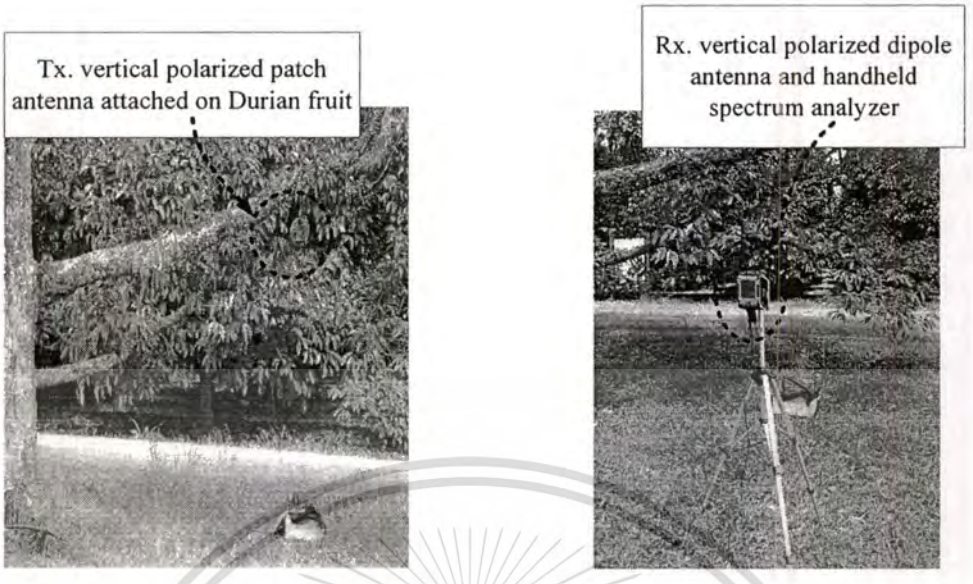

(b) (c)

Figure 5.7 Measurement setup: (a) the propagation path view, (b) patch antenna on durian fruit and its location, (c) 2.45GHz handheld spectrum analyzer.

5.5 Numerical and Measured Results

Many research works have studied on the relative permittivity of the various species of wood [42] and [43]. In the measurement results presented in [42] and [43], at the percentage of moisture contents below 50%, the relative permittivity of wood of approximately ε_r=(2 to 6)-j(0.1 to 2.828) depends on the percentage of moisture contents and structural direction of wood. Due to relative permittivity of the durian wood is unavailable, the value of the relative permittivity of the cylindrical surface of ε_r = 4.77-j2.828 is used in this work, which comes from the measurement result of dielectric properties of the oriental beech species with moisture content 28% at microwave frequencies (2.45GHz) in [42].

The dielectric constants of the various kinds of the actual ground have been reported in [37], [44] and [45]. The average ground with σ=5×10^{-3} S/m and ε_r=15 represents the actual ground in this work. The distances between any two durian trees are horizontally and vertically 8 meters. The average radius of durian trees is 0.15 meter (a = 0.15 meter). S_z = 2.2 meters, S_x = 1.5 meters, P_z = 1.5 meters and P_x = 1.5 meters. The

overall distance for propagation measurement is 80 meters. The field distributions in the communication area (i.e., the rectangular area as shown in Fig. 5.8) normalized to the maximum value of all plots are shown in Fig. 5.9. Fig. 5.9(a) shows the total field distribution which consists of the incident ray and scattered rays from cylinders without reflected ray from ground. Fig. 5.9(b) shows the total field plot without scattered rays from impedance cylinders. Fig. 5.9(c) shows the total field distribution which consists of the incident ray, reflected ray from ground and scattered rays from cylinders (i.e., all possible ray paths of the proposed model). In Fig. 5.9(a), the scattered rays from cylinders significantly contribute to the total field in the far region of the communication area. The total field strength in Fig. 5.9(a) is slightly changed when compared to that in Fig. 5.9(c) except in the 45-60 meters region. Fig. 5.9(b) shows the total field without scattered field from impedance cylinders. The reflected ray from ground is strong near the source and also show null of the total field in the region of 45-60 meters. The total field strength increases again in the region from 60 meters to 80 meters. Importantly, if the position of trees is not uniform in the orchard or the density of trees is changed, the field distribution plot of the total field strength in the communication area can be readily calculated using the proposed numerical procedure. However, under the same conditions, the total field strength cannot be computed with the empirical models [6]-[10]. This field distribution plot provides useful information as to the location to install the communication node around the sensor node (source) in the orchard. The plots in Fig. 5.9 show that the UTD solution provides physical insight of the problem since each field contribution can be quantitatively extracted.

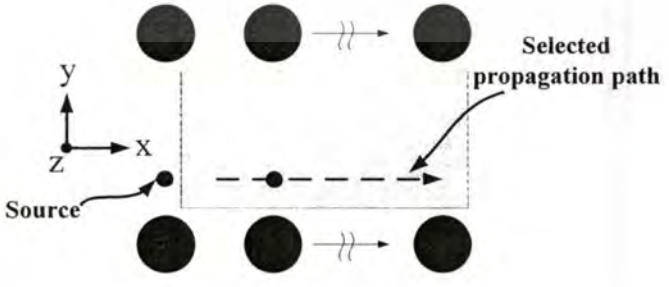

Figure 5.8 Selected area in the orchard modeling

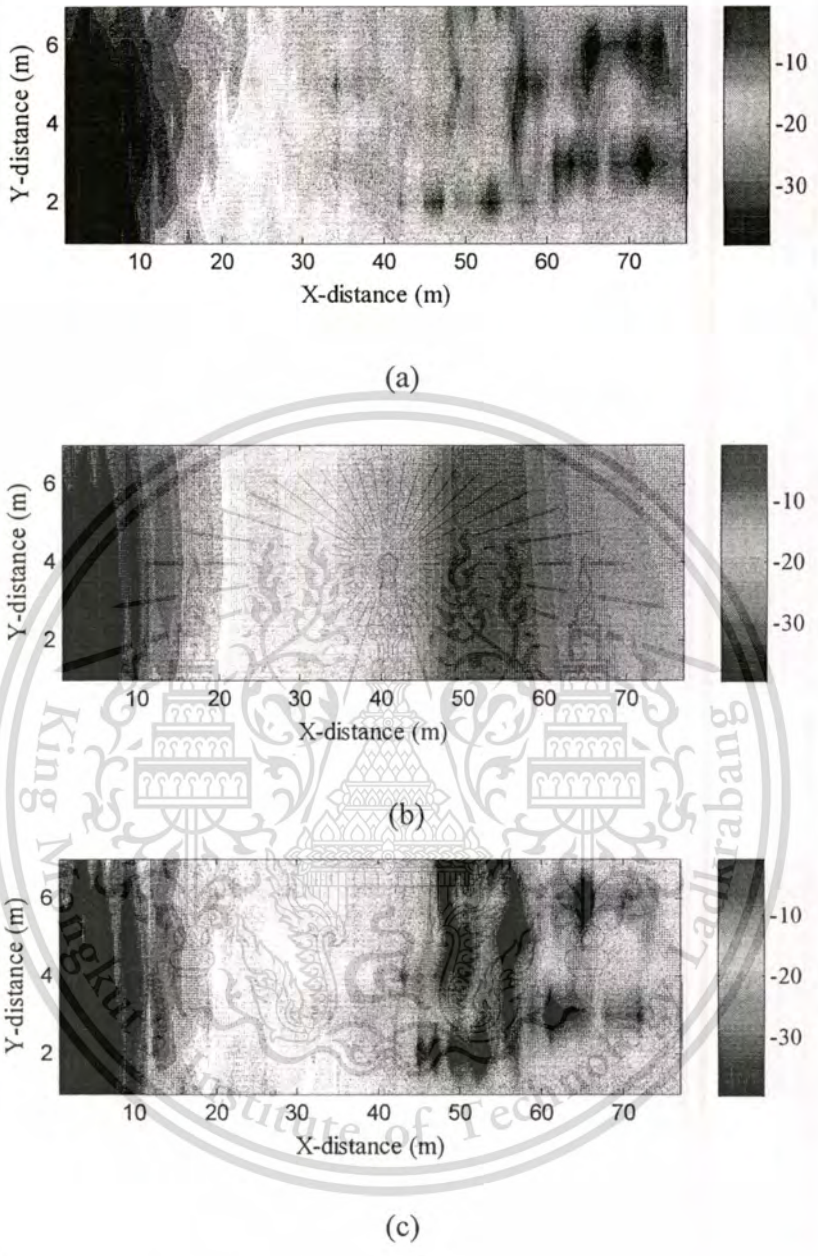

Figure 5.9 Normalized total field in the considered area: (a) without reflected ray from ground (i.e., only incident ray and scattered rays from cylinders), (b) without scattered ray from cylinders (i.e., only incident ray and reflected ray from ground), and (c) Normalized total field (i.e., incident ray, reflected ray from ground and scattered rays from cylinders).

Figure 5.10 shows the comparison between path loss of the numerical and measured results. The numerical results are calculated with two ground surface types and

all PEC surfaces (i.e., ground and cylinders). The two ground surface types are average ground and grass-covered ground. In this dissertation, the impedance cylindrical surface of the oriental beech wood species [42] with ε_r= 4.7-j2.828 is used in the proposed model. This value varies according to different wood surfaces. The dielectric coated thickness in the UTD model of 0.06λ is chosen. Nevertheless, the dielectric coated thickness, the radius a and position of the trees can be altered to suit different scenarios. The circle line is the measurement results along the propagation path of 80 meters sampling every 4 meters. In Fig. 5.10, the numerical results from the proposed UTD solution for the average ground, the grass-covered ground and all PEC surfaces are shown with the dashed line, the solid line and dotted line, respectively. The difference in numerical path loss predictions of two ground types is insignificant. Within the range of 4-50 meters, the numerical results show good agreement with the measured result. The prediction shows discrepancies in the range of 50-80 meters due to the incident field and reflected field dramatically decreasing in the far region. In fact, the multipath fading caused by multiple reflections from a group of leaves, surface wave of ground and multiple diffractions from trees is stronger than incident field from source and reflected field from ground at the far region. However, due to low transmitting power of both the sensor and communication nodes of the WSN, the communication range is usually limited to 40 meters or less. Therefore, the proposed method will be adequate for the proposed scenario. To improve the accuracy of path loss prediction at the far region in the future research, the proposed numerical procedure requires more field components such as the surface wave of dielectric ground and multiple reflections/diffractions from a group of leaves. Moreover, it is found that the field strength of all PEC surfaces (i.e., dotted line in Fig. 5.10) fluctuated along the propagation path due to strong constructive and destructive effects among incident field, reflected field from ground, and scattered fields from cylinders. This causes the reflection from ground and scattered field from cylinders in the PEC case to be stronger than in the case of impedance surface cylinders with dielectric ground. Therefore, the PEC surface model cannot be used to accurately predict the path loss in this scenario.

The comparison results in Fig. 5.11 are from the proposed solution and the empirical models for the forest. The two-ray model, Weissberger model and Chen&Kua model are presented in the empirical models [7]- [9]. The two-ray model shows multiple nulls of total field along the propagation path, causing the two-ray model to become invalid in certain propagation range (i.e., null field region). Both Weissberger model and Chen&Kua model show a large error of path loss prediction since the models are based on the wave propagation through a group of leaves. On the other hand, the proposed solution shows very good agreement for the range within a 50-meter limit, and such a solution is sufficiently good for designing a WSN in the orchard.

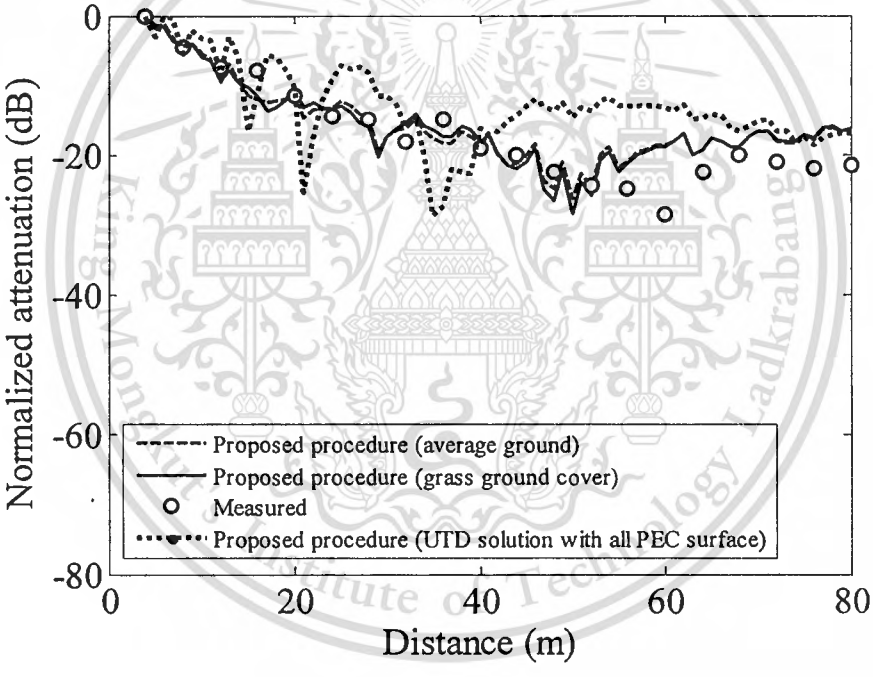

Figure 5.10 Comparison between path loss of the numerical and measured results at 2.45GHz: average ground (σ = 5×10 $^{-3}$ S/m and ε_r=15) and grass-covered ground (σ = 0.163 S/m and ε_r=8), both with impedance cylindrical surface (ε_r= 4.7-j2.828 and t = 0.06 λ) and with PEC surface.

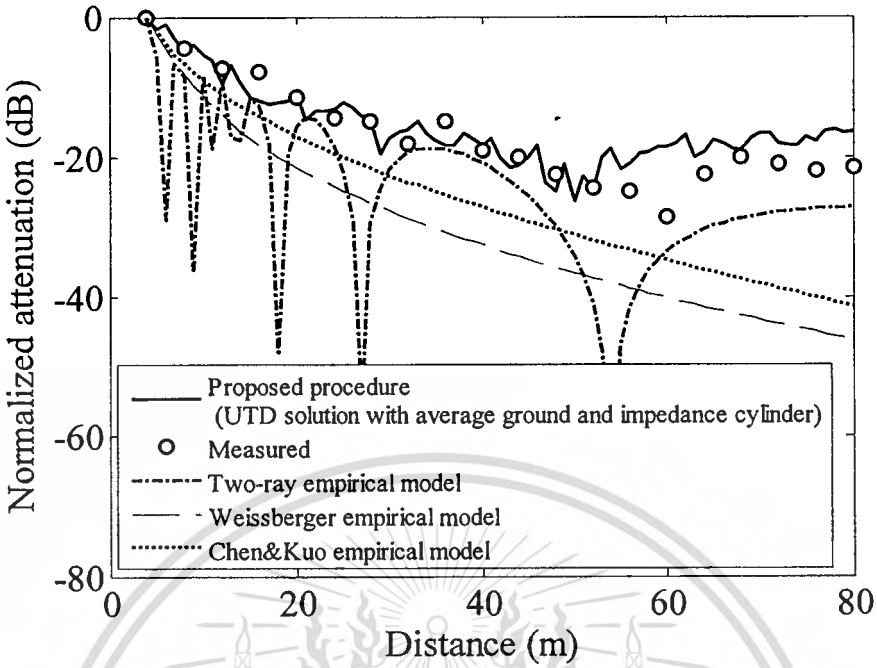

Figure 5.11 Comparisons of empirical models and path losses of the numerical and measured results at 2.45GHz

5.6 Summary

The path-loss prediction of radio wave propagation in an orchard using the modified UTD method has been proposed. The numerical procedure for path-loss prediction using the modified 3-D UTD solution for the impedance cylindrical surface together with the GB expansion via the CSP technique is presented in this chapter. The UTD can efficiently deal with all kinds of scattered rays from the trees and the ground in the durian orchard. The UTD method provides the physical insight into the results. The study of the effects of field distribution using UTD (i.e., incident, reflected and scattered fields) on the total field is possible despite the fact that the effects cannot be computed by any other numerical method. The GB can be used to construct the source pattern that takes into account both the durian fruit and the antenna attached on the fruit. The numerical results manifest that the modified 3-D UTD for the impedance cylindrical surface can be used to accurately calculate the total field, under the assumption that the difference in height of transmitting and receiving antennas is within a few meters. The proposed numerical path-loss prediction procedure using the modified 3-D UTD solution

will be efficiently used in various environments, such as in the network planning of the WSN in an orchard and in other settings for which the orchard physical dimensions are required.

CHAPTER 6
CONCLUSION
AND REMARK FOR FUTURE STUDIES

6.1 Conclusion

The 3-D UTD solutions for EM wave scattered from 3-D smooth curved impedance surface are proposed. The proposed 3-D UTD solution is constructed from the 3-D Green's functions. The heuristic modified 3-D UTD solution for EM wave scattered from 3-D smooth curved impedance surface is also developed from the classical 3-D PEC UTD solution. The proposed 3-D UTD solution based on the 3-D Green's function recovers the original 3-D PEC UTD solution with surface impedance value equals zero ($Z_s = 0$). Moreover, the proposed 3-D UTD solution recovers the classical 2-D UTD solutions for EM wave scattered from 2-D smooth curved impedance surface. Also, the computational time can be reduced by using the modified 3-D UTD solution in case of small transmitting and receiving antenna heights. This dissertation also demonstrates that the numerical integration based on the recursive adaptive Simpson Quadrature can be employed to calculate the new 3-D impedance Fock-type integrals functions accurately.

The application of the proposed 3-D UTD solution is also demonstrated. The theoretical path-loss prediction procedure is completely constructed using the proposed 3-D UTD solution. The comparison between the numerical results and measured results of radio wave propagation in an orchard environment are in very good agreement. The proposed numerical procedure to calculate the path loss from actual scenario of the orchard is useful for network planning such as the pre-harvesting WSN system and other scenarios.

6.2 Remark For Future Studies

The 3-D exact Green's functions for the EM wave scattered from impedance cylinder was presented in chapter 3. The solution will be able to analyze the EM radiation and coupling from the impedance cylinder as shown in Fig. 6.1. Moreover, the proposed methods and procedure in chapter 3 will be able to analyze the EM radiation and

coupling from the impedance sphere as shown in Fig. 6.2. The UTD solution for the radiation problem will be useful to predict EM fields that are radiated from the antenna on the curved impedance surface. Moreover, the UTD solution for coupling problem will be useful to predict the coupling EM fields of the antennas on the curved impedance surface.

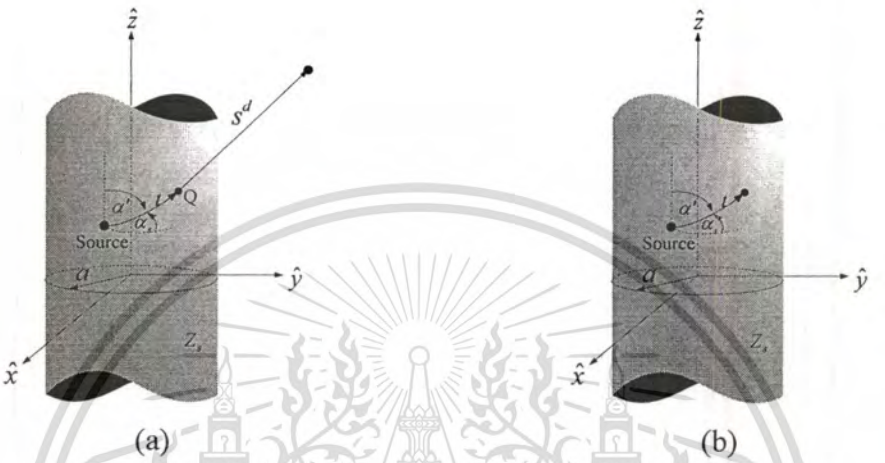

Figure 6.1 Impedance cylinder problem: (a) Radiation problem and (b) coupling problem.

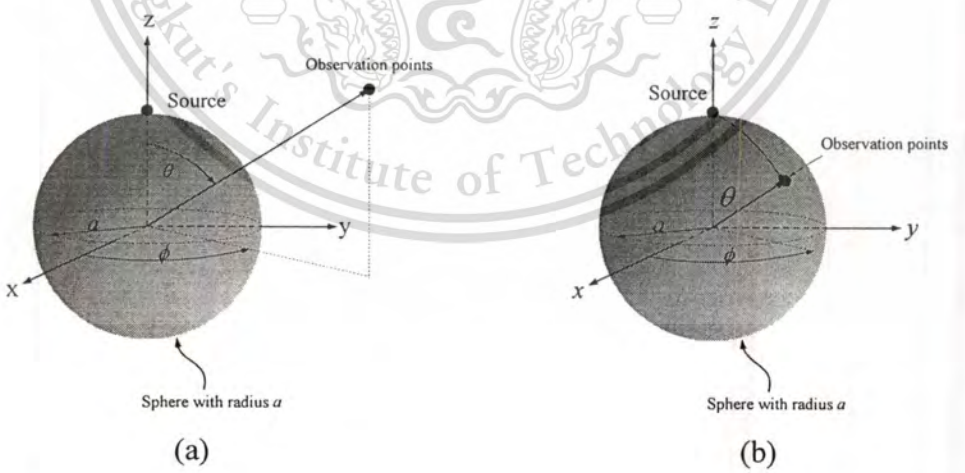

Figure 6.2 Impedance sphere problem: (a) Radiation problem and (b) coupling problem.

APPENDICES

APPENDIX A

Green's Functions

A mathematical tool called Green's function technique is generally employed to solve the differential equation in the electromagnetic (EM) wave problem. Firstly, the differential equations of the considered problem will be mentioned. Next, the EM wave solution using the Green's function will be proposed.

From [34], the scalar Helmholtz equation in the cylindrical coordinate can be written as

$$\left(\nabla^2 + k^2\right)\psi = 0 \tag{A-1}$$

or

$$\left(\frac{1}{\rho}\frac{\partial}{\partial\rho}\left(\rho\frac{\partial}{\partial\rho}\right)+\frac{1}{\rho^2}\frac{\partial^2}{\partial\phi^2}+\frac{\partial^2}{\partial z^2}+k^2\right)\psi = 0. \tag{A-2}$$

Using the separation of variable technique, the solution ψ can be written as

$$\psi = R(\rho)\Phi(\phi)Z(z). \tag{A-3}$$

Substituting Equation (A-3) into (A-2) and divided by $R(\rho)\Phi(\phi)Z(z)$, Equation (A-2) can be written as

$$\left(\frac{1}{\rho R}\frac{\partial}{\partial\rho}\left(\rho\frac{\partial R}{\partial\rho}\right)+\frac{1}{\Phi\rho^2}\frac{\partial^2\Phi}{\partial\phi^2}+\frac{1}{Z}\frac{\partial^2}{\partial z^2}+k^2\right)=0 \tag{A-4}$$

Generally, Using the radiation condition of traveling wave in z-domain, suppose the solution of Z can be written as

$$Z \sim C_z e^{-jk_z(z)} \tag{A-5}$$

thus

$$\frac{1}{Z}\frac{\partial^2\left(Ce^{-jk_z(z)}\right)}{\partial z^2} = (-jk_z)(-jk_z)\frac{1}{Z}Z = -k_z{}^2 . \tag{A-6}$$

In the same manner as above, the Φ wave function satisfies the periodic condition of traveling wave in ϕ direction. Φ function can also be written as

$$\Phi \sim C_\phi \sum_{n=-\infty}^{\infty} e^{-jv(\phi-2n\pi)}, \tag{A-7}$$

consider the dominant mode which is n=0, suppose Φ function can be written as

$$\Phi \sim C_\phi e^{-jv(\phi)} . \tag{A-8}$$

Multiply Equation (A-4) by ρ^2, thus

$$\frac{1}{\Phi}\frac{\partial^2\left(C_\phi e^{-jv(\phi)}\right)}{\partial\phi^2} = \frac{1}{\Phi}(-jv)(-jv)\Phi = -v^2 \tag{A-9}$$

where C_z and C_ϕ are constants.

Equation (A-4) multiplied by ρ^2 together with Equations (A-6) and (A-9) can be simplified as

$$\left(\frac{\rho}{R}\frac{\partial}{\partial\rho}\left(\rho\frac{\partial R}{\partial\rho}\right) - v^2 + (k^2 - k_z{}^2)\rho^2\right) = 0 . \tag{A-10}$$

Using $k^2 = k_\rho{}^2 + k_z{}^2$, thus

$$\left(\frac{\rho}{R}\frac{\partial}{\partial\rho}\left(\rho\frac{\partial R}{\partial\rho}\right) - v^2 + (k_\rho^2)\rho^2\right) = 0 . \tag{A-11}$$

The separated equations can be summarized as

$$\left(\rho\frac{\partial}{\partial\rho}\left(\rho\frac{\partial R}{\partial\rho}\right)+\left((k_\rho\rho)^2-v^2\right)R\right)=0. \tag{A-12a}$$

$$\left(\frac{\partial^2}{\partial\phi^2}+v^2\right)\Phi=0 \tag{A-12b}$$

$$\left(\frac{\partial^2}{\partial z^2}+k_z^2\right)Z=0 \tag{A-12c}$$

Green's function technique is a mathematical tool employed to solve the inhomogeneous differential of the electromagnetic (EM) wave equations such as

$$\left(\nabla^2+k^2\right)A_z^{J_z}=-\mu_0 J_z \tag{A-13a}$$

and

$$\left(\nabla^2+k^2\right)F_z^{M_z}=-\varepsilon_0 M_z. \tag{A-13b}$$

The J_z and M_z denote the electric and magnetic point current sources. The $A_z^{J_z}$ and $F_z^{M_z}$ denote the scalar potential functions in the EM problems. The $\delta\left(\bar{R}-\bar{R}'\right)$ denotes the Dirac delta function or called impulse function which is generally employed to represent the point current source. Green's function is a solution of the inhomogeneous differential equation defined as

$$\left(\nabla^2+k^2\right)G=-\delta\left(\bar{R}-\bar{R}'\right). \tag{A-14}$$

In the cylindrical coordinate, the Dirac delta function can be written as

$$\delta\left(\bar{R}-\bar{R}'\right)=\frac{\delta(\rho-\rho')}{\rho}\delta(\phi-\phi')\delta(z-z'). \tag{A-15}$$

Thus, Equation (A-14) is rewritten as

$$\left(\nabla^2+k^2\right)G=-\frac{\delta(\rho-\rho')}{\rho}\delta(\phi-\phi')\delta(z-z'). \tag{A-16}$$

The alternative representation of the Green's function in the closed contour integral is presented in [21]. The deep details of the derivation can be found in the unpublished class note [22]. The Green's function G can be written as

$$G=\tilde{K}\oint_{C_u} d\lambda_u \oint_{C_v} d\lambda_v \left[G_u G_v G_w\right]. \tag{A-17}$$

Let consider $G_u = G_\rho$, $G_v = G_z$ and $G_w = G_\phi$, substituting the Equation (A-17) into (A-16) together with the separation of variable technique, three differential equations including Dirac delta functions of each domain are obtained as follows

$$\left(\frac{\partial}{\partial\rho}\rho\frac{\partial}{\partial\rho}+\lambda_u\rho-\frac{\lambda_v}{\rho}\right)G_\rho=-\delta(\rho-\rho'), \tag{A-18a}$$

$$\left(\frac{\partial^2}{\partial\phi^2}+\lambda_v\right)G_\phi=-\delta(\phi-\phi'), \tag{A-18b}$$

and

$$\left(\frac{\partial^2}{\partial z^2}+\lambda_z\right)G_z=-\delta(z-z') \tag{A-18c}$$

where $\lambda_u = k_\rho^2 = k^2 - k_z^2$, $\lambda_v = v^2$ and $\lambda_z = k_z^2$. The $\tilde{K}$ is a constant. The solutions of each Equations (A-18a-A18b) are defined below.

- Equation (A-18), the G_ϕ satisfies the periodic boundary condition as

$$\begin{aligned} G_\phi &= -\frac{\cos\sqrt{\lambda_v}(\pi-|\phi-\phi'|)}{2\sqrt{\lambda_v}\sin\sqrt{\lambda_v}(\pi)} \\ &= \sum_{n=-\infty}^{\infty}\frac{e^{-j\sqrt{\lambda_v}|\phi-\phi'-2n\pi|}}{2j\sqrt{\lambda_v}} \end{aligned}, \tag{A-19}$$

consider only first term (dominant), let $n=0$, G_ϕ can be written as

$$G_\phi = \frac{e^{-j\sqrt{\lambda_v}|\phi-\phi'|}}{2j\sqrt{\lambda_v}}. \tag{A-20}$$

- The G_z satisfy the radiation condition $\lim_{z\to\pm\infty}\left(\frac{d}{dz}\pm j\sqrt{\lambda_z}\right)G_z=0$, G_z function can be written as

$$G_z=\frac{e^{-j\sqrt{\lambda_z}|z-z'|}}{2j\sqrt{\lambda_z}} \tag{A-21}$$

- The G_ρ satisfy both of the surface boundary conditions at $\rho=a$ and the radiation condition at $\rho=\infty$ of $\lim_{\rho\to\infty}\left(\frac{d}{d\rho}+j\sqrt{\lambda_u}\right)G_z=0$, G_z function can be written as

$$G_\rho=-\left(\frac{j\pi}{2}\right)\left(J_\nu(k_\rho\rho_<)+\tilde{\mathrm{B}}H_\nu^{(2)}(k_\rho\rho_<)\right)H_\nu^{(2)}(k_\rho\rho_>), \tag{A-22}$$

where $\tilde{\mathrm{B}}$ is a constant that contain the surface properties. The G_ρ can be constructed using the Green's function construction [21] and [34].

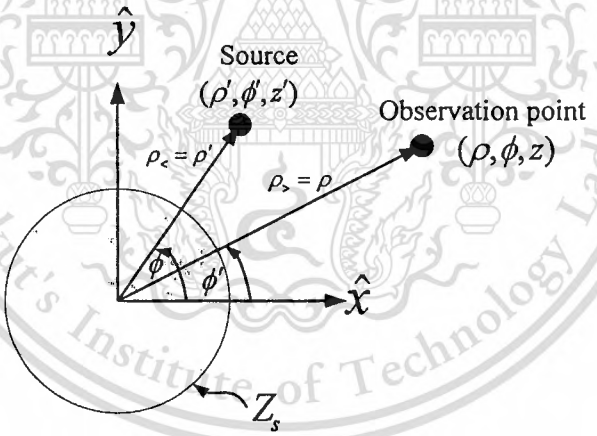

Figure A.1 Cylinder problem

Note that, the PEC surface Boundary Condition (BC) at $\rho=a$ are as follows

$$G_\rho=0 \quad \text{for E-mode (s-polarized),} \tag{A-23a}$$

$$\frac{\partial G_\rho}{\partial\rho}=0 \quad \text{for H-mode (h-polarized).} \tag{A-23b}$$

The general BC is defined as

$$\frac{\partial G_\rho}{\partial \rho} = -jk_\rho \tilde{C} G_\rho \tag{A-24}$$

where $\tilde{C}$ is a constant and may be related to the surface impedance of the cylinder. In case of the PEC surface, $\tilde{C} = \infty$ for E-mode and $\tilde{C} = 0$ for H-mode, respectively. The constant $\tilde{K}$ in Equation (A-17) is found in [22] as $\tilde{K} = 1/4\pi^2$. Finally, the Green's function can be written as

$$G = \frac{1}{4\pi^2} \int_{C_\nu} \int_{C_{k_z}} e^{-jk_z(z-z')} e^{-j\nu(\phi-\phi')} \left(G_\rho\right) d\nu dk_z \tag{A-25}$$

and

$$G_\rho = -\left(\frac{j\pi}{2}\right)\left(J_\nu(k_\rho \rho_<) + \tilde{\mathrm{B}} H_\nu^{(2)}(k_\rho \rho_<)\right) H_\nu^{(2)}(k_\rho \rho_>). \tag{A-26}$$

Note that, $\rho_< = \rho'$ and $\rho_> = \rho$ if $\rho' < \rho$. Other case $\rho_< = \rho$ and $\rho_> = \rho'$ if $\rho' > \rho$.

APPENDIX B

The Steepest Descent Path (SDP) Method

The steepest decent path (SDP or saddle-point method) method is generally employed to evaluate the integral in the scattering problem. the details are described in [47]. The integral of the form

$$I(k_0) = \int_C F(\alpha) e^{k_0 f(\alpha)} d\alpha \tag{B-1}$$

can be written as

$$I(k_0) = \int_C F(\alpha) e^{k_0 f(\alpha)} d\alpha = I_{SI} + I_{SDP}. \tag{B-2}$$

Let's consider only the main contribution from the I_{SDP}, then

$$I(k_0) = \int_{SDP} F(\alpha) e^{k_0 f(\alpha)} d\alpha \tag{B-3}$$

where $f(\alpha)$ is an analytic function. The SDP is the integration path in the complex α plane. Let's consider $k_0 = jk$, and k is positive real value. We skip some derivation details that presented in [47]. The integral in Equation (B-1) can then be simplified as

$$I(k_0) \simeq \frac{e^{k_0 f(\alpha_s)}}{\sqrt{-k_0 f''(\alpha_s)}} 2F(\alpha_s) \int_0^\infty e^{-\xi^2/2} d\xi = \frac{e^{k_0 f(\alpha_s)}}{\sqrt{-k_0 f''(\alpha_s)}} 2F(\alpha_s) \sqrt{\frac{\pi}{2}}, \tag{B-4}$$

$$I(k_0) \simeq \sqrt{\frac{-2\pi}{k_0 f''(\alpha_s)}} F(\alpha_s) e^{k_0 f(\alpha_s)} \tag{B-5}$$

with conditions of

$$f'(\alpha_s) = 0 \tag{B-6}$$

and

$$f''(\alpha_s) \neq 0 \tag{B-7}$$

APPENDIX C

The Computational Scheme for the Fock-Type Integrals Functions

The integral in Equation (C-1) cannot be evaluated analytically. Also, equation (C-1) is singular if argument $X = 0$. Therefore, one can separate the integral into 2 paths ($-\infty$ to 0 and 0 to ∞). This method was presented in [36].

$$\hat{P}_{s,h}(\xi^{L,d}, q_{s,h}) = \frac{e^{-j(\pi/4)}}{\sqrt{\pi}} \int_{-\infty}^{\infty} \frac{V'(\tau) - q_{s,h} V(\tau)}{w_2'(\tau) - q_{s,h} w_2'(\tau)} e^{-j\xi^{L,d}\tau} d\tau \tag{C-1}$$

where $V(\tau)$, $V'(\tau)$, $w_2(\tau)$ and $w_2'(\tau)$ denote the Fock-type Airy functions and their derivative. After some manipulations, the $\hat{P}_{s,h}(\xi^{L,d}, q_{s,h})$ can be finally written as

$$P_{s,h}(X, q_{s,h}) = \frac{e^{-j(\pi/4)}}{\sqrt{\pi}} \left\{ -\frac{1}{2X} + G_1(X,t) + G_2(X,t) \right\} \tag{C-2}$$

$$G_1(X, q_{s,h}) = \frac{e^{-j(\pi/6)}}{2} \cdot \int_0^{\infty} \frac{\left[e^{-j(\pi/6)} Ai'(t) + q_{s,h} e^{j(\pi/6)} Ai(t) \right] e^{-jXrt}}{e^{j(\pi/6)} Ai'(te^{j(2\pi/3)}) + q_{s,h} e^{-j(\pi/6)} Ai(te^{j(2\pi/3)})} dt \tag{C-3}$$

$$G_2(X, q_{s,h}) = -\frac{1}{2} \cdot \int_0^{\infty} \frac{\left[Ai'(t) - q_{s,h} Ai(t) \right] e^{-jXt}}{e^{j(\pi/6)} Ai'(te^{-j(2\pi/3)}) + q_{s,h} e^{-j(\pi/6)} Ai(te^{-j(2\pi/3)})} dt \tag{C-4}$$

The integration scheme employed in the literature [36] is based on the Fourier Quadrature method. In this dissertation, an alternative numerical integration method based on the recursive adaptive Simpson Quadrature is employed to compute this Pekeris

or Fock-Type integration function. The present method is very efficient and requires less computational time. The comparison results of the Fock-type integrals function between a computation scheme presented in [36] and Numerical integration of function $P_{s,h}(X, q_{s,h})$ without the singular factor ($-1/2X$ suppressed) are shown in Fig. C.1. Note that, for the new 3-D impedance Fock-type integral functions presented in Chapter 3, this procedure can be applied.

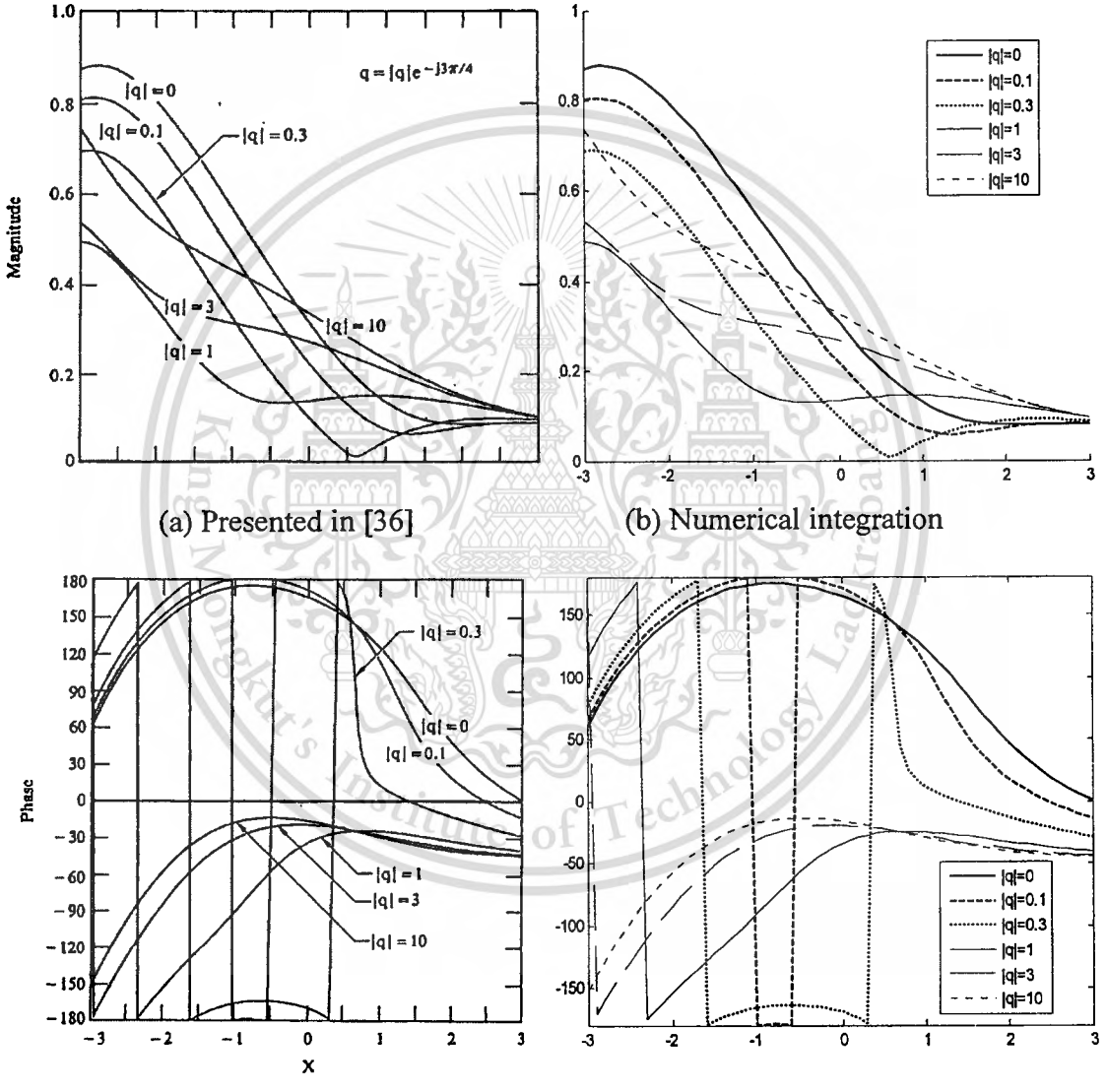

Figure C.1 Comparison results between [36] and Numerical integration based on the recursive adaptive Simpson quadrature

APPENDIX D

Ray Coordinate System and Transformation

The 3-D impedance cylinder problem is shown in Fig. D.1. The cylindrical coordinate $(\hat{\rho},\hat{\phi},\hat{z})$ can be converted into the ray coordinate $(\hat{s},\hat{n},\hat{b})$ by using the ray transformation [30] as shown in Fig. D.2. The formulas used to convert between the cylindrical and the ray coordinate systems are as follows:

$$\begin{aligned}\hat{n}_2 &= \hat{\rho}\sin(\xi)-\hat{\phi}\cos(\xi)\\ &= \hat{\rho}\cos(\beta)-\hat{\phi}\sin(\beta)\end{aligned}, \tag{D-1}$$

and

$$\hat{s}_{xy} = \hat{\rho}\sin(\beta)+\hat{\phi}\cos(\beta). \tag{D-2}$$

The unit vector of the propagation direction can be written as

$$\hat{s}_d = \hat{s}_{xy}\sin(\theta^i)+\hat{z}\cos(\theta^i). \tag{D-3}$$

$$\hat{s}_d = \hat{\rho}\sin(\beta)\sin(\theta^i)+\hat{\phi}\cos(\beta)\sin(\theta^i)+\hat{z}\cos(\theta^i). \tag{D-4}$$

Using $\hat{s}_d = \hat{b}_2\times\hat{n}_2$ or $\hat{b}_2 = \hat{n}_2\times\hat{s}_d$, the unit vector of $\hat{b}_2$ can be written as

$$\hat{b}_2 = \hat{z}\sin(\theta^i)-\hat{\phi}\cos(\beta)\cos(\theta^i)+\hat{\rho}\sin(\beta)\cos(\theta^i). \tag{D-5}$$

Generally, the diffracted field can be written as

$$\vec{E}^d = \hat{\rho}E^d_\rho+\hat{\phi}E^d_\phi+\hat{z}E^d_z = \hat{n}_2E^d_n+\hat{b}_2E^d_b \tag{D-6}$$

where

$$E^d_n = -\sin(\beta)E^d_\phi+\cos(\beta)E^d_\rho \tag{D-7}$$

and

$$E^d_b = \sin(\theta_i)E^d_z-\cos(\beta)\cos(\theta_i)E^d_\phi-\sin(\beta)\cos(\theta_i)E^d_\rho \tag{D-8}$$

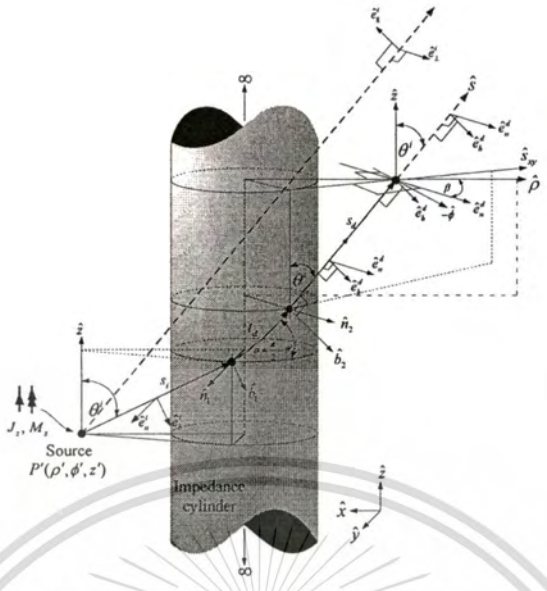

Figure D.1 Impedance cylinder problem

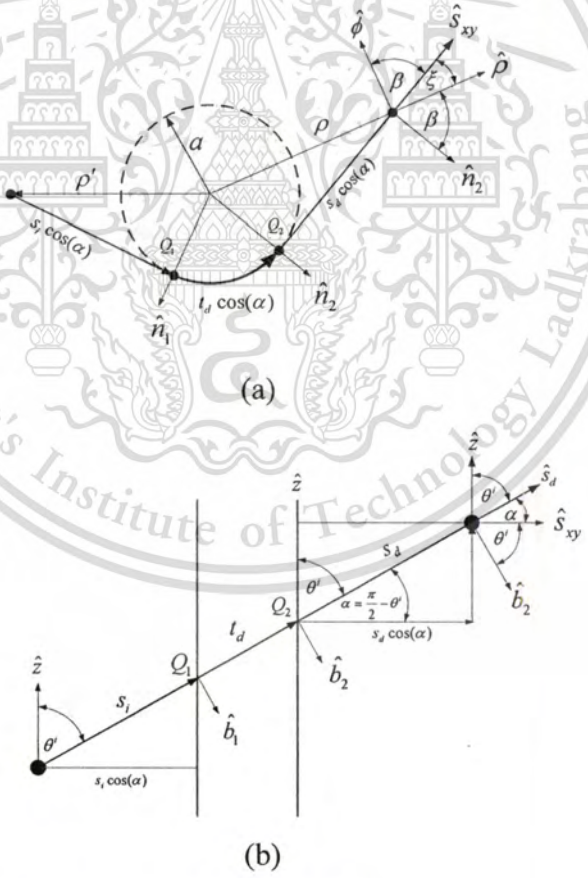

Figure D.2 (a) Top view and (b) Unwrapped ray path.

APPENDIX E

The Surface Impedance (Z_s) of a Material Coated PEC Cylinder and Other

The proposed 3-D UTD solution for EM wave scattering by impedance cylinder requires the approximate surface impedance value Z_s. The examples of the closed-form solutions of the material coated cylinder problems are summarized.

E.1 Single layer material coated PEC cylinder

The single layer material coated PEC cylinder problem is shown in Fig. E.1 where a radius of the PEC cylinder and coated thickness are defined as a and t, respectively. The $a_{equvl.}$ denotes the equivalent radius of the impedance cylinder. The coated material parameters consist of the relative permittivity ε_r and permittivity μ_r.

Figure E.1 Single layer material coated cylinder and its equivalent problem.

The surface impedance of the single layer material coated cylinder which comes from the approximation of the thin coating $(t << a)$. The closed-form solution is constructed by enforcing the tangential electric field continuous at the boundary of $\rho = a + t$ and tangential electric field equal to zero at the PEC surface of $\rho = a$. The closed-form solution is valid only a thin coating [41]. The closed-form solution can be written as

$$\begin{bmatrix} E_z \\ H_z \end{bmatrix}_{\rho=a_{equvl.}} = \begin{bmatrix} Z_s & 0 \\ 0 & -Z_s^{-1} \end{bmatrix} \begin{bmatrix} H_\phi \\ E_\phi \end{bmatrix}_{\rho=a_{equvl.}} \tag{E-1}$$

thus

$$Z_s \approx -\frac{jZ_0 kt}{\varepsilon_r}\left(1-\varepsilon_r\mu_r\right)\left[1+\frac{(kt)^2}{2}\left(1-\varepsilon_r\mu_r\right)\right]^{-1}. \tag{E-2}$$

E.2 Multi layers material coated PEC cylinder

The multi layers material coated PEC cylinder problem is shown in Fig. E.2 where a radius of the PEC cylinder and n coated thicknesses are defined as a and t_n, respectively. $a_{equvl.}$ denotes the equivalent radius of the impedance cylinder. The material layers consists of the relative permittivity ε_r^n and permittivity μ_r^n.

Figure E.2 Multilayers material coated cylinder and its equivalent problem

The surface impedance is obtained by using the approximated closed-form solution of the multilayers flat surface [46] as shown in Fig. E.3.

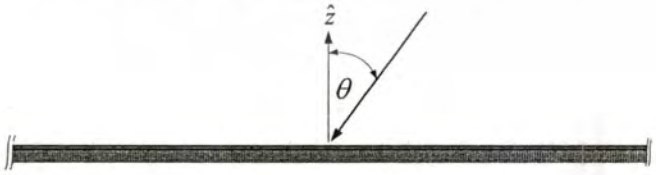

Figure E.3 Multi layers material coated flat surface

For example, the PEC flat surface coated with three material layers is shown in Fig. E.3. The solutions of wave equation of each layers are defined as

$$E_y = \begin{cases} E_{i0}e^{-jk_0 z} + E_{r0}e^{jk_0 z}, & z < 0 \\ E_1^+ e^{-jk_1 z} + E_1^- e^{jk_1 z}, & 0 \le z \le l_1 \\ E_2^+ e^{-jk_2 z} + E_2^- e^{jk_2 z}, & l_1 \le z \le l_2 \\ E_3^+ e^{-jk_3 z} + E_3^+ e^{jk_3 z}, & l_2 \le z \le l_3 \end{cases}, \tag{E-3}$$

$$H_y = \begin{cases} \left(E_{i0}e^{-jk_0 z} + E_{r0}e^{jk_0 z}\right)/Z_0, & z < 0 \\ \left(E_1^+ e^{-jk_1 z} + E_1^- e^{jk_1 z}\right)/Z_1, & 0 \le z \le l_1 \\ \left(E_2^+ e^{-jk_2 z} + E_2^- e^{jk_2 z}\right)/Z_2, & l_1 \le z \le l_2 \\ \left(E_3^+ e^{-jk_3 z} + E_3^+ e^{jk_3 z}\right)/Z_3, & l_2 \le z \le l_3 \end{cases} \tag{E-4}$$

where $Z_i = Z_0\sqrt{\mu_r^i \varepsilon_r^i}$, $k_i = 2\pi f\sqrt{\mu_r^i \varepsilon_r^i}/c$, $l_1 = t_1$, $l_2 = t_1 + t_2$ and $l_3 = t_1 + t_2 + t_3$.

The boundary conditions of all boundaries are defined as

$$E_0(0) = E_1(0), \quad H_0(0) = H_1(0), \tag{E-5a}$$

$$E_1(l_1) = E_2(l_1), \quad H_1(l_1) = H_2(l_1), \tag{E-5b}$$

$$E_2(l_2) = E_3(l_2), \quad H_2(l_3) = H_2(l_2). \tag{E-5c}$$

The reflection coefficient (R) can be written as

$$R = \frac{E_{r0}}{E_{r0}} = \frac{Z_s - Z_0}{Z_s + Z_0}, \tag{E-6}$$

where

$$Z_s = \frac{Z_1 Z_3^2 \delta_1\delta_2\delta_3 - Z_2 Z_3^2 \delta_3 - Z_2^2 Z_3 \delta_2 - Z_1 Z_2 Z_3 \delta_1}{Z_1 Z_2 Z_3 - Z_1 Z_3^2 \delta_2\delta_3 - Z_2 Z_3^2 \delta_1\delta_3 - Z_2^2 Z_3 \delta_1\delta_2} Z_1, \tag{E-7}$$

and $\delta_i = \tanh(jk_i t_i)$. t_i denotes the coated thickness of each layer.

REFERENCES

[1] W. Dargie and C. Poellabauer, *Fundamentals of Wireless Sensor Networks: Theory and Practice*, John Wiley and Sons, 2010.

[2] L. Yu, N. Wang and X. Meng, "Real-time forest fire detection with wireless sensor networks," *Proceedings of the 2005 International Conference on Wireless Communications, Networking and Mobile Computing*, vol.2, no., pp. 1214- 1217, 23-26 Sept. 2005

[3] Z. W. Sim, R. Shuttleworth, M. J. Alexander, and B. D. Grieve, "Compact patch antenna design for outdoor RF energy harvesting in wireless sensor networks," *Progress In Electromagnetics Research,* Vol. 105, 273-294, 2010.

[4] M. Krairiksh, J. Varith and A. Kanjanavapastit, "Wireless sensor network for monitoring maturity stage of fruit," *Wireless Sensor Network*, Vol. 3 No. 9, 2011, pp. 318-321.

[5] J. Ju, I. Park, Y. Lee, J. Cho, H. Cho, H. Yoe and C. Shin, "An implementation of the salt-farm monitoring system using wireless sensor network," *Communications in Computer and Information Science, 1,* Volume 78, Security-Enriched Urban Computing and Smart Grid, Pages 647-655

[6] H. L. Bertoni, *Radio Propagation for Modern Wireless Systems.* Prentice-Hall, New Jersey, 2000.

[7] J. S. Seybold, *Introduction to RF Propagation,* John Wiley and Sons, 2005.

[8] J. A. R. Azevedo and F. E. S. Santos, "An empirical propagation model for forest environments at tree trunk level," *IEEE Trans. Antennas Propagat.*, Vol. 59, 2357-2367, 2011.

[9] Y. S. Meng, Y. H. Lee and B. C. Ng, "Study of propagation loss prediction in forest environment," *Progress In Electromagnetics Research B, PIER B*, Vol. 17, 117-133, 2009.

[10] J. A. Gay-Fernandez, M. Garcia Sánchez, I. Cuinas, A. V. Alejos, J. G. Sanchez, and J. L. Miranda-Sierra, "Propagation analysis and deployment of a wireless sensor network in a forest," *Progress In Electromagnetics Research*, Vol. 106, 121-145, 2010.

[11] Y. Li and H. Ling, "Investigation of wave propagation in a dielectric rod array: toward the understanding of HF/VHF propagation in a forest," *IEEE Trans. Antennas Propagat.*, Vol. 58, 4025-4032, 2010.

[12] D. N. Schettino, F. J. S. Moreira and C. G. Rego, "Efficient ray tracing for radio channel characterization of urban scenarios," *IEEE Trans. Magn.*, Vol. 43, 1305-1308, 2007.

[13] H. M. El-Sallabi and P. Vainikainen, "Radio wave propagation in perpendicular streets of urban street grid for microcellular communications. Part I: channel modeling," *Progress In Electromagnetics Research, PIER* 40, 229–254, 2003.

[14] G. Koutitas and C. Tzaras, "A UTD solution for multiple rounded surfaces," *IEEE Trans. Antennas Propagat.*, Vol. 54, 1277-1283, 2006.

[15] M. Ghaddar, L. Talbi, T. A. Denidni and A. Sebak, "A conducting cylinder for modeling human body presence in indoor propagation channel," *IEEE Trans. Antennas Propagat.*, Vol. 55, 3099 - 3103, 2007.

[16] K. Phaebua, T. Lertwiriyaprapa, C. Phongcharoenpanich and M. Krairiksh, "Path loss prediction in durian orchard using uniform geometrical theory of diffraction," *Proceedings of 2009 IEEE AP-S Int. Symp.*, 4 pages, 2009.

[17] P. H. Pathak, "An asymptotic analysis of the scattering of plane waves by a smooth convex cylinder," *Radio Sci.*, Vol. 14, 419-435, 1979.

[18] P. H. Pathak, W. D. Burnside and R. J. Marhefka, "A uniform UTD analysis of the diffraction of electromagnetic waves by a smooth convex surface," *IEEE Trans. Antennas Propagat.*, Vol. 28, 609-622, 1980.

[19] P. H. Pathak, "High-frequency techniques for antenna analysis," *Proc. IEEE*, Vol. 80, 44-65, 1992.

[20] D. A. McNamara, C. W. I. Pistorius, and J. A. G. Malherbe, *Introduction to the Uniform Geometrical Theory of Diffraction.* Artech House, New York, 1990.

[21] L. B. Felsen, and N. Macuvitz, *Radiation and Scattering of Waves.* Prentice-Hall, New Jersey, 1973.

[22] P. H. Pathak, Source-excited Boundary Value Problem. The Ohio State University, OH: Unpublished Class Notes ECE811.

[23] T. Lertwiriyaprapa, P. H. Pathak, and J. L. Volakis, "A UTD for predicting fields of sources near or on thin planar positive/negative material discontinuities," *Radio Sci.*, Vol. 42, RS6S18, 14 pages, 2007.

[24] T. Lertwiriyaprapa, P. H. Pathak, and J. L. Volakis, "An approximate UTD ray solution for the radiation and scattering by antennas near a junction between two different thin planar material slab on ground plane," *Progress In Electromagnetics Research, PIER*, Vol. 102, 227-248, 2010.

[25] H. H. Syed, and J. L. Volakis, "An asymptotic analysis of the plane wave scattering by a smooth convex impedance cylinder," Report, Radiation Laboratory Department of Electrical Engineering and Computer Science, The University of Michigan Ann Arbor, 1990.

[26] H. H. Syed, and J. L. Volakis, " High-frequency scattering by a smooth coated cylinder simulated with generalized impedance boundary conditions," *Radio Sci.*, Vol. 26, 1305-1314, 1991.

[27] H. Kim and N. Wang, " UTD solution for electromagnetic scattering by a circular cylinder with thin lossy coatings, " *IEEE Trans. Antenna & Propagat.*, Vol. AP-37, pp. 1463-1472, Nov. 1989.

[28] K. Phaebua, T. Lertwiriyaprapa, C. Phongcharoenpanich and P. H. Pathak, "A Modified UTD Solution for an Impedance Cylinder Surface," *Proceedings of the 2011 Electrical Engineering/Electronics, Computer, Telecommunications, and Information Technology International Conference (ECTI-CON2011)*, 208-211, 2011.

[29] T. Lertwiriyaprapa, K. Phaebua, C. Phongcharoenpanich and M. Krairiksh, "Application of UTD ray solution for characterization of propagation in Thai commercial orchard," *Proceedings of Int. Conf. on Electromagn. in Adv. Appl.*, 176 - 179, 2010.

[30] S. Kato and N. Wang, Ray Optic Formulation for the Scattering of an Obliquely Incident Plane wave from an Infinitely Long Dielectric Coated Circular Cylinder, ElectroSci. Lab., Dept. Elect. Eng., Columbus, Ohio State Univ., Final Rep. 717675-5, June 1990.

[31] Y. Li and H. Ling, "Numerical modeling and mechanism analysis of VHF wave propagation in forested environments using the equivalent slab model," *Progress In Electromagnetics Research, PIER* 91, 17-34, 2009.

[32] G. Tyrus, *Radiation and Propagation of Electromagnetic Waves*, Academic, London, 1969.

[33] J. R. Wait, *Electromagnetic Radiation from Cylindrical Structures*, Pergamon Press, Inc., New York, 1959.

[34] R. F. Harrington, *Time–harmonic electromagnetic fields*, John Wiley & Sons, New York, 2001

[35] J. R. Wait, *Electromagnetic radiation from cylindrical structures*, Peter Peregrinus, London, 1988.

[36] L. W. Pearson, "A scheme for automatic computation of fock-type integrals," *IEEE Trans. Antennas Propagat.*, Vol. 35, 1111-1118, 1987.

[37] J. C. Rautio, "Reflection coefficient analysis of the effect of ground on antenna patterns," *IEEE Trans. Antennas Propagat.*, Vol. 29, 5-11, 1980.

[38] T. Lertwiriyaprapa, P. H. Pathak, K. Tap, and R. J. Burkholder, "Application of the complex source point method for analyzing the diffraction of an electromagnetic Gaussian beam by a curved wedge using UTD concepts," *Proceedings of 2004 IEEE AP-S Int. Symp.,* 4 pages, 2004.

[39] L. B. Felsen, "Complex source point solution of the field equations and their relation to the propagation and scattering of Gaussian beams," *Symposia Mathematica*, Vol. 18, 39-56, 1975.

[40] K. Tap, "Complex source point beam expansions for some electromagnetic radiation and scattering problems," Ph.D. dissertation, The Ohio State Univ., Columbus, OH, 2007.

[41] C. Tokgoz "Asymptotic high frequency analysis of the surface fields of a source excited circular cylinder with an impedance boundary condition," Ph.D. dissertation, The Ohio State Univ., Columbus, OH, 2002.

[42] H. Sahin and N. Ay, "Dielectric properties of hardwood species at microwave frequencies," *Journal of Wood Sci.*, Vol. 50, 375-380, 2004.

[43] E. Peyskens, M. de Pourcq, M. Stevens, and J. Schalck, "Dielectric properties of softwood species at microwave frequencies," *Wood Sci. and Tech.*, Vol. 18, 267-280, 1984.

[44] L. H. Ford and R. Oliver, "An experimental investigation of the reflection and absorption of radiation of 9-cm. wavelength," *Proc. Phys. Soc.* Vol. 58, 256-280, 1945.

[45] H. S. Kim and R. M. Narayanan, "A new measurement technique for obtaining the complex relative permittivity of terrain surfaces," *IEEE Trans. Geosci. Remote Sensing*, Vol. 40, 1190-1194, 2002.

[46] C. X. Yuan, Z. X. Zhou, J.W. Zhang, X. L. Xiang, Y. Feng, H. G. Sun, "Properties of propagation of electromagnetic wave in a multilayer radar-absorbing structure with plasma and radar-absorbing material," *IEEE Transactions on Plasma Science,* vol.39, no.9, pp.1768-1775, Sept. 2011.

[47] C. Balanis, *Advanced Engineering Electromagnetics*, John Wiley & Sons, 1989.